



HAL
open science

The origin of peculiar magnetic response of thin Co films intercalated between Graphene and Ir(111)

Ilaria Carlomagno

► **To cite this version:**

Ilaria Carlomagno. The origin of peculiar magnetic response of thin Co films intercalated between Graphene and Ir(111). Materials Science [cond-mat.mtrl-sci]. Université Grenoble Alpes; Università degli studi Roma Tre, 2017. English. NNT: 2017GREAY025 . tel-01688833

HAL Id: tel-01688833

<https://theses.hal.science/tel-01688833>

Submitted on 19 Jan 2018

HAL is a multi-disciplinary open access archive for the deposit and dissemination of scientific research documents, whether they are published or not. The documents may come from teaching and research institutions in France or abroad, or from public or private research centers.

L'archive ouverte pluridisciplinaire **HAL**, est destinée au dépôt et à la diffusion de documents scientifiques de niveau recherche, publiés ou non, émanant des établissements d'enseignement et de recherche français ou étrangers, des laboratoires publics ou privés.

THÈSE

Pour obtenir le grade de

**DOCTEUR DE LA COMMUNAUTE UNIVERSITE
GRENOBLE ALPES**

**préparée dans le cadre d'une cotutelle *entre la
Communauté Université Grenoble Alpes et
l'Università degli studi Roma Tre***

Spécialité: **Physique de la Matière Condensée et du Rayonnement**

Arrêté ministériel: le 6 janvier 2005 - 7 août 2006

Présentée par

Ilaria CARLOMAGNO

dirigée par **Carlo MENEGHINI** et codirigée par **Roberto FELICI**

préparée au sein de l'ESRF, European Synchrotron Radiation Facility

dans **les Écoles Doctorales de Physique** et de **Scienze della materia,
nanotecnologie e sistemi complessi**

L'origine de la réponse magnétique particulière des films minces de Co intercalés entre Graphene et Ir(111)

Thèse soutenue publiquement le **12/04/2017**

devant le jury composé de:

Mme Giuliana AQUILANTI

Elettra-Sincrotrone Trieste, Rapporteur

Mme Luisa FERNANDEZ-GUBIEDA

Professeur, Universidad del País Vasco, Rapporteur

Mme Antonella IADECOLA

Ingénieur de recherche, Synchrotron SOLEIL, examinateur

M Carlo MARIANI

Professeur, Università La Sapienza, président du jury

M Settimio MOBILIO

Professeur, Università Roma Tre, examinateur

M Gilles RENAUD

Ingénieur de recherche, CEA-Grenoble, examinateur



The origin of the peculiar magnetic response of Co thin films intercalated between Graphene and Ir(111)

by

Ilaria Carlomagno

Dissertation presented in partial fulfillment of the requirements for the degree of Doctor of Philosophy

in

“Scienze della materia, nanotecnologie e sistemi complessi”

and

“Physique de la Matière Condensée et du Rayonnement”



Supported by the ESRF

Supervisors:
Carlo Meneghini
Roberto Felici

Roma, 12th of April 2017

The noblest pleasure is the joy of understanding.
Leonardo da Vinci

Contents

1	Magnetic anisotropy in ferromagnets	9
1.1	Cobalt films	12
2	Interaction between X-rays and matter	17
2.0.1	EXAFS	22
2.0.2	XANES	33
2.1	X-ray Scattering	38
2.1.1	Many particles system	40
2.1.2	Scattering from a small crystal	44
2.1.3	Surface diffraction	49
2.1.4	Electron density representations	58
2.1.5	X-Ray Reflectivity	60
2.1.6	specular reflection from a uniform layer	65
2.2	Visible light and anisotropic effects	69
3	Methodology	73
3.1	Laboratory Techniques	73
3.1.1	Thin films growth	74
3.1.2	Graphene capping layer	75
3.1.3	XPS	77
3.1.4	LEED	82
3.1.5	MOKE	84
3.2	Synchrotron Radiation	85
3.2.1	Beamlines	92
3.2.2	BM23: the XAFS beamline	92
3.2.3	ID03: the surface diffraction beamline	94
4	Experiments and results	101
4.1	The Graphene's effects	101
4.2	Intercalation dynamics	109
4.2.1	The thickness dependence	110
4.2.2	The effects of deposition temperatures	113
4.3	Co/Ir interface evolution upon thermal annealing	116

4.3.1	Magnetic response dependence on the film's integrity . .	116
4.3.2	Co atomic environment	117
4.4	Capping efficiency and origin of the enhanced PMA	126
4.4.1	Oxidation prevention	129
5	Conclusions	141
6	Rèsumè substantiel	145
6.1	Introduction	145
6.2	Réalisation expérimentale	146
	Bibliography	153

Abstract

This thesis focuses on the structural evolution and the peculiar magnetic response of Cobalt films observed upon intercalation between Graphene and Ir(111).

The origin of the exotic magnetic behaviour of such films [1] has not been found yet. In this respect, the final goal of this work is to probe the effects of the structural anisotropy on the magnetic anisotropy.

Several parameters such as: film thickness, annealing times and temperatures, Graphene presence, and Co local environment were taken into account as possible sources of structural anisotropy. A complete analysis was carried out using complementary, state-of-the-art techniques. While laboratory techniques such as X-ray Photoelectron Spectroscopy (XPS) and Magneto-Optic Kerr Effect (MOKE) provided information on the Co distribution along the direction perpendicular to the surface, and on the magnetic response, synchrotron radiation techniques such as X-ray Absorption Spectroscopy (XAS) and Grazing Incidence X-ray Diffraction (GIXD) probed the local structure and the long range order of the films.

The analysis presented in this thesis includes the surface effects at the Co/Ir interface, the local Co environment, the crystalline structure of the film and the system roughness and average disorder. In particular, the evolution of such parameters is presented and discussed together with their effect on the macroscopic magnetic response of the intercalated films.

The results demonstrate that thermal treatments affect Co morphology, roughness, and local coordination. Such effects alter the film structure affecting the overall magnetic anisotropy. This information alone is valuable for applicative purposes. Moreover, the description of the micro-structural modifications provides a deep insight into the physical properties of intercalated Co films.

Resumé

Le sujets de cette thèse sont l'évolution structurale et la réponse magnétique particulière des films de cobalt observés lors de l'intercalation entre graphène et Ir (111).

L'origine du comportement magnétique exotique de ces films n'a pas été trouvée encore. À cet égard, l'objectif final de ce travail est de sonder les effets de l'anisotropie structurale sur l'anisotropie magnétique.

Plusieurs paramètres tels que l'épaisseur du film, les temps et les températures de la procédure du *annealing*, la présence de graphène et l'environnement local de Co ont été pris en compte comme possibles sources d'anisotropie structurale. Une analyse complète a été réalisée en utilisant des techniques complémentaires et avancées. Techniques comme la spectroscopie de photo-électrons de rayons X (XPS) et l'effet Kerr magnéto-optique (MOKE) ont fourni des informations sur la distribution de Co dans la direction perpendiculaire à la surface et sur la réponse magnétique. Cependant, techniques de rayonnement synchrotron comme la spectroscopie d'absorption de rayonnement X (XAS) et la diffraction de rayons X par incidence rasante (GIXD) ont sondé la structure locale et l'ordre à long terme des films.

L'analyse présentée dans cette thèse inclut les effets de surface à l'interface Co/Ir, l'environnement local autour du Co, la structure cristalline du film, la rugosité du système et le désordre moyen. En particulier, l'évolution de ces paramètres est présentée et discutée en même temps que leur effet sur la réponse magnétique macroscopique des films intercalés.

Les résultats démontrent que les traitements thermiques affectent la morphologie du Co, sa rugosité et sa coordination locale. Tels effets altèrent la structure du film affectant l'anisotropie magnétique globale. Cette information est utile à des fins applicatives. De plus, la description des modifications micro-structurales fournit un aperçu approfondi des propriétés physiques des films de Co intercalés.

Introduction

This thesis aims to describe the structural evolution of Cobalt films upon annealing. The goal of this work is to find the relation between the structural, and the magnetic anisotropy of the ferromagnetic films. Particular attention is paid to the surface effects affecting the macroscopic magnetic response of the systems.

In general, ferromagnetic films can be exploited in the most advanced application for magnetism: the technology underlying magnetic storage and memory [2, 3, 4]. In fact, artificially engineered thin film structures have been used since the 1990's [5]. Later on, in the early 2000's, nonvolatile magnetic memories were proposed as magnetic random access memories (MRAM) [6]. In this respect, thin ferromagnetic films possessing perpendicular magnetic anisotropy (PMA) occupy a prominent position due to their potential use in ultra-high-density MRAM [7, 8, 9, 10, 11].

PMA, compared to longitudinal magnetization, allows smaller magnetic bit size while preserving the magnetic state from thermal fluctuations. Since 1978, when the first Co-Cr recording film with PMA was reported [12], a number of systems have been explored. Among these, hcp Co is known to have high intrinsic magnetic anisotropy, and to develop PMA for thickness below a critical value $t_c \simeq 7$ monolayers (ML) [13, 1].

For the easily oxidisable Co films to be suitable for applications, they need to be protected against degradation. This challenge has led to the fabrication of Graphene (Gr) capped Co films characterized by enhanced chemical stability. The *in-situ* Gr growth on thin Co film can be achieved by chemical vapour deposition (CVD). However, this procedure requires high temperatures ($T \simeq 1000$ °C) representing an issue for the structural integrity of the Co layer. On the other hand, the use of intercalation procedures requires much lower temperatures ($T \simeq 300$ °C) avoiding the integrity problems during the production of Gr/Co/Ir(111) heterostructures [14].

Gr capping has been proven to affect the magnetic properties of thin Co films: intercalated Gr/Co/Ir systems present smaller magnetic domains while PMA is retained even by Co film exceeding t_c [1]. These findings spurred renewed interest in applications of such heterostructures and stimulated the fundamental research about the role of Gr in the magnetic properties of intercalated Co layers. Recent work provides different explanations for the observed

behavior invoking the intercalation topology [15], the hybridization of Gr and Co electron orbitals [16, 1], the magnetic ordering of Co upon intercalation [17] and the induced magnetic moment on Gr [18]. Although large attention has been paid to the Co-Gr interaction, less has been reported to disentangle the contribution of Gr-Co interaction from that of the Co-Ir interface during the preparation of the Gr/Co/Ir(111) heterostructures.

This work focuses on the surface effects involving the Co-Ir interface and aims to provide a fine characterization of this region combining several *in-situ* techniques. The complementary information achieved with each technique resulted into a detailed description of the structural evolution of Co thin films upon intercalation. In particular, laboratory techniques such as X-ray Photoelectron Spectroscopy (XPS) and Magneto-Optic Kerr Effect (MOKE) were employed to gain information on the Co distribution along the direction perpendicular to the surface and on the magnetic response, respectively. Moreover, synchrotron radiation techniques such as X-ray Absorption Spectroscopy (XAS) and Grazing Incidence X-ray Diffraction (GIXD) were used to assess the local structure and the long range order of the films.

The thesis is organized as follows:

Chapter 1: Introduction to the concept of magnetic anisotropy with a few details concerning the particular case of Co films.

Chapter 2: Phenomena driving the interaction between light and matter.

Chapter 3: Laboratory techniques.

Chapter 4: Synchrotron radiation techniques.

Chapter 5: Experimental measurements divided in four sections: each one dealing with a different experimental run involving several characterization techniques.

Chapter 6: Conclusions.

Magnetic anisotropy in ferromagnets

Nowadays we face a plethora of different magnetic behaviours depending on the sample nature, composition, morphology, nanostructure, providing a stimulating research field and an abundance of innovative materials together with ideas about novel applications. The present work aims to pay particular attention on the magnetic anisotropy of nanostructured, ferromagnetic films.

The first approach to the understanding of ferromagnetism can be dated back to the early 1950's, that is when Néel research was published [19]. Néel work represented a major breakthrough in the comprehension of ferromagnetic phenomena. Ferromagnets give rise to an hysteretic behaviour which can be graphically represented in the plane M/H , as shown in Fig.1.1. The curve, known as *hysteresis curve*, represents the behaviour of a ferromagnet placed into a varying magnetic field \mathbf{H} : the material, initially unmagnetized ($M = 0$) gradually aligns its magnetic moments with \mathbf{H} so that a net magnetization \mathbf{M} is found. \mathbf{M} 's intensity increases with the external field until a saturation value M_s and usually decreases to the remanent magnetization M_r value after the magnetizing field has been removed. To bring the material back to the unmagnetized state, one has to apply a coercive field \mathbf{H}_c antiparallel to that of M_s .

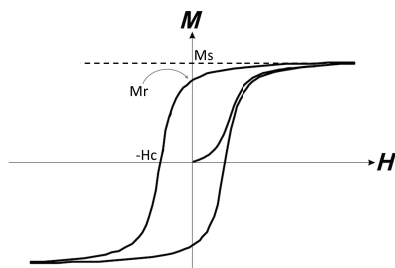


Figure 1.1: The cycle of magnetization of a ferromagnet is represented on the M/H plane. Starting from the unmagnetized state (the origin of the axes), an increasing magnetic field \mathbf{H} is applied. This causes the magnetic moments to progressively align with the field's direction until the saturation M_s is reached. Reducing the field, the magnetization slowly decreases until a remanent value M_r which remains for $H = 0$. To set \mathbf{M} back to 0, an opposite coercive field H_c has to be applied. For more intense negative field, the negative saturation is reached closing the cycle.

The hysteretic response can be found only until the temperature remains

below the Curie's temperature T_c . Above T_c , the thermal fluctuations of the magnetic moments are too strong for the material to present a net magnetization. In other words, above T_c ferromagnets behave paramagnetically. The value of T_c is determined by the sample properties, such as atomic species and structure. In facts, these features affect the electric fields or mechanical strain or stress present in the material. These effects result into a symmetry breaking defining preferential orientations for the axial vector \mathbf{M} . Since the source of anisotropy can be identified with polar vectors, the preferential orientations can only be represented by unique axes: the "easy axes" [2].

In thin ferromagnetic films, one usually deals with an *uniaxial* anisotropy, meaning that only one easy axis is found. The energy needed to rotate \mathbf{M} from the easy axis to a hard axis is called "magneto-crystalline anisotropy energy". The energy density associated with this rotation E_{mc} , depends on the angle θ enclosed by \mathbf{M} and the easy axis, and on the anisotropy constant K_{mc} through the relation $E_{mc} = -K_{mc} \sin^2 \theta$. K_{mc} is the anisotropy constant with dimensions [energy/volume]. K_{mc} is the sum of the contributions from interface atoms and inner atoms of a magnetic layer of thickness t . This can be expressed through a volume anisotropy constant K_v , and an interface one. Since the latter becomes significant only in the thin film regime, it is usually expressed as a ratio of the constant K_i over the thickness t . The magnetocrystalline constant then becomes:

$$K_{mc} = K_v + 2\frac{K_s}{t} \quad (1.1)$$

where $K_v < 0$ and $K_s > 0$. The relation 1.1 is presented under the convention that K_s/d (with d the thickness of 1 ML) represents the difference between the anisotropy of the interface atoms with respect to the inner or bulk atoms. Also the layer is assumed to be bounded by two identical interfaces accounting for the prefactor 2.

When K_v dominates, $K_{mc} < 0$ and the preferred direction of the magnetization lies in the film plane. On the contrary, for low thickness, $K_{mc} > 0$ and PMA is found [20]. A typical parameter defining the magnetic properties of the film is the critical thickness at which the interface contribution equal the volume one:

$$t_c = -2\frac{K_s}{K_v}. \quad (1.2)$$

For thickness below t_c , the interface anisotropy outweighs the volume contribution and the easy axis rotates out of the film plane. t_c marks the higher limit for the perpendicular magnetic anisotropy (PMA).

The main sources of the magnetic anisotropy in thin films are dipolar interaction, the spin-orbit interaction and the film compression or strain due

to a lattice mismatch with the substrate or the overlayer¹.

Dipolar Interaction

The long-range dipolar interaction is sensitive to the macroscopic shape of the sample. For this reason, the anisotropy arising from this interaction is usually referred to as the *shape* anisotropy. Its effect on the magnetic response can be described as the action of a demagnetizing field $\mathbf{H}_d = -N\mathbf{M}$ where \mathbf{M} is the magnetization vector and N is the shape-dependent demagnetizing tensor. For thin films, N has one only term which is different from zero: N_\perp . Therefore, using \mathbf{H}_d in the expression for the magnetostatic energy one gets:

$$E = -\frac{\mu_0}{2V} \int M \cdot \mathbf{H}_d dv. \quad (1.3)$$

Then, the constant for the shape anisotropy results to be:

$$K_{shape} = -\frac{\mu_0}{2} M_s^2 \cos^2 \vartheta. \quad (1.4)$$

with ϑ being the angle between M and the film's normal. This result is valid within the limit of magnetization continuity: in facts, it holds whenever M can be assumed to be uniform with intensity equal to the saturation magnetization M_s . The minimum for E_{shape} is reached for $\vartheta = 0$, *i.e.* when M lies in the plane of the film. Moreover, since E_{shape} does not depend on the film's thickness, it contributes only to K_v in Eq.1.1.

Below a certain thickness, one cannot neglect the discrete nature of the system. In this limit, the outer layers experience a demagnetizing field being way weaker than the inner layers. As a consequence, one should consider two different dipolar interactions for inner and outer atoms and Eq.1.4 is not valid anymore. In particular, for outer atoms other sources of interface anisotropy, such as spin-orbit coupling, becomes dominant.

Spin-orbit interaction

For itinerant materials the spin-orbit interaction induces a small orbital momentum, which then couples the total (spin plus orbital) magnetic moment to the crystal axes² [20]. This results in a total energy which depends on the orientation of the magnetization relative to the crystalline axes. Since it reflects the symmetry of the crystal, this anisotropy was named *magneto-crystalline*.

In addition to the crystal lattice anisotropy, another contribution may arise from the film's tension or compression induced by a lattice mismatch with the substrate or the overlayer. This contribution is commonly referred

¹Here, effects due to antiferromagnetic coupling have been neglected.

²In principle, also dipolar and exchange interaction contributes to the magnetocrystalline anisotropy. However, in cubic crystals, these contributions cancels out.

to as *magnetoelastic anisotropy* and was historically distinguished from the magneto-crystalline anisotropy. On a microscopic level, however, they both arise from the same mechanism, the anisotropy of the atomic structure and the bonding in conjunction with the spin-orbit interaction. For this reason, we will discuss both of them under the general name of magneto-crystalline anisotropy.

In the case of uniaxial anisotropy, the anisotropy energy can be written as a function of θ , the angle between \mathbf{M} and the direction of the easy axis:

$$K_{mc} = K_0^{mc} + K_1^{mc} \sin^2 \theta + K_2^{mc} \sin^4 \theta + \dots \quad (1.5)$$

where $K_0^{mc}, K_1^{mc}, K_2^{mc}$ are empirical parameters of the medium varying with the temperature. In the case of hexagonal close-packed (hcp) crystals, the easy axis lies along the c -plane, represented in Fig.1.2. From Eq.1.5, one can see that when \mathbf{M} is parallel to this direction, K_{mc} has a minimum. This contribution is responsible for the easy axis rotation outside of the film plane.

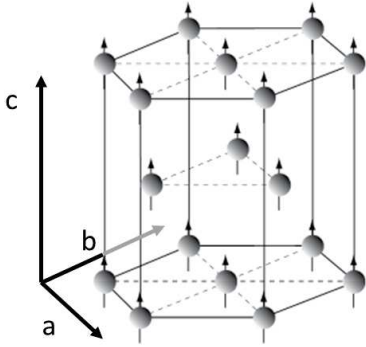


Figure 1.2: Representation of an hcp crystalline arrangement. Circles represent atoms while arrows indicate the direction of the atomic magnetic moments. Hcp crystals can be represented using two base vectors, \mathbf{a} and \mathbf{b} , having the same length and a third vector, \mathbf{c} being perpendicular to the \mathbf{ab} plane whose length $|\mathbf{c}| \neq |\mathbf{a}| = |\mathbf{b}|$. For hcp Co, the easy axis lies along the c direction and $|\mathbf{c}| = 4.07\text{\AA} > |\mathbf{a}| = |\mathbf{b}| = 2.507\text{\AA}$.

Typically, $K_{shape} > K_1^{MC}$ and the shape anisotropy dominates over the magneto-crystalline contribution. When this happens, the easy axis lies parallel to the film plane. However, in extremely thin films, the discrete nature of magnetic moments plays a key role and the surface and interface contributions dominate. This can result in an out-of-plane easy axis.

1.1 Cobalt films

Cobalt is the 27th element in the periodic table, its symbol is “Co” and, at room temperature it is a solid crystal with either fcc or hcp structure. The length of the basis vectors for fcc Co is $a = b = c = 3.54 \text{\AA}$, whereas $a = b = 2.507 \text{\AA}$ and $c = 4.07 \text{\AA}$ for the hcp. The hcp structure can also be seen as a compression of the fcc crystal along the $[111]$ direction.

Among the ferromagnetic materials, Co has an intense magnetization and the highest Curie’s temperature (1121 °C). Its electronic configuration is represented in Fig.1.3.

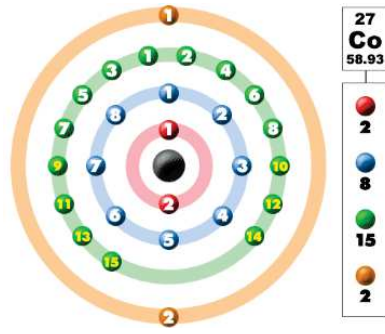


Figure 1.3: Cobalt electronic configuration. All the electronic shells are complete except the $3d$ from which the magnetic properties arise.

The incomplete d shell is the origin of the two most important properties of the Co: its magnetic response and its chemical reactivity. For instance, Co exhibits a ferromagnetic response at room temperature because of the unpaired electrons in the d shell. Moreover, the incomplete d shell gives rise to the Co chemical reactivity. Under ambient pressures, Co tends to react with Oxygen forming a thin oxide layer at the surface. This oxide layer prevents the rest of the atoms from the oxidation, therefore Co is commonly considered a “stable” element.

Co oxides stoichiometry depends on the Co oxidation states. CoO is formed from Co^{2+} , whereas Co_3O_4 involves both Co^{2+} and Co^{3+} in a normal spinel structure with Co^{2+} ions in tetrahedral interstices and Co^{3+} ions in the octahedral interstices (illustrated in Fig.1.4).

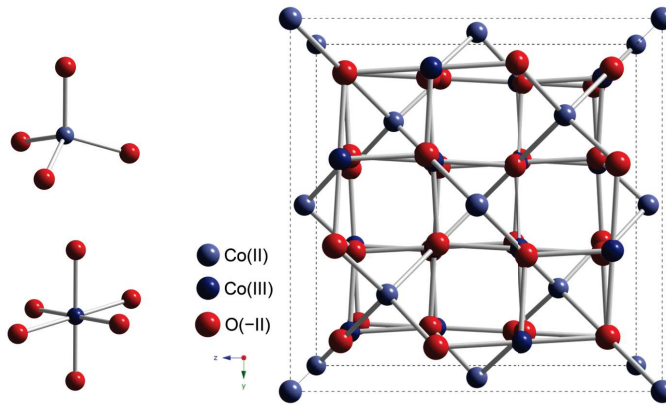


Figure 1.4: Co_3O_4 normal spinel structure. On the left hand side, the tetrahedral and octahedral arrangement of Co are shown.

Both oxides are antiferromagnetic at room temperature: *i.e.* their atomic magnetic moment align antiparallel to one another. This leads to a long-range alternating order resulting into an overall zero magnetization. When an antiferromagnet is placed next to a ferromagnet, a particular coupling is found at the interface. This happens between the antiferromagnetic Co oxide layer and the underlying Co. The coupling results into a further source of magnetic anisotropy which alters the overall magnetic response affecting the

ferromagnetic behaviour.

In order to avoid this coupling, ultra-high vacuum (UHV) chambers and *in-situ* characterization are routinely used. This allows one to reduce Co oxidation down to negligible amounts. In fact, the minor oxygen amount present in UHV chambers, guarantees oxidation safety even for thin films, where the interface effects dominates.

UHV techniques have been used to study the unusually high magnetic anisotropy of ultra-thin ferromagnetic films with thickness $t < t_c$, *i.e.* films showing PMA. The PMA of these films is found to be enhanced when *5d* transition metals are used as substrates. This is due to the spin-orbit coupling between the Co *3d* orbitals and the *5d* orbitals of the substrate. Such interaction strengthens the perpendicular component of the orbital magnetic moment driving the magnetic easy axis out of the film plane. This occurs, for example, in the case of Co films on Ir(111) substrate. Ir(111) single crystals have a lattice parameter of 2.72 Å, *i.e.* 7% larger than that of Co allowing an epitaxial Co growth for the first ML, while further layers progressively relax to follow Co bulk structure.

The naturally high intensity magnetization found in PMA Co/Ir systems makes them ideal candidates for the development of a new class of magnetic recording media [7, 8, 9, 10, 11].

However, the use of such devices requires a high chemical stability which is not typical of thin Co films, as we have already discussed above. For this reason, Co films intercalated between Graphene and Iridium(111) (Gr/Co/Ir systems) have attracted a considerable amount of interest. Such systems provide several advantages: the Ir substrate is a good catalyst for the C-H dissociation. This property can be used to achieve a successful and straightforward CVD growth of Gr using ethylene. Moreover, the Gr layer provides the system with chemical stability under ambient conditions.

Besides these “basics” characteristics, Gr/Co/Ir systems show an enhanced PMA, compared to bare Co/Ir systems [1]. In order to understand the origin of such an enhanced PMA, Gr/Co/Ir systems have been widely investigated. The Co-Gr and Co-Ir interfaces have been characterized and details on the magnetic moments of Co and C [17, 18, 16], and on the long range order of the Co-Ir interface upon annealing [21, 22] are available in literature. In particular, upon intercalation between Gr/Ir the Co-Ir interaction was found to be enhanced and an intermixing of Co-Ir was found to take place at the interface [21].

However, a fine structural characterization of Co films upon intercalation was still missing. Therefore, this thesis aims to describe the intercalation effect on the structural and magnetic anisotropies of Co films. For this reason, several complementary techniques have been exploited. Laboratory techniques such as X-ray Photoemission Spectroscopy (XPS), Low Energy Electron Diffraction (LEED) and Magneto-Optic Kerr Effect (MOKE) have been used

to follow the evolution of the structural arrangement and magnetic response of the Co films. Moreover, synchrotron radiation techniques such as X-Ray Reflectivity (XRR), Grazing Incidence X-ray Diffraction (GIXD), and X-ray Absorption Fine Structure (XAFS) were employed to describe the crystalline structure of the system, to gain chemically sensitive information on the local scale of the system, and to assess the electronic density profile of the systems. In particular, the use of polarized X-rays allowed us to investigate the local anisotropy of Co films upon repeated annealing treatments with a quantitative insight on Co interatomic distances in the directions parallel and perpendicular to the film plane.

Interaction between X-rays and matter

A reliable understanding of the Co films magnetic response requires a careful characterization of their structure, morphology, composition and electronic states. This can be achieved employing a number of complementary state-of-art techniques.

This work is based on the combination of synchrotron radiation X-Ray Reflectivity (XRR), Grazing Incidence X-ray Diffraction (GIXD), and X-ray Absorption Fine Structure (XAFS). In addition, laboratory probes such as X-ray Photoemission Spectroscopy (XPS), Low Energy Electron Diffraction (LEED) and Magneto-Optic Kerr Effect (MOKE) were employed for ancillary characterization and *in-situ* characterization of the films both before and after intercalation and annealing processes.

In order to better understand the experimental results, a description of the physical phenomena underlying these techniques will be provided.

X-rays are electromagnetic waves with energy in the range $0.1\div 100$ KeV. Such waves interact with charged particles and the strength of the interaction is proportional to the ratio of the particle's charge over its mass q/m . Therefore, X-rays interact with matter mainly through the electrons, whereas the interaction with the atomic nuclei is very weak. When X-Rays of energy $h\nu$ interact with matter, three events are possible:

- **photoelectric absorption:** the photon's energy is entirely absorbed and the atom is left in an ionized or excited state. The system, initially with energy E_i , is left with a final energy $E_f = E_i + h\nu$;
- **elastic scattering:** the kinetic energy of an elastically scattered particle is conserved in the center-of-mass frame, but its direction of propagation is modified (by interaction with other particles and/or potentials). Furthermore, while the particle's kinetic energy in the center-of-mass frame is constant, its energy in the lab frame is not. Generally, elastic scattering describes a process where the total kinetic energy of the system is conserved. Among the elastic scattering events, one finds the Thomson scattering, which is the elastic scattering of electromagnetic radiation by

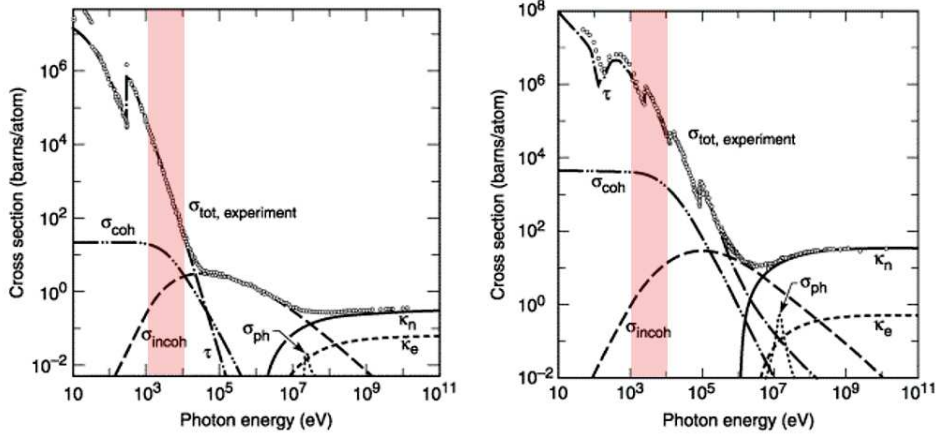


Figure 2.1: Total and differential cross sections for a light (C) and a heavy element (Pb). Photoelectric absorption (solid line) dominates over coherent σ_{coh} and incoherent σ_{incoh} scattering cross sections in the energy range used for this thesis (1-10 keV, see highlighted region). Other absorption processes such as pair production and nuclear absorption are also shown, however they are of minor importance for this work and therefore will not be discussed. Images from the *X-ray data booklet*, Sec.3.1 by J. Kirz.

a free charged particle. The energy of the photon after the scattering $h\nu_f$ equals the initial energy $h\nu_i \Rightarrow \lambda_f = \lambda_i$;

- **inelastic scattering:** the kinetic energy of an inelastically scattered particle is not conserved (in contrast to elastic scattering). An inelastically scattered photon participates in the so called *Compton scattering* and has energy $h\nu_f < h\nu_i \Rightarrow \lambda_f > \lambda_i$.

The probability of each process $W_{i \rightarrow f}$ can be obtained through the Fermi's golden rule. Commonly, instead of the single transition probability from the initial state i to the final state f , one refers to the cross section of the absorption event. The cross section σ can be obtained from $W_{i \rightarrow f}$ by summing over all the possible final states, multiplying by the density of absorbers $1/n_a$ and dividing by the photon flux. Being dependent on n_a , σ is a function of the atomic number. Moreover, it depends on the photon energy $h\nu$, as shown in Fig.2.2.

For each element, the total cross section is given by the sum of all the possible channels. As an example, in Fig.2.1 we present the cross sections of a light element (C) and a “heavy” one (Pb).

In the following we will describe the interaction processes starting from the atomic case and gradually moving towards the bulk limit. For the diffraction

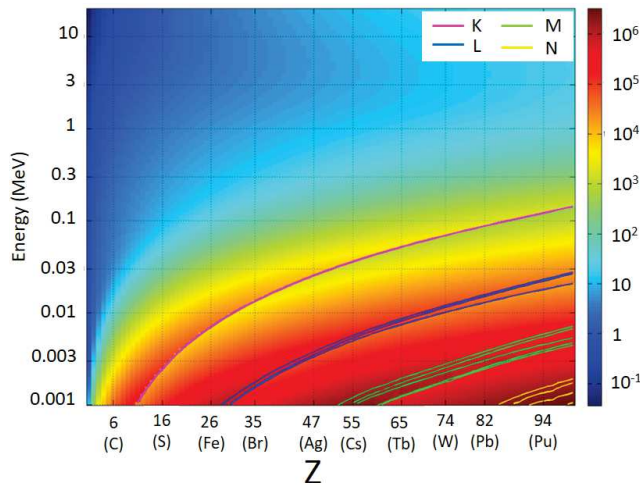


Figure 2.2: Total cross section in barns/atom or in 10^{-24} cm^2 for elements with atomic number $Z < 100$ collected for photons with energies $h\nu = 1 \div 20 \cdot 10^3 \text{ keV}$. The discontinuities in the values are due to absorption edges which are also shown.

theory, further details will be given about scattering by surfaces and interfaces.

Looking at Fig.2.1, one can notice that, in the energy range of interest for this thesis *i.e.* from 1 to 10 keV (see highlighted region), the cross section is dominated by absorption processes. In facts, both for light and heavy elements, the absorption cross section outweighs the other contributions by, at least, one order of magnitude.

Due to absorption, and to other interactions with matter, a light of intensity I_0 travelling in a medium is exponentially attenuated following the Lambert and Beer's equation:

$$I(x) = I_0 e^{-\mu x} \quad (2.1)$$

where $I(x)$ is the intensity after travelling a distance x in the material and μ is the absorption coefficient. $\mu(E)$ can be expressed as a function of the atomic absorption cross section for a photon of energy E , $\sigma(E)$, and the number of atoms per unit volume, n_a :

$$\mu(E) = n_a \sigma(E). \quad (2.2)$$

From $\sigma(E)$ one can find the dependency on the photon flux ϕ_f using:

$$\mu(E) = n_a \frac{1}{\phi_f} \sum_f W_{fi} \quad (2.3)$$

where W_{fi} is the probability of transition between the initial state $|\Psi_i\rangle$ of energy E_i and the final state $|\Psi_f\rangle$ of energy $E_f = E_i + h\nu$.

In general, $\mu(E)$ decreases roughly as $1/(h\nu)^3$ with some sharp discontinuities, as shown in Fig.2.1. These discontinuities are due to quantum effects and cannot be explained in a classical picture. A simplified approach to describe the phenomenon is known as the *semiclassical model*. It is based on

a quantum mechanical treatment of atoms and a classical treatment of the X-ray electromagnetic field. Under these assumptions, w_{fi} is:

$$W_{i \rightarrow f} = \frac{2\pi}{\hbar} |\langle f | H_{int} | i \rangle|^2 \rho(E_f) \delta(E_f - E_i - h\nu) \quad (2.4)$$

where $\rho(E_f)$ is the density of final continuum states, δ is the Dirac's delta function preserving the energy's conservation and H_{int} is the interaction Hamiltonian. For an atom with N electrons, H_{int} depends on the N electrons momenta \mathbf{p}_j through:

$$H_{int} = \frac{e}{m} \sum_{j=1}^N \mathbf{p}_j \cdot \mathbf{A}(\mathbf{r}_j) \quad (2.5)$$

where $\mathbf{A}(\mathbf{r})$ is the vector potential of the electromagnetic field of wavevector \mathbf{k} , and polarization ε , defined as:

$$\mathbf{A}(\mathbf{r}) = A_0 \varepsilon e^{i\mathbf{k}\cdot\mathbf{r}} + cc. \quad (2.6)$$

Inserting Eqs.2.5 and 2.6 in Eq.2.4, The transition probability becomes:

$$W_{i \rightarrow f} = \frac{2\pi e^2}{\hbar m^2} A_0^2 |\langle f | \varepsilon \cdot \mathbf{p} e^{i\mathbf{k}\cdot\mathbf{r}} | i \rangle|^2 \delta(E_i - E_f + h\nu) \quad (2.7)$$

In the one-electron approximation, the initial and final states are considered as single-electron states described by single-particle wavefunctions, while the passive electrons are not participating in the absorption. Therefore one can separate the wavefunction of the $N - 1$ passive electrons from that of the interacting photoelectron $|i\rangle = |\Psi_i^{N-1} \psi_i\rangle$ and $\langle f| = \langle \Psi_f^{N-1} \psi_f|$ and obtain a cross section where the Hamiltonian of the interaction acts only on the single-electron wavefunctions $\psi_{i/f}$. This approach is valid when multiplet splitting or other many body effects can be neglected and it is useful for solids and yields:

$$W_{i \rightarrow f} = \frac{2\pi e}{\hbar m} A_0 |\langle \Psi_f^{N-1} \psi_f | \varepsilon \cdot \mathbf{p} e^{i\mathbf{k}\cdot\mathbf{r}} | \Psi_i^{N-1} \psi_i \rangle|^2 \delta(E_i - E_f + h\nu) \quad (2.8)$$

The delta function in Eq.2.8, provides a probability which is non zero only when the photon energy matches with the energy difference between the initial $|i\rangle$ and some unoccupied final state $\langle f|$. This affects the cross section and, as a consequence, produces the sharp increase in $\mu(E)$ observed whenever $h\nu$ equals some ionization threshold (see Fig.2.1). Such jumps superimpose to the decreasing behaviour of $\mu(E)$: each sharp step identifies an ‘‘absorption edge’’ corresponding to the excitation energy of an electronic level. Each absorption edge is related to a specific atom present in the material and, more specifically, to a quantum-mechanical transition that excites a particular atomic core-orbital electron to the free or unoccupied continuum levels (ionization of

the core orbital). The energies of the edges are unique to the type of atom that absorbs the X-ray, and hence are signatures of the atomic species present in a material.

The edges are named according to the principal quantum number n of the ionized level. For $n = 1, 2, 3, \dots$ one has K, L, M, ... edges. Moreover, to distinguish among photoelectrons coming from the same shell but from different subshells, numerical subscripts are used: $2s$, $2p_{1/2}$ and $2p_{3/2}$ electrons will give rise to L_1 , L_2 and L_3 edges, respectively.

When many atoms are considered, the situation becomes more complex as the photoelectrons reaching the continuum interact with the potentials of the neighbouring atoms, as shown in Fig.2.3. This results into wavy modulations of spectrum near the absorption edges extending several hundreds of eV above the edge. These features are known as X-ray Absorption Fine Structure (XAFS). The energy range in which the XAFS can be observed depends on the average order of the probed system.

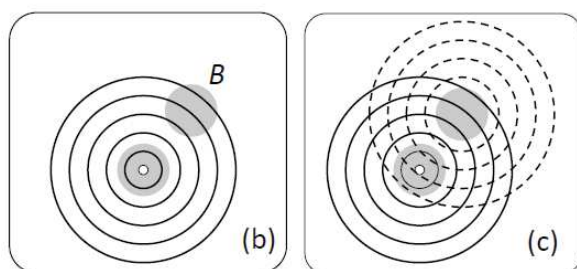


Figure 2.3: a) the wavefunction of the photoelectron expands in the surroundings of the absorber. b) the final state superposition of the outgoing photoelectron with the backscattering wave generated by the potential of a neighboring atom.

When $h\nu$ is near an absorption threshold, the final state can be either a bound state, or a low-lying continuum state. From the bound state one will have features emerging in the pre-edge region, whereas modulations above the edge are due to low energy photoelectrons. These spectral region is commonly called X-ray Absorption Near Edge Spectroscopy (XANES).

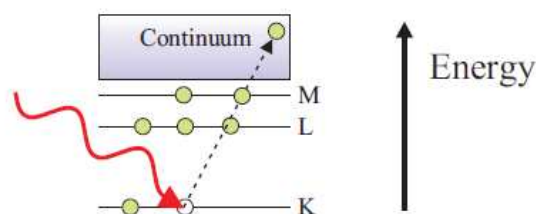


Figure 2.4: The absorption of a photon and the subsequent creation of a core-hole is represented. The electron participating in the process reaches a state in the continuum.

Raising $h\nu$, photoelectrons of higher energies are excited giving rise to the Extended X-ray Absorption Fine Structure (EXAFS). The boundary between these two regions is set at about 80-100 eV above the edge, as shown in Fig.2.5.

Despite there is no real distinction in the studied processes, the division of XANES from EXAFS is useful when it comes to the interpretation and to

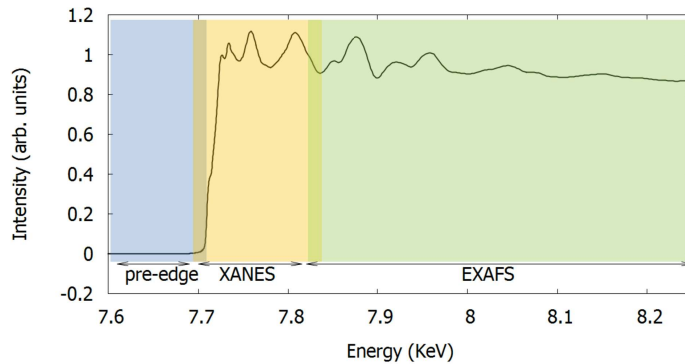


Figure 2.5: XAFS energy regions in the case of Co K edge. The overlap between two neighbouring regions is meant to show that there is no actual border between them.

the formal description of the phenomenon originating of the modulations. In facts, although the underlying theory is the same for both cases, in the XANES region, lower energies photoelectrons are more affected by many-body effects and strong interaction. On the contrary, the high energy of EXAFS photoelectrons allow one to use the Born expansion achieving a simpler description. This can be seen also as a higher sensitivity of EXAFS due to the shorter wavelengths.

In the following, we will give some details about the two regions.

2.0.1 EXAFS

The first approach to EXAFS can be facilitated by a phenomenological picture. When an X-ray photon of high enough energy ionizes an atom, the outgoing photo-electron can be described as a spherical wave of wavelength λ , much as a rock thrown in a pond creates an expanding wave in water. In the same way that water waves reflect off of any obstacles in the pond, the photo-electron can be back-scattered by neighboring atoms, giving rise to an incoming spherical wave, as represented in Fig.2.3. The superposition of all the reflected electron waves at the absorbing atom add either constructively or destructively to the outgoing photoelectron wave and hence modulate the matrix element between the initial and final states that controls the strength of the transition.

As discussed in the previous section, the absorption coefficient $\mu(E)$ depends on the dipole matrix element between the initial electron core state $|i\rangle$ and the photo-electron final state $\langle f|$. The latter, in turn, is a superposition of the outgoing and the incoming spherical waves. The phase relationship between outgoing and incoming waves depends on the photo-electron wavelength and on the inter-atomic distance R . The variation of the phase relationship as a function of photon energy influences the final state amplitude at the core site, giving rise to a modulation of the absorption coefficient. The frequency of the EXAFS oscillations depends on the distance between absorber and back-scatterer atoms while their amplitude is proportional to the number of back-scatterer atoms. Moreover, due to the effects of intrinsic and extrinsic losses,

EXAFS can only measure the local atomic structure over a range limited by the net lifetime (or effective mean free path) of the excited photoelectron.

Two main peculiarities characterize EXAFS: *a)* the selectivity of atomic species, which is achieved by tuning the X-ray energy to the corresponding absorption edge; *b)* the insensitivity to long-range order, due to the short mean free path of the photo-electron, typically limited within 10 Å from the absorber [23].

To obtain a quantitative interpretation of EXAFS one has to properly describe, within the framework of suitable approximations, the process of photo-electric X-ray absorption as well as the final state scattering wavefunction. In the following paragraphs, a series of useful approximations will be discussed.

Electric dipole approximation

Whenever the wavelength of the radiation $\lambda = 2\pi/|\mathbf{k}|$ is much larger than the orbital's dimensions, the interaction Hamiltonian in Eq.2.8 can be expanded in series:

$$e^{i\mathbf{k}\cdot\mathbf{r}} = 1 + i\mathbf{k}\cdot\mathbf{r} + \dots \quad (2.9)$$

The series can then be truncated at the first, dipolar term if $|\mathbf{k}\cdot\mathbf{r}|^2 \ll 1$. This approximation does not hold in the XANES region, whereas it holds for EXAFS around K edges: core orbitals are localized and extend in a very narrow region near the nucleus, therefore their size is much smaller than the X-ray wavelength and guarantees an accurate description. In the case of photons of energy $h\nu = 7 \text{ keV}$, $\lambda = 1.8\text{\AA}$, which is way larger than the spatial extension of the core electrons wavefunctions.

Under the dipolar approximation, the first order of the cross section becomes:

$$\sigma \simeq |\langle \Psi_f^{N-1} \psi_f | \boldsymbol{\varepsilon} \cdot \mathbf{p} | \Psi_i^{N-1} \psi_i \rangle|^2 \rho(E_f). \quad (2.10)$$

and the selection rules of the angular momentum read:

$$\Delta\ell = \pm 1, \quad \Delta s = 0, \quad \Delta j = \pm 1, 0, \quad \Delta m = 0. \quad (2.11)$$

In one-electron transitions, these rules implies that for initial states with *s* symmetry, like K holes ($\ell = 0$), only excitations to *p* orbitals are allowed ($\ell = 1$).

Sudden Approximation

In the EXAFS region, the photoelectron energy is high enough to make the interaction with passive electrons negligible. Therefore, after the factorization of the global wavefunction Ψ^N into $\Psi^{N-1}\psi_i$, one has only to evaluate:

$$\begin{aligned}\sigma &\simeq |\langle \Psi_f^{N-1} | \Psi_i^{N-1} \rangle|^2 |\langle \psi_f | \boldsymbol{\varepsilon} \cdot \mathbf{p} | \psi_i \rangle|^2 \rho(E_f) = \\ &= S_0^2 |\langle \psi_f | \boldsymbol{\varepsilon} \cdot \mathbf{p} | \psi_i \rangle|^2 \rho(E_f).\end{aligned}\quad (2.12)$$

The term S_0^2 is the superposition integral of the passive electrons wavefunctions [23]. It accounts for the difference between Ψ_i and Ψ_f and it usually ranges between $0.7 \div 0.9$.

The total absorption coefficient calculated so far neglects inelastic contributions due to excitation of other outer electrons (*shake up* and *shake-off* processes) in addition to the photoelectron. If one accounts for these further processes, the total μ_{tot} becomes:

$$\mu_{tot}(\omega) = \mu_{el}(\omega) + \mu_{inel}(\omega).\quad (2.13)$$

Therefore the estimate one can have from Eq.2.12 refers only to μ_{el} as it neglects any relaxation of the passive electrons. In this respect, the value of S_0^2 can be seen as a measure of μ_{el} , that is the fraction of total absorption due to elastic events.

Decay

Upon absorption events, the system is left in an atomic excited state, with one of the core electron levels left empty, *i.e.* with a *core hole*, and a photoelectron. The atom will eventually decay into a lower energy configuration filling the core hole with a higher energy electron. The atomic relaxation from the excited state to the final state occurs through *Fluorescence* or *Auger* emission.

- **Fluorescence** occurs when the atomic transition to the ground state involves the emission of a photon. The photon energy equals the energy difference between the initial excited state E_i , and the final ground state E_f : $h\nu_f = E_f - E_i$. Fluorescence photons are labelled according to the quantum number of the “filler” electron. Photons emitted upon *K* edge absorption are labelled as $K_{\alpha,1}$, $K_{\alpha,2}$ and $K_{\beta,1}$ if $2p_{3/2}$, $2p_{1/2}$ and $3p_{3/2}$ electrons are involved, respectively.
- **Auger** electrons can be photoemitted by the atom upon decay, instead of the fluorescence emission. The Auger emission notation includes the location of the initial vacancy, that of the decaying electron and that of the photoemitted electrons (es.: KL_2L_3 if the initial $1s$ core hole is filled with a $2p_{1/2}$ electron while a $2p_{3/2}$ is emitted.).

The two processes are represented in Fig.2.6. Being dependent on the electronic state of the system, these processes have characteristic energies for each atomic species.

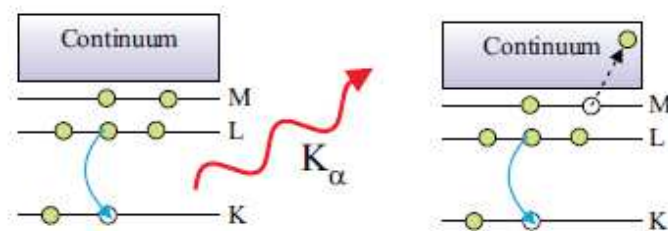


Figure 2.6: Decay channels for a system with a $1s$ core hole. **Left:** an electron with higher energy than the core hole is used to fill the vacancy. If the electron is taken from the $n = 2$ levels, the emitted X-ray will be identified as K_α radiation. **Right:** Auger emission is represented in the case of a KLM transition: the K core hole is filled with an L electron, while an M electron is photoemitted.

Furthermore, depending on the primary absorption event, these decay processes are an indirect way of measuring the absorption spectrum.

The two de-excitation mechanisms are in competition and their relative weight is measured by the *fluorescence yield*:

$$\eta_s = \frac{X_s}{X_s + A_s} \quad (2.14)$$

where s subscripts refers to a given absorption edge (K, L₁, ...) while X and A are the emission probabilities of a fluorescence photon and of an Auger's electron, respectively. The fluorescence yield depends on the atomic number.

The total de-excitation probability per unit time is inversely proportional to the core-hole lifetime. The deeper the core hole and the larger the atomic number Z , the larger is the number of upper levels from which an electron can drop to fill the core hole and consequently the shorter is the core-hole lifetime τ_h (typically $10^{-16} \div 10^{-15}$ s) representing an upper limit for the time allowed to the photo-electron for probing the local structure surrounding the absorber atom.

Because of the time-energy uncertainty relation, the core-hole lifetime is associated with the energy width of the excited state $\Gamma_h \simeq \hbar/\tau_h$ where the width Γ_h contributes to the experimental resolution of the absorption spectra. For a given edge, the larger Z , the lower the lifetime τ_h and the larger the energy width Γ_h .

The EXAFS function

According to Eq.2.12, the fine structure of the absorption coefficient $\mu_{el}(h\nu)$ reflects the variation of the final photo-electron state $\langle \psi_f |$, evaluated at the localized core site of the initial state $|\psi_i\rangle$, as a function of the photon energy $h\nu$. It is the final state $\langle \psi_f |$ that carries structural information. The task of the

theory is calculating the photoelectron final state in molecules and condensed matter and can be done in several different ways. The most effective approach for XAFS is based on the multiple scattering (MS) formalism, which allows a unified interpretation over the entire energy range, from edge to EXAFS. In the EXAFS region the treatment can be much simplified within the single scattering (SS) approximation, which leads to an effective parametrization in terms of structural parameters such as coordination numbers N , distance R and mean square relative disorder σ^2 , and few MS terms.

For concreteness, we consider here the contribution of a K edge to the absorption coefficient.

It is convenient to represent the EXAFS oscillation as a function of the magnitude of the photoelectron wavevector \mathbf{k} :

$$k = \frac{2\pi}{\lambda} = \sqrt{\frac{2m}{\hbar^2} E_k} = \sqrt{\frac{2m}{\hbar^2} (h\nu - E_b)} \quad (2.15)$$

where E_k and E_b are the photoelectron kinetic and binding energy, respectively.

Assuming the sudden approximation and a negligible contribution from inelastic events, in the one-electron picture, the absorption coefficient will take the form of Eq.2.12. Moreover, in the case of an isolated atom and under the dipole approximation, $\mu(\omega)$ will be:

$$\mu_0(\omega) \simeq |\langle \psi_f^0 | \boldsymbol{\varepsilon} \cdot \mathbf{r} | \psi_i \rangle|^2 \quad (2.16)$$

μ_0 represents the atomic absorption coefficient which decreases monotonically for increasing photon energies. The decrease is described by the empirical Victoreen's law $\mu_0 \simeq h\nu^{-3}$.

Non-isolated case

When the absorber is surrounded by other atoms, the photoelectron wavefunction will be scattered back to the origin from the surrounding electrons. Since the photoelectron energy is far above the electron-atom interaction energy, one can use the perturbation theory and write the final state as:

$$\langle \psi_f | = \langle \psi_f^0 | + \langle \delta\psi_f | \quad (2.17)$$

and Eq.2.12 becomes:

$$\sigma \simeq |\langle \psi_f^0 | \boldsymbol{\varepsilon} \cdot \mathbf{r} | \psi_i \rangle + \langle \delta\psi_f | \boldsymbol{\varepsilon} \cdot \mathbf{r} | \psi_i \rangle|^2. \quad (2.18)$$

Then, the oscillatory part of the spectrum χ is defined as the difference between the measured absorption coefficient μ and the atomic absorption coefficient μ_0 , normalized to the latter. In formula, the EXAFS function is written as a function of k and reads:

$$\chi(k) = \frac{\mu - \mu_0}{\mu_0}. \quad (2.19)$$

Substituting to μ and μ_0 Eq.2.18 and 2.18, one has:

$$\chi(k) = \frac{2\text{Re} \int d\mathbf{r} \left[\psi_i(r) \boldsymbol{\varepsilon} \cdot \mathbf{r} \psi_f^{*0}(r) \right] \left[\psi_i^*(r) \boldsymbol{\varepsilon} \cdot \mathbf{r} \delta \psi_f(r) \right]}{\int d\mathbf{r} \left| \psi_i^*(r) \boldsymbol{\varepsilon} \cdot \mathbf{r} \psi_f^0(r) \right|^2}. \quad (2.20)$$

The structural information is contained in the numerator and it is responsible for the oscillations of μ .

In a simple two-body system, where one has an absorber A, a backscatterer B at a distance R, the EXAFS function depends on how a wavefunction evolves upon backscattering. To evaluate it, it is useful to introduce the muffin-tin approximation.

The potential is described by two spherically symmetric potentials centred around A and B, connected through a region of constant potential. Such model is represented in Fig.2.7

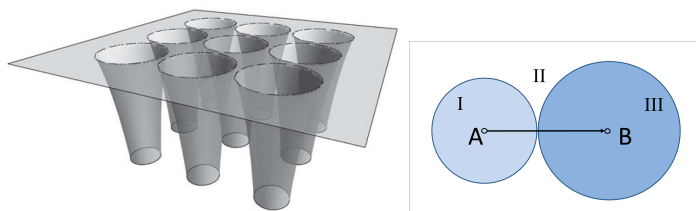


Figure 2.7: Muffin tin potential.

In such a representation, the effect of the potential is calculated in terms of phase-shift due to the change in the potential experienced by the wavefunction at various k on his way to the scatterer and back.

In the case of a K edge, the wavefunction ψ_i is confined at the center of the region I and has s symmetry and $\ell = 0$, while the final state has ψ_f^0 and $\ell = 1$ set by the selection rules. Since the superposition integral has to be evaluated at the origin of region I, also ψ_f^0 needs to be known only in that area. Considering the high energy approximation of Eq.2.17, one needs to know only $\delta\psi_f$ on the entire path back and forth between A and B.

Within region I, $\psi_f = \psi_0$ and the wavefunction corresponds to the isolated atom case. On the border with the constant potential region, for high energies ($kr \gg 1$) the radial part of the wavefunction can be approximated as:

$$\psi_f^0 \cdot \frac{e^{ikr}}{2kr} \cdot e^{i\delta_1} \quad (2.21)$$

where the term $e^{i\delta_1}$ takes into account the phase shift due to the potential changing at the border.

Moving towards the atom B, the photoelectron will interact with the potential of B. If the energy of the photoelectron is high enough, it will only interact

with B's inner electrons in a spatial region small with respect to R. This allows one to describe the propagating wave as a plane wave whose backscattering amplitude equals:

$$f_B(k, \pi) = \frac{1}{k} \sum_{\ell=0}^{\infty} (-1)^\ell (2\ell + 1) e^{i\delta_\ell} \sin \delta_\ell \quad (2.22)$$

where δ_ℓ is the phase shift at the border of region III. At the border of region III, on the way back towards A, the backscattered photoelectron will then be

$$\left(\psi_f^0 \frac{e^{ikr}}{2kr} e^{i\delta_1} \right) f_B(k, \pi) \left[\frac{e^{ikr'}}{r'} \right] \quad (2.23)$$

where the terms in brackets indicate the wave impinging on B, and the terms in square brackets refer to the wave *backscattered* by B after having travelled a distance r' . When $r' = R$, the photoelectron has reached the absorber and its wavefunction can be factorized in:

$$\psi_f^0 \frac{1}{2k} \underbrace{e^{i\delta_1}}_{\text{inter.}} \overbrace{\frac{e^{2ikR}}{R}}^{\text{propag.}} \underbrace{f_B(k, \pi)}_{\text{inter.}} \overbrace{\frac{e^{2ikR}}{R}}^{\text{propag.}} \underbrace{e^{i\delta_1}}_{\text{inter.}} \quad (2.24)$$

where the terms responsible for propagation and interaction have been explicitly identified. Eq.2.24 shows how the perturbation $\delta\psi_f$ generated by the presence of B, can be accounted for as a factorized sequence of interaction factors and propagators. Inserting such result into Eq.2.20, one has:

$$\chi(k) = 3(\boldsymbol{\varepsilon} \cdot \mathbf{r})^2 \frac{1}{kR^2} \text{Im}\{f_B(k, \pi) e^{2i\delta_1} e^{2ikR}\} \quad (2.25)$$

which can be rewritten, grouping the phase terms

$$f_B(k, \pi) e^{2i\delta_1} = |f_B(k, \pi)| e^{i\phi} \quad (2.26)$$

or, in the purely real form,

$$\chi(k) = 3(\boldsymbol{\varepsilon} \cdot \mathbf{r})^2 \frac{1}{kR^2} |f_B(k, \pi)| \sin(2kR + \phi(k)). \quad (2.27)$$

The first term of Eq.2.27, is quite important since because of it, EXAFS is sensitive to structural anisotropies. In facts, this term originates an angular dependence of $\chi(k)$ which can be expressed through:

$$\chi(k, \theta) = \sum_j 3 \langle \cos^2 \theta_j \rangle \chi_j(k) \quad (2.28)$$

where j is the number of neighbouring atomic shell¹, $\chi_j(k)$ is the isotropic contribution of the j^{th} shell and θ_j is the angle between the ε and the absorber-scatterer vector. Averaging upon the in-plane angles one obtains: $\langle \cos^2 \theta_j \rangle = \cos^2 \beta \sin^2 \alpha + (\sin^2 \beta \cos^2 \alpha)/2$ where β is the angle between the absorber-scatterer vector and the normal to the layer plane, while α is the angle made by ε and the layer plane [24]. This effect provides XAFS with directional sensitivity as this term may vanish for some of the atoms around the absorber. For instance, it vanishes for in-plane contributions ($\beta = 90^\circ$) investigated with perpendicular polarization ($\alpha = 90^\circ$). Moreover, when the angular term vanishes, the effective number of atoms observable N_j^{eff} with a given polarization is smaller than the number of atoms surrounding the absorber N_j . Therefore, the effective coordination number of the shell must be taken into account when comparing measurements collected with different polarization directions.

The anisotropic absorption of polarized-XAFS can be used to selectively probe the local atomic structure along specific directions in asymmetric systems, e.g. layered systems, surfaces, interfaces. In evaluating the structural anisotropy of thin films, polarized-XAFS can be exploited to specifically discriminate details of the atomic structure along different crystallographic directions.

Besides the first term, Eq.2.27 shows how the EXAFS signal follows a sinusoidal behaviour in k space. The oscillation amplitude is modulated by the scattering amplitude $f_B(k, \pi)$. Its frequency, $2R$, depends on the interatomic distance travelled by the photoelectron, and is perturbed by the k -dependent shift $\phi(k)$. In general, for low Z values the backscattering amplitude decreases fast and monotonously when k increases. On the contrary, for high Z the amplitude of $\chi(k)$ becomes higher at high k values, and the overall behaviour becomes more and more structured. The behaviour of the scattering amplitude and phase-shift provides XAS techniques with chemical sensitivity to neighbouring atoms.

The plane wave picture is useful to explain the phenomenon. However, nowadays it is common practice to approach the theoretical EXAFS description using spherical waves. This allows one to simulate the propagation in a more accurate and realistic way. For spherical waves, amplitudes and phase-shifts depend weakly on the interatomic distance: $\phi(k, r)$, $|f_B(k, \pi, r)|$ [23].

Moving to many-atoms interactions, one can extend the results obtained so far by summing up all the contributions of single scattering between any possible pair. Of course, this holds only until the multiple scattering events can be neglected. Under this assumption, $\chi(k)$ writes:

¹An atomic shell is made up of all the atoms placed around the absorber at the same distance R_j . Each shell contains N_j atoms depending on the crystalline arrangement around the absorber. N_j is said to be the coordination number of the shell. The reason for the introduction of such concept will be clarified later in the text.

$$\chi(k) = \frac{1}{k} \sum_j \frac{1}{R_j^2} \text{Im}\{f_j(k, \pi) e^{2i\delta_1} e^{2ikR_j}\} \quad (2.29)$$

with the sum running over all atoms and R_j being the distance between the j^{th} atom and the absorber.

Inelastic effects

As far as inelastic losses are concerned, one should distinguish two types of events: intrinsic losses (due to many-body interactions within the absorber atom) and extrinsic losses (linked to the photoelectron mean free path).

Intrinsic losses manifest themselves as multiple excitation in the absorber atom and produce alteration in the photoelectron energy. This results into a reduction of the coherent signal and a decrease in the superposition integral S_0^2 . Therefore, this effect is taken into account whenever the value of S_0^2 is considered to be less than unity.

Extrinsic losses are due to the scattering experienced by the photoelectron on its way to the scatterers and back and can be linked to its mean free path λ . This can be thought as made up of two contribution: the finite core-hole lifetime τ_h , defining the distance $\lambda_h = \nu\tau_h$ travelled by the photoelectron before the absorber relaxes into a lower energy state; and the energy dependent electron mean free path λ_e accounting for inelastic collisions with electrons belonging to neighbouring atoms. The global value of λ equals:

$$\frac{1}{\lambda} = \frac{1}{\lambda_h} + \frac{1}{\lambda_e} \quad (2.30)$$

In the EXAFS energy region, the major contribution comes from λ_e and its effects are taken into account through an exponential decay factor $\exp(-2R_j/\lambda(k))$. The EXAFS formula accounting for inelastic phenomena is:

$$\chi(k) = \frac{S_0^2}{k} \sum_j \frac{e^{(-2R_j/\lambda(k))}}{R_j^2} \text{Im}\{f_j(k, \pi) e^{2i\delta_1} e^{2ikR_j}\} \quad (2.31)$$

Typical values of $\lambda(k)$ are in the range $5 \div 15$ Å. The exponential damping increases with R_j , making the EXAFS sensitive to a region extending up to few Å around the absorber.

In order to simplify the calculations, one can group together atoms of the same element, placed at the same distance from the absorber. These N_s atoms at distance R_s will be grouped in the same *coordination shell*. The expression for $\chi(k)$ can therefore be written as:

$$\chi(k) = \frac{S_0^2}{k} \sum_s N_s \text{Im}\{f_s(k, \pi) e^{2i\delta_1} \frac{e^{-2R_j/\lambda(k)}}{R_s^2} e^{2ikR_s}\} \quad (2.32)$$

where the sums run over the different shells. Eq.2.32 is the standard XAFS formula.

Disorder effects

The description given so far refers to a system of frozen atoms at their equilibrium positions. However, this is not physical, as the thermal vibrations can displace the atoms from their “frozen” positions. Since the period of thermal vibrations $\tau_{th} \simeq 10^{-12}$ s is much larger than the photoelectron time of travel along the EXAFS paths ($\simeq 10^{-16} \div 10^{-15}$ s), each EXAFS spectrum samples a very large number of instantaneous atomic configurations, corresponding to a distribution of instantaneous interatomic distances for each scattering path.

The distribution of interatomic distances can be modified by the presence of structural disorder. This can give rise to distorted coordination shells having slightly different interatomic distances. Alternatively, structural disorder can manifest itself through different sites for the absorbing atom.

This can be accounted for through the *effective EXAFS distribution* $P(r, \lambda) = \rho(r)e^{-2r/\lambda}/r^2$ in the EXAFS signal:

$$\chi_s(k) = \frac{S_0^2}{k} N_s \text{Im}\{f_s(k, \pi) e^{2i\delta_1} \int_0^\infty P(r, \lambda) e^{2ikr} dr\}. \quad (2.33)$$

The fundamental problem of EXAFS analysis is to recover the real distribution $\rho(r)$ from the experimental spectrum $\chi(k)$. Due to the finite extension of the spectrum, no exact solution can be obtained. The problem is usually faced by hypothesising physically sound structural models and refining the parameters of their distribution $\rho(r)$ by best fit of $\chi_s(k)$ to the experimental spectrum [25].

Also, one can have compositional disorder, affecting the atomic species of the neighbours around the absorber.

Multiple Scattering events

Multiple scattering (MS) phenomena are quite weak in the EXAFS region but their contribution is significant for XANES. In order to evaluate multiple scattering events, one can write the absorption coefficient as:

$$\mu(k) = \mu_0(k) [1 + \chi_2(k) + \chi_3(k) + \chi_4(k) + \dots] \quad (2.34)$$

where the terms χ_i identify the number of i legs of the scattering paths. In particular, χ_2 refers to the single scattering (SS) contribution considered so far. This series, not always convergent in the XANES region, converges fast in the EXAFS region. Moreover, it has been demonstrated [26], that each MS contribution can be expressed as oscillatory terms of the form:

$$\chi_p(k) = A_p(k, \{\mathbf{r}\}_p) \sin [kR_p + \phi_p(k, \{\mathbf{r}\}_p)] \quad (2.35)$$

where the terms $\{\mathbf{r}\}_p$ are the set of all vector distances inside the path, R_p is the total path length, and A_p and ϕ_p are functions of the potential.

Fourier Transform and Back Transform

The EXAFS analysis is usually performed with the Fourier transform of the signal $\chi(k)$. This leads to :

$$\chi(r) = \int_{k_{min}}^{k_{max}} dk \chi(k) W(k) k^n e^{2ikr}. \quad (2.36)$$

$W(k)$ is a window function reducing the spurious oscillations coming from an abrupt truncation of the signal, k^n a weight to balance low- and high- k signals. The integration interval is usually chosen so that low- k and high- k values are cut out, thus minimizing effects due to the low reliability and high noise, respectively. $\chi(r)$ is a complex quantity whose modulus $|\chi(r)|$ presents peaks corresponding to the leading frequencies $2r$ of the original $\chi(k)$ signal. However, these peaks do not match the radial distribution function as they carry a shift of about $0.3 \div 0.5 \text{ \AA}$ due to the phase shift contribution $\phi(k)$ of each scattering path. Moreover, the shape of the peaks is affected by the shape of the potentials $\mathbf{A}(\mathbf{k}, \mathbf{r})$ and by the k^n weights. Other than that, the analysis of the Fourier transformed $\chi(R)$ gives important information on the interatomic distances.

Contribution coming from a given set of scattering paths can be singled out through an inverse Fourier transformation:

$$\chi'(k) = \frac{2}{\pi} \int_{r_{min}}^{r_{max}} \chi(r) W'(r) \exp(-2ikr) dr \quad (2.37)$$

again, $\chi'(k)$ is a complex function and carries artefacts due to the Fourier transformation and back-transformation. Therefore, minor discrepancies from the original $\chi(k)$ have to be expected.

However, the first shell contribution usually provides the stronger signal and can be safely interpreted using only single-scattering terms. The outer shells, typically require a multiple-scattering treatment.

In order to obtain the distances R as in Eq.2.32, one needs to know the scattering amplitudes $|f_s(k)|$, phase-shifts $\phi(k)$ and inelastic factors S_0^2 and $\lambda(k)$ for each scattering path.

This can be achieved thanks to *ab-initio* calculations: using advanced codes, one can obtain scattering amplitudes and paths starting from known structures and simulate theoretical EXAFS functions for a given model. The structure of the sample can then be obtained by non linear least square refinement.

2.0.2 XANES

Moving closer to the absorption edge, one progressively enters the XANES region. Here, photoelectrons are less energetic than in the EXAFS region and have longer mean free paths, as shown in Fig.2.8.

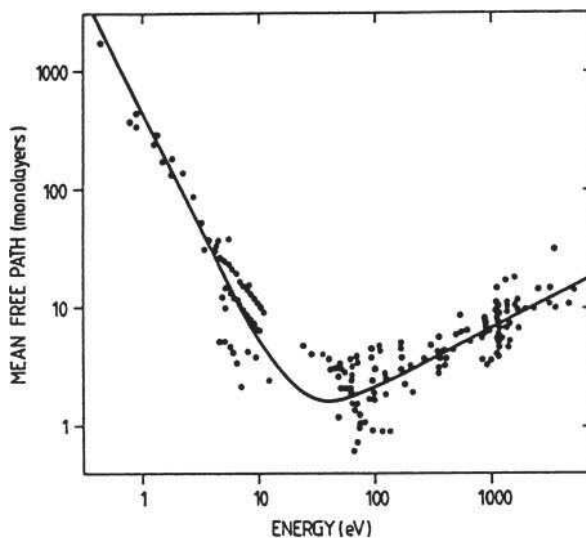


Figure 2.8: Universal curve of inelastic mean free paths of electrons in matter as a function of their kinetic energy (or the distance in eV from the absorption edge). Image from [27].

For this reason, multiple scattering events are definitely relevant and XANES features are sensitive to even weak changes of valence states, coordination chemistry, local structure and ligand symmetry around the absorber. Therefore, XANES can be used to identify chemical species in mixtures and complex materials. As a consequence, even the finest details of the DoS around the Fermi level and of the interatomic potentials affect the XANES signal making the quantitative analysis a complex matter. On the other hand, the strong intensity of XANES features guarantees a satisfactory data collection even in diluted or inhomogeneous samples. Furthermore, the scarce dependency on data statistics, sample quality and X-ray beam intensity makes XANES scarcely sensitive to structural disorder, therefore it is a suitable tool to investigate samples at high temperatures.

XANES spectral features can be divided in three regions, as shown in Fig.2.9:

- 1. Pre-edge** Spectral features emerging at energies below the edge, mainly originate from dipole allowed transition to bound localized states. For this reason, they are generally weaker in metals but particularly evident in oxides. In this region the hybridization of the electronic levels is strongly affected by details of the crystalline field caused by the ligand geometry. This gives rise to large differences also for elements in the same valence state but

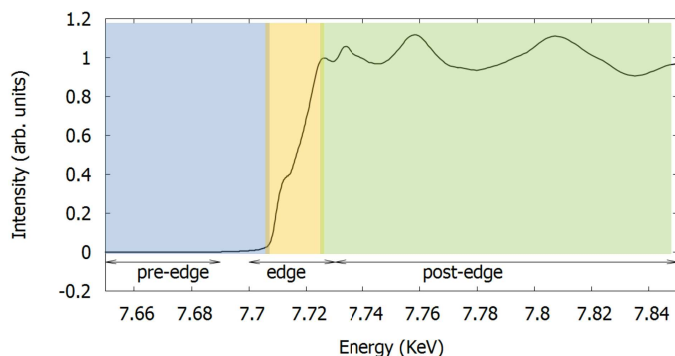


Figure 2.9: XANES regions.

having different local structure.

2. Edge It represents the onset of the continuum state and is related to the oxidation state of the photoabsorber (chemical shift): higher oxidation state raises E_0 even by several eV per oxidation unit. Also the shape of the edge is often characteristic of the chemical environment and ligand geometry.

3. Post-edge At higher energies, this region corresponds to photoelectrons excited in the continuum states. Due to the long mean free path of low energy electrons the absorption signal is dominated by Full Multiple Scattering (FMS) events.

For all the above, it is evident that this technique matches many of the requirements for studying ultra-thin films down to the ML range.

In the following, we will provide the basics for understanding the XANES theory and the principles used in their interpretation.

Semi-quantitative interpretation of XANES

As already mentioned, the FMS theory requires a deep knowledge of inter-atomic potentials and DoS, therefore a quantitative analysis is complex and time consuming. Nevertheless, a semi-quantitative approach needs little effort and leads to information about chemical coordination and composition.

In this thesis the interpretation has been done using the *Linear Combination Analysis (LCA)* combined with ab-initio calculations. LCA represents a simple way to quantify the relative amount of chemical species in mixtures and multiphase compounds. The normalized experimental spectrum μ_{exp} of unknown samples is fitted to a theoretical curve μ_{th} calculated as a linear combination of normalized reference compound spectra:

$$\mu_{exp} = \sum_j \alpha_j \mu_{th}. \quad (2.38)$$

The coefficients α_j represent the fraction of absorbers in the j^{th} environment/ chemical state. The accuracy of LCA lies in the proper set of good

quality spectra measured on reference compounds. In order to obtain reliable results, one should measure such spectra during the same experimental run: this avoids artefacts due to different experimental configurations. Discrepancy in the energy resolution, for example, can smoothen the structural features which are sharper near to the absorption edge and alter the interpretation [28].

Therefore, if the choice of reference spectra is careful enough, LCA is a simple method providing reliable results.

Other methods such as Principal Component analysis (PCA) and deconvolution of the spectral features can be used but fall beyond the purpose of this thesis and will not be described.

Theoretical Approach

In order to run *ab-initio* calculations, the theoretical approach known as the *standard quasiparticle theory* was used. This method considers that a high energy photoelectron interacts dynamically with the gas of other electrons in the material, and due to many-body effects, it behaves no more like a free particle.

Because of many-body interactions, in the XANES region the one-electron approximation used for the EXAFS region cannot be applied to calculate the final states $|f\rangle$. Therefore the absorption $\mu(\omega) \simeq \sum |\langle i | H_{int} | f \rangle|^2$ is not well reproduced.

Another approach consists in treating the photoelectron and the others electrons it interacts with, according to the *final state rule*, e.g. treating them collectively as a *quasiparticle*. Their interaction is accounted for using an energy-dependent complex function $\Sigma(E)$ called the self-energy². Under this approximation, final states are obtained from the solution to the Dyson's equation (i.e. a Schrödinger equation for excited states):

$$h'\psi_f = \left[\frac{p^2}{2m} + V_{Coul} + \Sigma(E) \right] \psi_f = E\psi_f. \quad (2.39)$$

where h' is the non-Hermitian final state Hamiltonian with the prime denoting quantities calculated in the presence of the screened core-hole potential, V_{Coul} is the final state Coulomb potential and $\Sigma(E)$ is the photoelectron self-energy in the quasi-particle approximation.

The use of a complex potential implies that the probability is not conserved. The “leaking away” of probability from the wavefunction effectively introduces a mean free path into the formalism, which means a loss of coherence as the electron propagates through the material. Probability is lost

²This function is sometimes called *optical potential*, in analogy to the way the propagation of light in absorbing media is modelled using a complex index of refraction.

from the main single electron (quasiparticle) channel into a large number of multielectron channels that need not be explicitly calculated.

The crucial difference between ground state electronic structure and excited states is the need for $\Sigma(E)$ and the core-hole for excited states. The self-energy is essentially a dynamically screened exchange interaction, which is the analog of the exchange-correlation potential of ground state density functional theory. Typically, the real part of the self energy, varies by about 10 eV over XAS energies, while the imaginary part is negative and varies by about 5 eV. Thus, this quantity accounts both for (extrinsic) inelastic losses or final-state broadening and systematic peak shifts compared to those calculated with ground state theories [29].

However, this approach neglects intrinsic losses due to many-body excitations and does not account for the core hole's finite lifetime. Through the uncertainty principle, any state with a finite lifetime does not have a sharp energy level, but is better thought of as having a finite width, (e.g., a Lorentzian line shape). In practice, these intrinsic losses lead to an additional broadening of the spectrum and dominate the effective mean free path at threshold [26]. For this reason, the quasiparticle approximation overestimates the absorption at low energies and works well only at high energies.

The Real-Space Multiple Scattering (RSMS) theory solves this problem. Instead of explicitly calculating the final states, it re-expresses the XAS in terms of the photoelectron Green's function or propagator G in real space, which implicitly sums over all final states.

Therefore, using the spectral representation:

$$-\frac{1}{\pi} \text{Im}G = \sum_f |f\rangle \delta(E - E_f) \quad (2.40)$$

one can rewrite the Fermi Golden rule as:

$$\mu \simeq -\frac{1}{\pi} \text{Im} \langle i | \varepsilon \cdot \vec{r}' G(\vec{r}', r, E) \varepsilon \cdot \vec{r} | i \rangle \quad (2.41)$$

which is advantageous for XAS calculations even in perfect crystals, since inelastic losses limit the range probed by XAS experiment to clusters typically of order a few hundred atoms about a given absorption site.

This gives rise to a short range order theory. The cluster size is determined largely by the mean-free path, which is controlled by the core-hole and final state lifetimes. Moreover, at high energies, scattering is relatively weak and perturbation theory in the scattering potential converges well.

The starting point in RSMS theory is the separation of the potential into contributions from "scattering potentials" v_r localized on each atomic site \vec{R}

$$V'_{coul} + \Sigma(E) = \sum_R v_R(\vec{r} - \vec{R}). \quad (2.42)$$

Within the MS theory, the propagator

$$G(\vec{r}', \vec{r}, E) = \Sigma_{L,L'} R_L(\vec{r}') G_{L,L'} R_{L'}(\vec{r}) \quad (2.43)$$

can be separated so that the expression for μ can be reduced to a calculation of atomic dipole-matrix elements of the form $M_L = \langle i | \varepsilon \cdot \vec{r} | L \rangle$ and a propagator matrix $G_{L,L'}(E)$:

$$\mu(E) = -\frac{4\pi e^2 \omega}{c} \text{Im} \sum_{LL'} M_L(E) G_{LL'}(E) M_{L'}(E) \quad (2.44)$$

where $L = (l, m)$ denotes the angular momentum variables.

The calculation of the scattering potentials simplifies for electrons even of moderate energy. Thus, at high energies self-consistency is not important. However, this approximation is inadequate for XANES where self-consistent field (SCF) calculations are almost always necessary. That is, the potentials, electron densities and the Fermi energy are iterated until they are self-consistent.

In RSMS theory, the propagator $G_{LL'}$ naturally separates into intra-atomic contributions from the central atom G^0 and MS contributions from the environment G^{sc} yielding $G = G^0 + G^{sc}$. Following this separation, μ becomes:

$$\mu = \mu_0(1 + \chi) \quad (2.45)$$

Hence, the structure in the XAS μ depends both on the atomic background μ_0 and on the fine structure χ due to MS:

$$\chi = \text{Im} \chi = \text{Im} T r_m G_{LL'}^{sc} \quad (2.46)$$

where the scattering contribution is given by

$$G^{sc} = e^{i\delta} [1 - G^0 T]^{-1} G^0 e^{i\delta'} \quad (2.47)$$

where δ are partial-wave phase shifts. These results are consistent with the experimental definition of XAFS $\chi = (\mu - \mu_0)/\Delta\mu_0$ with $\Delta\mu_0$ jump in the atomic background absorption. For XANES, however, the MS expansion must generally be carried to very high or all orders (full MS), e.g. by matrix inversion.

The matrix $G_{LL'}$ can also be expressed as a sum over all MS paths that a photoelectron can take away from the absorbing atom and back, and thus, gives rise to the path expansion:

$$G^{sc} = e^{i\delta'} [G^0 T G^0 + G^0 T G^0 T G^0 + \dots] e^{i\delta} \quad (2.48)$$

where the successive terms represent single, double, ..., n -scattering processes. This expansion converges rapidly for EXAFS but it is not always reliable for XANES.

In general, one needs a combination of full multiple scattering and the path expansion to cover all energies of interest in XAS.

Due to the large dimension of G , exact calculations with the path expansion can only be carried out for a few low-order MS paths

To overcome this computational bottleneck, an efficient method based on the Rehr–Albers (RA) scattering matrix formalism has been devised [26]. The RA approach yields curved-wave calculations of the effective scattering amplitude $f_{eff}(k)$ (from which the FEFF code takes its name) in terms of a separable representation of the free propagator $G^0(E)$. With this representation the MS expansion can be re-expressed as a sum over MS paths R in a form identical to the original EXAFS equation:

$$\chi(k) = S_0^2 \sum_R \frac{|f_{eff}(k)|}{kR^2} \sin(2kR + \Phi_k) e^{(-2R/\lambda_k)} e^{-2\sigma^2 k^2} \quad (2.49)$$

except that all quantities must be redefined to include curved wave and many-body effects implicitly. Here the electron mean free path $\lambda(k) \simeq k/(|Im\Sigma| + \Gamma/2)$ is calculated in terms of the self-energy and core-hole lifetime, while σ accounts for the thermal and structural disorder, representing the rms fluctuation in the effective path length $R = R_{path}/2$.

At high energy, effects of thermal and structural disorder are of crucial importance. In facts, they lead to a strong damping of the fine structure accounted for by a *Debye-Waller* factor $\exp(-2\sigma^2 k^2)$ and by the photoelectron mean free path $\lambda(k)$. In XANES, where k is small (a few \AA^{-1}), the Debye–Waller factor is of order unity, hence these terms are usually considerably less important than in diffraction experiments (see next section and Ref.[29]). In this thesis, the refinement of these parameter is performed through the FEFF8 code [30].

2.1 X-ray Scattering

The scattering events of X-rays in matter can be described in terms of the classical theory. In facts, an electromagnetic field can make a charge oscillate by exerting a force on it. As a consequence, that particle will emit a radiation whose frequency will be linked to the particle’s frequency of oscillation.

In the simplest case, one can consider a single free electron of charge e and mass m , and an X-ray beam. The reference system can be chosen so that the origin will be where the electron lies and the \mathbf{x} direction will follow the electromagnetic wave’s propagation.

The scattered wave can be evaluated in a point P at distance R from the electron and at an angle ϕ with \mathbf{x} . The \mathbf{y} direction can be chosen so that P lies in the \mathbf{x} - \mathbf{y} plane. For unpolarized beams, the polarization can be oriented in any direction in the \mathbf{y} - \mathbf{z} plane with equal probability. Therefore we can choose one ($\boldsymbol{\varepsilon}_0$) and later average over all the directions.

The beam, of frequency ν , will have instantaneous electric fields projected along \mathbf{y} and \mathbf{z} given by:

$$E_{0,y} = \varepsilon_{0y} \sin(2\pi\nu t), \quad E_{0,z} = \varepsilon_{0z} \sin(2\pi\nu t). \quad (2.50)$$

The y component will exert a force on the electron which will accelerate according to:

$$a_y = \frac{f_y}{m} = \frac{e\varepsilon_{0y}}{m} \sin 2\pi\nu t. \quad (2.51)$$

Such particle, in its acceleration, will radiate an electric field at a distance R equal to:

$$E = \frac{ea \sin \alpha}{c^2 R} \quad (2.52)$$

with c being the speed of light and α the angle between \mathbf{R} and \mathbf{a} . E will lie in the plane of \mathbf{R} and \mathbf{a} with its magnitude depending on the projection $a \sin \alpha$. The last expression can be used to evaluate the instantaneous field produced by the accelerated particle. Analogously to Eq.2.50, one gets:

$$E_y = \frac{e^2 \varepsilon_{0y}}{mc^2 R} \cos \phi \sin(2\pi\nu t) = \varepsilon'_y \sin(2\pi\nu t) \quad (2.53)$$

and, for E_z :

$$E_z = \frac{e^2 \varepsilon_{0z}}{mc^2 R} \sin(2\pi\nu t) = \varepsilon'_z \sin(2\pi\nu t). \quad (2.54)$$

The amplitude E at the point of observation will then be given by:

$$\varepsilon^2 = \varepsilon_y^2 + \varepsilon_z^2 = \frac{e^4}{m^2 c^4 R^2} (\varepsilon_{0z}^2 + \varepsilon_{0y}^2 \cos^2 \phi). \quad (2.55)$$

Averaging over the possible polarization direction leads to:

$$\langle \varepsilon^2 \rangle = \langle \varepsilon_{0y}^2 \rangle + \langle \varepsilon_{0z}^2 \rangle \quad (2.56)$$

whose solution has to fulfil

$$\frac{1}{2} \langle \varepsilon^2 \rangle = \langle \varepsilon_{0y}^2 \rangle = \langle \varepsilon_{0z}^2 \rangle \quad (2.57)$$

since there is no preferred orientation. Finally one is left with:

$$\langle \varepsilon^2 \rangle = \langle \varepsilon_0^2 \rangle \frac{e^4}{m^2 c^4 R^2} \left(\frac{1 + \cos^2 \phi}{2} \right). \quad (2.58)$$

The observable quantity is the intensity I , the mean energy per unit area per unit time:

$$I = \frac{c}{8\pi} \langle \varepsilon^2 \rangle \quad (2.59)$$

with $\langle \varepsilon^2 \rangle$ being the maximum value of a sinusoidal field.

Rewriting Eq.2.58 multiplying both sides by $c/8\pi$, one has:

$$I = I_0 \frac{e^4}{m^2 c^4 R^2} \left(\frac{1 + \cos^2 \phi}{2} \right). \quad (2.60)$$

that is the Thomson scattering equation, giving the intensity of classical scattering by a single free electron. The term $(1 + \cos^2 \phi)/2$ is the polarization factor and describes the scattering of unpolarized light. The factor $e^4/m^2 c^4 \simeq 10^{-26} \text{ cm}^{-2}$ gives the order of magnitude of the scattered wave moving further from the scatterer.

2.1.1 Many particles system

If our system is made up of several electrons, we can evaluate the scattered field summing up the single scattered waves. In general, for a plane wave of wavelength λ impinging on n electrons, at P one will have an electric field for each scattered wave equal to:

$$E_n = \varepsilon_n \cos \left(2\pi\nu t - \frac{2\pi X_n}{\lambda} \right) \quad (2.61)$$

if X_n is the path length travelled by the wave on its way to P, across the n^{th} electron. Expanding the sum in the cosine function, E_n takes the form:

$$E_n = \varepsilon_n \cos(2\pi\nu t) \cos \left(\frac{2\pi X_n}{\lambda} \right) + \varepsilon_n \sin(2\pi\nu t) \sin \left(\frac{2\pi X_n}{\lambda} \right) \quad (2.62)$$

In principle, E_n are different from one another: therefore, the global field in P results to be:

$$E = \sum_n E_n = \cos 2\pi\nu t \sum \varepsilon_n \cos \frac{2\pi X_n}{\lambda} + \sin 2\pi\nu t \sum \varepsilon_n \sin \frac{2\pi X_n}{\lambda}. \quad (2.63)$$

If we define:

$$\sum \varepsilon_n \cos \frac{2\pi X_n}{\lambda} = \varepsilon \cos \phi \quad (2.64)$$

$$\sum \varepsilon_n \sin \frac{2\pi X_n}{\lambda} = \varepsilon \sin \phi$$

the instantaneous field becomes:

$$E = \varepsilon (\cos 2\pi\nu t \cos \phi + \sin 2\pi\nu t \sin \phi) = \varepsilon \cos(2\pi\nu t - \phi) \quad (2.65)$$

Again, the observable is the intensity which depends on the square of ε :

$$\varepsilon^2 = \left(\sum \varepsilon_n \cos \frac{2\pi X_n}{\lambda} \right)^2 + \left(\sum \varepsilon_n \sin \frac{2\pi X_n}{\lambda} \right)^2 \quad (2.66)$$

from this, the intensity reads

$$I = \frac{c}{8\pi} \varepsilon^2. \quad (2.67)$$

Hence we are only interested in ε^2 , which is given by:

$$\varepsilon^2 = \left(\sum \varepsilon_n \cos \frac{2\pi X_n}{\lambda} \right)^2 + \left(\sum \varepsilon_n \sin \frac{2\pi X_n}{\lambda} \right)^2. \quad (2.68)$$

In diffraction experiments, one usually prefers to use the *complex exponential* method, leading to the same result. Using the relation $i = \sqrt{-1}$, one can rewrite Eq.2.61 in the form:

$$E_n = \varepsilon_n e^{i[2\pi\nu t - 2\pi X_n/\lambda]}. \quad (2.69)$$

Given $e^{-ix} = \cos x - i \sin x$, one has:

$$E_n = e^{i2\pi\nu t} \left(\varepsilon_n \cos \frac{2\pi X_n}{\lambda} - i \varepsilon_n \sin \frac{2\pi X_n}{\lambda} \right) \quad (2.70)$$

and, summing up,

$$E = \sum E_n = e^{i2\pi\nu t} \left(\sum \varepsilon_n \cos \frac{2\pi X_n}{\lambda} - i \sum \varepsilon_n \sin \frac{2\pi X_n}{\lambda} \right). \quad (2.71)$$

By multiplying E by its complex conjugate E^* , one has:

$$EE^* = \left(\sum \varepsilon_n \cos \frac{2\pi X_n}{\lambda} \right)^2 + \left(\sum \varepsilon_n \sin \frac{2\pi X_n}{\lambda} \right)^2 \quad (2.72)$$

which is equal to Eq.2.68 and thus yields $EE^* = E^2$. This demonstrates that with the right use of the complex potential one can calculate the intensity I . In practice, to obtain I one has to write for each scatterer the instantaneous value of the electric field at the point of observation as a complex quantity. After summing up these values, the intensity is given by the product of this sum, multiplied by its complex conjugate times $c/8\pi$.

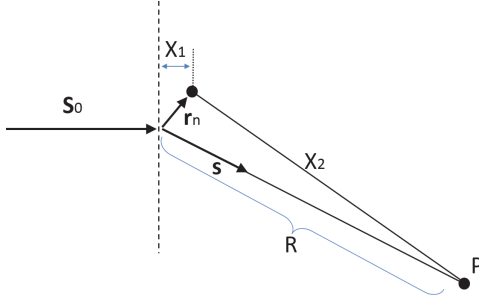


Figure 2.10: Schematic representation of a plane wave scattered by an atom. The origin of the reference system is chosen at the nucleus of the atom. The wavefront S_0 is scattered by an electron in \mathbf{r}_n and the scattered wave is observed from a point P at a distance R from the atom.

Scattering by an atom

In an atom, one has several scatterers localized in a certain region. Choosing our reference system by setting the origin to the atom's nucleus, each electron's position will be identified by the position vector \mathbf{r}_n , as shown in Fig.2.10.

At P , at distance R from the atom, the instantaneous field acting on the n^{th} electron will be:

$$E_0 = \varepsilon_0 \cos \left(2\pi\nu t - \frac{2\pi X_1}{\lambda} \right) \quad (2.73)$$

To account for the phase shift, we can multiply by the classical factor for one electron and consider the total path as $X_1 + X_2$:

$$E_n = \varepsilon_0 \frac{e^2}{mc^2 X_2} \cos \left(2\pi\nu t - \frac{2\pi}{\lambda} (X_1 + X_2) \right). \quad (2.74)$$

Actually this is neglecting a phase shift of π but the same condition will hold for every electron, therefore it is not important, here. If both the source and P are very far from the scattering center, *i.e.* their distance is $\gg r_n$, a plane wave approximation will be adequate. Under this assumption $X_2 \rightarrow R$ and:

$$X_1 + X_2 \rightarrow \mathbf{r}_n \cdot \mathbf{S}_0 + R - \mathbf{r}_n \cdot \mathbf{s} = R - (\mathbf{s} - \mathbf{s}_0) \cdot \mathbf{r}_n. \quad (2.75)$$

In terms of complex potential, the sum of instantaneous fields at P gives:

$$E = \varepsilon_0 \frac{e^2}{mc^2 R} e^{2\pi i[\nu t - R/\lambda]} \sum_n e^{2\pi i/\lambda} e^{(\mathbf{s} - \mathbf{s}_0) \cdot \mathbf{r}_n} \quad (2.76)$$

However, the representation we gave so far is not adequate to describe the elastic and inelastic scattering events.

In facts, we have to consider each electron as a diffuse cloud of negative charge, characterized by a charge density ρ expressed in electron units. Integrating this quantity over the volume of an electron dV , gives $\int \rho dV = 1$. From the wave mechanical treatment, the amplitude of elastic scattering from the element ρdV is equal to ρdV times the amplitude of classical scattering

from one electron. Therefore, the contribution to the scattering from a single electron comes from the integration over the volume occupied by the electron itself. To calculate it, we adapt Eq.2.76 so that instead of electrons placed at \mathbf{r}_n we have charge elements ρdV at positions \mathbf{r} and instead of a sum, we have an integral:

$$E = \varepsilon_0 \frac{e^2}{mc^2 R} e^{2\pi i[\nu t - R/\lambda]} \int e^{2\pi i/\lambda} e^{(s-s_0)\cdot\mathbf{r}} \rho dV \quad (2.77)$$

this equation holds a quantity called the “scattering factor per electron”, typically indicated by f_e :

$$f_e = \int e^{(2\pi i/\lambda)(s-s_0)\cdot\mathbf{r}} \rho dV \quad (2.78)$$

which is the ratio of the amplitude of elastic scattering over the classical scattered amplitude for one electron or, equivalently, it is the amplitude of elastic scattering in electron units.

For core electrons we can assume a spherical symmetry of the charge distribution $\rho = \rho(r)$ and take the origin at the center of the atom. In this case we can write f_e as:

$$f_e = \int_{r=0}^{\infty} \int_{\phi=0}^{\pi} e^{ikr \cos \phi} \rho(r) 2\pi r^2 \sin \phi d\phi dr \quad (2.79)$$

where $k = 4\pi \sin \theta / \lambda$, while $(s - s_0) \cdot r = 2 \sin \theta r \cos \phi$ is shown in Fig.2.11.

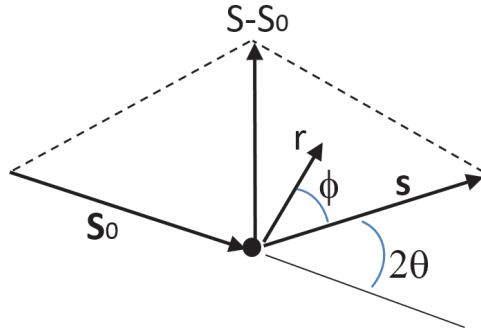


Figure 2.11: Relation between the $\mathbf{s} - \mathbf{s}_0$ vector and the vector \mathbf{r} for an atom centered at O .

Performing the integration over ϕ yields

$$f_e = \int_0^{\infty} 4\pi r^2 \rho(r) \sin \frac{2kr}{kr} dr. \quad (2.80)$$

In the case of an atom with n electrons, one has to sum the several contributions:

$$f_{at} = \sum_n f_e^n = \sum_n \int_0^{\infty} 4\pi r^2 \rho_n(r) \sin \frac{2kr}{kr} dr. \quad (2.81)$$

f_{at} is the atomic scattering factor and represents the amplitude of elastic scattering per atom in electron units. To calculate f_{at} one needs only to know $\rho(r)$, *i.e.* the radial dependence of the electron density in the atom. Given its dependence on k , f_{at} is a function of $\sin\theta/\lambda$. For any atom the relation with the atomic number Z holds:

$$\sum_n \int_0^\infty 4\pi r^2 \rho_n(r) dr = Z \quad (2.82)$$

and $f_{at} \rightarrow Z$ for small values of $\sin\theta/\lambda$.

The description we provided so far has completely neglected absorption, therefore it remains valid only until the wavelength of the X-ray is far from the absorption edges. When absorption events become relevant, it is possible to correct the expression for f as follows:

$$f = f_0 + \Delta f' + i\Delta f'' \quad (2.83)$$

where f_0 is the uncorrected atomic scattering factor, while $\Delta f'$ and $\Delta f''$ are the real and imaginary part of the dispersion correction.

2.1.2 Scattering from a small crystal

Crystals are periodic arrangement of atoms. The periodicity of a 3D crystal can be expressed by three basis vectors $\mathbf{a}_1, \mathbf{a}_2, \mathbf{a}_3$ called crystal axes. The parallelepipedon defined by the crystal axes is the smallest volume which is repeated throughout the crystal and it is called *unit cell*. The volume of each unit cell is $v_a = \mathbf{a}_1 \cdot \mathbf{a}_2 \times \mathbf{a}_3$ whereas its position in the crystal is given by a linear combination of the crystal axes.

The position of every atom in a crystal can be specified by the position of the unit cell in the crystal (relative to the crystal's origin) plus its position in the unit cell (relative to the cell's origin). Hence the position of an atom of type n in the unit cell designated by the indexes m_1, m_2, m_3 is given by the vector:

$$\mathbf{R}_m^n = m_1 \mathbf{a}_1 + m_2 \mathbf{a}_2 + m_3 \mathbf{a}_3 + \mathbf{r}_n. \quad (2.84)$$

The laws of diffraction typically refers to crystallographic planes. The set of planes designated by the Miller indexes hkl , indicates a set of equidistant, parallel planes. One of these passes by the origin and the nearest one intercepts the axes at $a_1/h, a_2/k, a_3/l$.

The set of hkl planes can be indicated also by a single vector \mathbf{H}_{hkl} which is perpendicular to the planes and whose magnitude is equal to the reciprocal of the spacing among them.

\mathbf{H}_{hkl} is expressed in terms of the reciprocal space vectors $\mathbf{b}_1, \mathbf{b}_2, \mathbf{b}_3$ defined as:

$$\mathbf{a}_i \cdot \mathbf{b}_j = \begin{cases} 1, & i = j \\ 0, & i \neq j. \end{cases} \quad (2.85)$$

Hence $\mathbf{H}_{hkl} = h\mathbf{b}_1 + k\mathbf{b}_2 + l\mathbf{b}_3$. If vectors \mathbf{H}_{hkl} are drawn for all values of hkl , the terminal points of these vectors form a new lattice called *reciprocal lattice*. The reciprocal lattice is particularly useful in diffraction. For example, it can be demonstrated that the Bragg's law can be expressed using reciprocal space vectors as: $\mathbf{s} - \mathbf{s}_0 = \lambda\mathbf{H}_{hkl}$.

The graphical representation of this expression of the Bragg's law is known as the Ewald's sphere and is shown in Fig.2.12. The primary beam is represented on the reciprocal lattice by the vector \mathbf{s}_0/λ terminating in the reciprocal lattice origin. \mathbf{s}_0 has magnitude $1/\lambda$ and makes an angle 2θ with the diffracted beam vector \mathbf{s} . Moreover, \mathbf{s}_0 also represents the radius of the Ewald's sphere.

Every point hkl of the reciprocal space lying on the Ewald's sphere surface corresponds to a set of hkl planes for which the Bragg's law is satisfied. These points can be found at the termination of the diffracted beam vector \mathbf{s} originating at the center of the sphere, or at the termination of the \mathbf{H}_{hkl} vector originating at the origin of the reciprocal lattice.

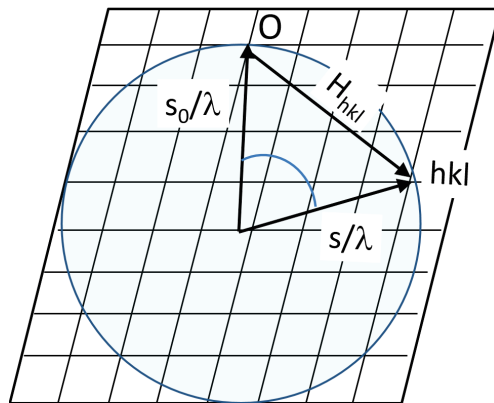


Figure 2.12: Representation of the Ewald Sphere.)

Even if the representation of Fig.2.12 is for the 2D case, the results obtained are valid in the 3D case and the points satisfying the Bragg's conditions can be found anywhere on the sphere's surface.

Consider now the diffraction from a crystal which is small compared to the distances from the X-ray source and to the point of observation. This assumption will allow us to use the plane wave approximation both for the primary beam and for the scattered one.

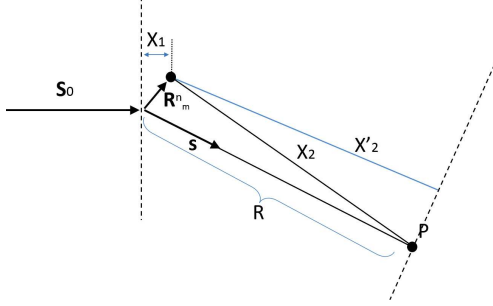


Figure 2.13: Diffraction of a parallel primary beam by a small crystal.

Following the representation in Fig.2.13, we will place our origin at the center of the crystal. The phase of the electric field of the primary beam E_p acting on an atom (m, n) depends upon x_1 , the distance between the atom and the initial wavefront. Following the results obtained in the previous section and neglecting a jump of π in the phase, the instantaneous value of E at P due to elastic scattering from (m, n) is:

$$E_p = \frac{\varepsilon_0 e^2}{m c^2 R} f_n \cos \left(2\pi \nu t - \frac{2\pi}{\lambda} (x_1 - x_2) \right). \quad (2.86)$$

Under the assumption of small crystal, $(x_1 + x_2) \rightarrow (x_1 + x'_2)$. In terms of complex exponential, Eq.2.86 becomes:

$$E_p = \frac{\varepsilon_0 e^2}{m c^2 R} f_n e^{i(2\pi \nu t - \frac{2\pi}{\lambda} [R - (s-s_0) \cdot (m_1 a_1 + m_2 a_2 + m_3 a_3 + r_3])]} \quad (2.87)$$

where the position of the atom has been written as its position in the unit cell plus the position of the unit cell in the crystal.

Summing over all the n atoms in the unit cell and summing again over m_1, m_2, m_3 to include all the unit cells in the crystal one obtains:

$$E_p = \frac{\varepsilon_0 e^2}{m c^2 R} e^{2i\pi(\nu t - \frac{R}{\lambda})} \sum_n f_n e^{(2\pi i/\lambda_0)(s-s_0) \cdot r_n} \sum_{m_1=0}^{N_1-1} e^{(2\pi i/\lambda_0)(s-s_0) \cdot m_1 a_1} \sum_{m_2=0}^{N_2-1} e^{(2\pi i/\lambda_0)(s-s_0) \cdot m_2 a_2} \sum_{m_3=0}^{N_3-1} e^{(2\pi i/\lambda_0)(s-s_0) \cdot m_3 a_3} \quad (2.88)$$

where the first sum runs over the position of all atoms in the unit cell. Since this factor depends on the structure of the crystal it is known as the *structure factor*:

$$F = \sum_n f_n e^{(2\pi i/\lambda_0)(s-s_0)\cdot r_n}. \quad (2.89)$$

The structure factor plays an important role in scattering because it is the only one carrying the atomic positions.

The summations over $m_1 m_2 m_3$ can be written as the result of geometric progressions of the form:

$$S = a + ar + ar^2 + \dots + l = \frac{lr - a}{r - l} \quad (2.90)$$

with a and l first and last term, respectively and r their ratio. Using this result in Eq.2.88, one gets:

$$E_p = \frac{\varepsilon_0 e^2}{mc^2 R} e^{2\pi i(\nu t - R/\lambda)} F \frac{e^{(2\pi i/\lambda)(s-s_0)\cdot N_1 a_1} - 1}{e^{(2\pi i/\lambda)(s-s_0)\cdot a_1} - 1} \frac{e^{(2\pi i/\lambda)(s-s_0)\cdot N_2 a_2} - 1}{e^{(2\pi i/\lambda)(s-s_0)\cdot a_2} - 1} \times \frac{e^{(2\pi i/\lambda)(s-s_0)\cdot N_3 a_3} - 1}{e^{(2\pi i/\lambda)(s-s_0)\cdot a_3} - 1} \quad (2.91)$$

and, multiplying this E_p by its complex conjugate, one gets $E_p E_p^*$ which is equal to the amplitude at P . Accounting for the factor $c/8\pi$, one finally gets the intensity at P , I_p in terms of primary intensity I_0 .

This holds for a primary beam polarized with the electric field perpendicular to the plane of the paper and for a parallelepiped-shaped crystal. In the case of polarization parallel to the plane of the paper, one has to add a factor $\cos^2 2\theta$. On the other hand, for unpolarized beam, ε_0 takes all the orientations perpendicular to s_0 , one then has to consider two components and take their average, as we did in the previous section. This procedure leads to the same result multiplied by a factor $(1 + \cos^2 2\theta)/2$, that is:

$$I_p = I_e F^2 \frac{\sin^2(\pi/\lambda)(s-s_0)\cdot N_1 a_1}{\sin^2(\pi/\lambda)(s-s_0)\cdot a_1} \frac{\sin^2(\pi/\lambda)(s-s_0)\cdot N_2 a_2}{\sin^2(\pi/\lambda)(s-s_0)\cdot a_2} \times \frac{\sin^2(\pi/\lambda)(s-s_0)\cdot N_3 a_3}{\sin^2(\pi/\lambda)(s-s_0)\cdot a_3} \quad (2.92)$$

with $F^2 = FF^*$ and

$$I_e = I_0 \frac{e^4}{m^2 c^4 R^2} \left(\frac{1 + \cos^2 2\theta}{2} \right) \quad (2.93)$$

The Laue's Equations

The intensity depends sharply on the three factors of Eq.2.92. All the three have the form:

$$y = \frac{\sin^2 Nx}{\sin^2 x} \quad (2.94)$$

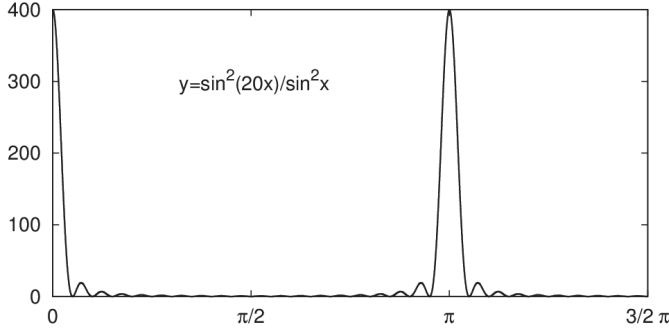


Figure 2.14:
The plot shows
the function $y = \sin^2 20x / \sin^2 x$.

with $x = (\pi/\lambda)(s - s_0) \cdot a_i$. Functions like y have maxima $y = N^2$ everytime $x = n\pi$. These maxima are quite sharp already for $N = 20$ as presented in Fig.2.14, and in a typical crystal the number of atoms is $\gg 20$, therefore we can expect intensity maxima much higher and sharper than those of Fig.2.14 and we can approximate the intensity to zero everytime we are not close to the maxima $x = n\pi$, *i.e.* everytime the three factors of Eq.2.92 are not simultaneously close to their maxima. In formula, the condition to obtain maxima is:

$$\begin{aligned} (\pi/\lambda)(s - s_0) \cdot a_1 &= h'\pi \\ (\pi/\lambda)(s - s_0) \cdot a_2 &= k'\pi \\ (\pi/\lambda)(s - s_0) \cdot a_3 &= l'\pi \end{aligned} \quad (2.95)$$

where h', k', l' are integers. Equivalently, we can write:

$$\begin{aligned} (s - s_0) \cdot a_1 &= h'\lambda \\ (s - s_0) \cdot a_2 &= k'\lambda \\ (s - s_0) \cdot a_3 &= l'\lambda \end{aligned} \quad (2.96)$$

which is the common form of Laue's equations. Diffraction is observed only when these three conditions are simultaneously satisfied. These equations are equivalent to the Bragg's law: $\mathbf{s} - \mathbf{s}_0 = \lambda \mathbf{H}_{h',k',l'}$.

On the other hand, if the crystal is small N is small too, and the peaks of Eq.2.92 will broaden.

Also in the case of multiple crystalline domains, one can expect broad intensity peaks. The average crystallite dimension perpendicular to the reflecting planes can be estimated from the measure of the peak width (FWHM) through the Scherrer equation.

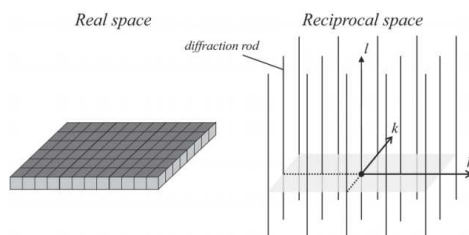


Figure 2.15: Crystal truncation rods (right) representing an ideal layer (left).

A further source of peak broadening is the instrumental resolution. This accounts for imperfect focussing, wavelength width, sample size, penetration of the beam in the sample. These effects have to be taken into account and the raw data can be corrected accordingly in order to ensure the reliability of the data analysis.

2.1.3 Surface diffraction

In order to move towards the surface phenomena, the ideal surface will now be discussed. In particular, we consider a 2D crystal, with infinite spatial extension, and completely independent from substrate and overlayers. In this case, the calculation of the scattering amplitude is similar to that of 3D crystals, but the summation over the unit cells of Eq.2.88 runs only along the two in-plane directions³ \mathbf{a} and \mathbf{b} . This makes the Laue equation involving a_3 (the third one of Eq.2.96) be always satisfied and the amplitude results to be independent from this variable. In reciprocal space, because of the lack of periodicity along l , the diffraction occurs along *rods* instead of points, as shown in Fig.2.15. Since l is varying continuously, different rods are denoted by their integer (h,k) indices.

The next step in the analysis is to consider the free-standing surface with the same structure of a semi-infinite crystal substrate.

Here, the absorption effects should be taken into account as the top layers see a slightly larger intensity than the lower layers. In facts, while along \mathbf{a} and \mathbf{b} all the contributions to the diffraction are the same, due to the attenuation the X-rays have a decreasing intensity for increasing depth.

The summation over all the unit cells than becomes:

³In surface X-ray diffraction one usually chooses the axes of the crystal in such a way that \mathbf{a} and \mathbf{b} are in the plane of the layer, which makes the \mathbf{l} direction of the reciprocal space perpendicular to the surface.

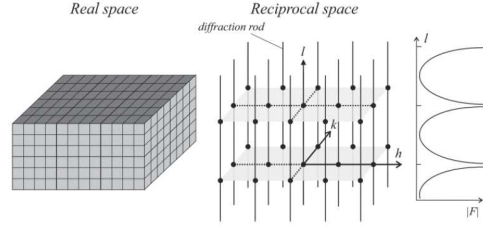


Figure 2.16: Diffraction from an ideal semi-infinite bulk crystal.

$$E_p = \frac{\varepsilon_0 e^2}{m c^2 R} e^{2\pi i(\nu t - R/\lambda)} \sum_{m_1, m_2} e^{(2\pi i/\lambda_0)(s-s_0) \cdot (m_1 a_1 + m_2 a_2)} \quad (2.97)$$

$$\times \sum_{m_3=-\infty}^0 e^{(2\pi i/\lambda_0)(s-s_0) \cdot m_3 a_3} e^{-\alpha m_3} F_{hk}^u(q_z)$$

with α being the attenuation factor. The first sum is the same as for single layer and leads to the (h, k) diffraction rods in reciprocal space. The second summation is the contribution of a single column of identical unit cells, each having the structure factor $F_{hk}^u(q_z)$ with its own phase, and the absorption factor. Evaluating this summation separately, one gets:

$$F_{hkl}^{bulk}(\mathbf{q}) = \sum_{m_3=-\infty}^0 e^{2\pi i m_3} e^{-\alpha m_3} F_{hk}^u(q_z) = \frac{F_{hk}(q_z)}{1 - e^{-2\pi i} e^{-\alpha}}. \quad (2.98)$$

Then the diffracted intensity reads:

$$I_{hk}^{bulk}(q_z) = \left| F_{hk}^{bulk}(q_z) \right|^2 = \frac{|F_{hk}^u(q_z)|^2}{(1 - e^{-\alpha})^2 + 4e^{-\alpha} \sin^2(\pi l)}. \quad (2.99)$$

Neglecting the absorption that only has effects at the bulk Bragg peaks, the amplitude takes the form:

$$\left| F_{hk}^{bulk}(q_z) \right| \approx \left| \frac{F_{hk}^u(q_z)}{2 \sin(\pi l)} \right| \quad (2.100)$$

The amplitude is rising to high values at the bulk Bragg peaks where l is integer, furthermore, due to the presence of the surface, a weak scattering connects the Bragg peaks, called *crystal truncation rods*, shown in Fig.2.16.

However, real crystals do not terminate in a perfectly flat surface: the top layers may relax, undergo reconstructions, give rise to roughness, or a combination of these three effects. To calculate the diffracted amplitude it is convenient to divide the crystal into a bulk and surface part. The total diffracted amplitude can be written as:

$$E = E_0 \sum_{m_1, m_2} e^{2\pi i(hm_1 + km_2)} \left(\sum_{n_3=-\infty}^0 e^{2\pi i n_3 r} e^{-\alpha n_3} F_{hkl}^u(q_z) + \sum_j f_j(\mathbf{q}) e^{-M_j} e^{2\pi i(hx_j + ky_j + lz_j)} \right) \quad (2.101)$$

The left-most summation yields the rod structure of the reciprocal space, the first summation in the brackets is over the part of the crystal having the bulk structure, presented in the previous section. All the contributions from the layers on top of this form the surface contribution:

$$F_{hkl}^{tot}(\mathbf{q}) = F_{hkl}^{bulk}(\mathbf{q}) + F_{hk}^{surf}(q_z) \quad (2.102)$$

The measured intensity will be proportional to:

$$I \propto |F_{hkl}^{tot}(\mathbf{q})|^2 = |F_{hkl}^{bulk}(\mathbf{q}) + F_{hk}^{surf}(q_z)|^2. \quad (2.103)$$

The surface contribution will modify the total structure factor amplitude if the surface structure differs from the structure of the bulk crystal. If the film is incommensurate with the substrate they only interfere in the specular rod, *i.e.* the (0,0) rod.

- The ordering properties of the overlayer can be described using anisotropic Debye-Waller parameters together with partial occupancy (if necessary):

$$F_{hk}^{surf}(q_z) = \sum_j f_j(q_z) \theta_j e^{-M_j} e^{2\pi i(hx_j + ky_j + lz_j)} \quad (2.104)$$

where θ_j is the occupancy of the j^{th} atom and

$$\exp(-M_j) = \exp\left(-\frac{\sigma_{j,\parallel} Q_{\parallel}^2}{16\pi^2}\right) \exp\left(-\frac{\sigma_{j,\perp} Q_{\perp}^2}{16\pi^2}\right) \quad (2.105)$$

with σ_{\parallel} and σ_{\perp} the Debye-Waller parameter along the parallel and perpendicular direction, respectively. The mean square vibration, $\langle u^2 \rangle$, is related to σ by the formula:

$$\sigma = 8\pi^2 \langle u^2 \rangle. \quad (2.106)$$

The formulae presented so far demonstrate that the reconstruction of the electron density depends on the knowledge of the structure factors. Therefore the atomic location can be retrieved once the structure factors. Nevertheless, our detectors only allow us to measure the intensities thus losing the phase information. For this reason one cannot access the crystal structure directly from the data.

The typical procedure consists in building a model and refining the parameters we have discussed so far. The fitting procedure goes on until the best

agreement between data and model is found. In this thesis, the programs used to fit the data are ROD [31] and GenX [32].

The structure factor for a Bragg reflection

Expressing the cell vectors \mathbf{r}_n in terms of components along a_1, a_2, a_3 , by means of fractional coordinates x_n, y_n, z_n , one has: $\mathbf{r}_n = x_n \mathbf{a}_1 + y_n \mathbf{a}_2 + z_n \mathbf{a}_3$. For an hkl reflection, one has to make sure that the Bragg law $\mathbf{s} - \mathbf{s}_0 = \lambda \mathbf{H}_{\mathbf{h}', \mathbf{k}', \mathbf{l}'}$ is satisfied. Hence:

$$F_{hkl} = \sum_n f_n e^{2\pi i (h\mathbf{b}_1 + k\mathbf{b}_2 + l\mathbf{b}_3) \cdot (x_n \mathbf{a}_1 + y_n \mathbf{a}_2 + z_n \mathbf{a}_3)} = \sum_n f_n e^{2\pi i (hx_n + ky_n + lz_n)} \quad (2.107)$$

which is the simplest form for the structure factor of the hkl reflection. If $F_{hkl} = 0$ for a given choice of hkl , the intensity of that reflection will be zero. The reflections with zero intensities allow one to distinguish among the different Bravais lattices. In fcc crystals, for example, each atom of fractional coordinates x_n, y_n, z_n has three corresponding identical atoms at $x_n + \frac{1}{2}, y_n \frac{1}{2}, z_n$, $x_n + \frac{1}{2}, y_n, z_n \frac{1}{2}$, and $x_n, y_n \frac{1}{2}, z_n \frac{1}{2}$. If the unit cell has n atoms, there are $n/4$ groups of 4 identical atoms with the same scattering factor. Therefore, F_{hkl} can be expressed as a sum over such groups:

$$\begin{aligned} F_{hkl} &= \sum_{n/4} f_n [e^{2\pi i (hx_n + ky_n + lz_n)} + e^{2\pi i (h(x_n + 1/2) + k(y_n + 1/2) + lz_n)} + \\ &\quad + e^{2\pi i (h(x_n + 1/2) + ky_n + l(z_n + 1/2))} + e^{2\pi i (hx_n + k(y_n + 1/2) + l(z_n + 1/2))}] \quad (2.108) \\ \Rightarrow F_{hkl} &= \left[1 + e^{i\pi(h+k)} + e^{i\pi(h+l)} + e^{i\pi(k+l)} \right] \sum_{n/4} f_n e^{2\pi i (hx_n + ky_n + lz_n)}. \end{aligned}$$

From the last equation, we have that for m integer $e^{i\pi m} = (-1)^m$. Therefore the factor in squared brackets equals 4 if hkl are unmixed (all odd or all even) or zero if hkl are mixed, independently from the coordinates x_n, y_n, z_n .

$$hkl \text{ unmixed: } F_{hkl} = 4 \sum_{n/4} f_n e^{2\pi i (hx_n + ky_n + lz_n)} \quad (2.109)$$

$$hkl \text{ mixed: } F_{hkl} = 0$$

The missing reflection for mixed hkl allow one to immediately recognize an fcc lattice.

For hcp structures with 2 atoms per unit cell at positions $(0,0,0)$ and $(\frac{1}{3}, \frac{2}{3}, \frac{1}{2})$. Therefore one has:

$$F_{hkl} = f \left[1 + e^{2\pi i [(hx + 2k)/3 + l/2]} \right] \quad (2.110)$$

and the intensity will be proportional to:

$$\begin{aligned} F_{hkl}^2 &= f^2 \left[1 + e^{2\pi i[(hx+2k)/3+l/2]} \right] \left[1 + e^{-2\pi i[(hx+2k)/3+l/2]} \right] = \\ &= f^2 \cos^2 \pi \left(\frac{h+2k}{3} + \frac{l}{2} \right). \end{aligned} \quad (2.111)$$

The structure factors take the form:

$$\begin{aligned} F_{hkl}^2 &= 0 && \text{if } h+2k = 3n, \text{ } l \text{ odd,} \\ F_{hkl}^2 &= f^2 && \text{if } h+2k = 3n \pm 1, \text{ } l \text{ even,} \\ F_{hkl}^2 &= 3f^2 && \text{if } h+2k = 3n \pm 1, \text{ } l \text{ odd,} \\ F_{hkl}^2 &= 4f^2 && \text{if } h+2k = 3n, \text{ } l \text{ even.} \end{aligned} \quad (2.112)$$

Therefore the hcp lattice is recognized by the missing reflection for $l = \text{odd}$ and either $h+2k = 3n$ or $2h+k = 3n^4$.

Thermal vibrations

Eq.2.92 is valid under the assumption that atoms occupy given position in a lattice. Even at room temperature, however, thermal vibration make such positions become the *average* positions. If we aim to derive the expression for I_p accounting for thermal vibrations, we will have to deal with the average position \mathbf{R}_l . At every instant, the atom will be at $\mathbf{R}'_l = \mathbf{R}_l + \delta_l$, *i.e.* it will be around \mathbf{R}_l , displaced by δ_l .

The intensity will then carry an extra term and will take the form:

$$I = I_e \sum_l f_l e^{(2\pi i/\lambda)(\mathbf{s}-\mathbf{s}_0) \cdot (\mathbf{R}_l + \delta_l)} \sum_{l'} f_{l'}^* e^{(-2\pi i/\lambda)(\mathbf{s}-\mathbf{s}_0) \cdot (\mathbf{R}_{l'} + \delta_{l'})} \quad (2.113)$$

and the observed intensity will be:

$$I = I_e \sum_l \sum_{l'} f_l f_{l'}^* e^{(2\pi i/\lambda)(\mathbf{s}-\mathbf{s}_0) \cdot (\mathbf{R}_l - \mathbf{R}_{l'})} \langle e^{(2\pi i/\lambda)(\mathbf{s}-\mathbf{s}_0) \cdot (\delta_l - \delta_{l'})} \rangle. \quad (2.114)$$

if the component of the displacement normal to the diffracting plane u_{sl} is the projection of δ_l along $\mathbf{s} - \mathbf{s}_0$, we can write $(2\pi i)\lambda(\mathbf{s} - \mathbf{s}_0) \cdot \delta_l = ik u_{sl}$, where $k = 4\pi \sin \theta / \lambda$. Using this relation, we can write the average of Eq.2.114 as:

$$\langle e^{(2\pi i/\lambda)(\mathbf{s}-\mathbf{s}_0) \cdot (\delta_l - \delta_{l'})} \rangle = \langle e^{ik(u_{sl} - u_{sl'})} \rangle. \quad (2.115)$$

⁴in the derivation of the last equation we used the fact that if $h+2k = 3n$, then $2h+k = 6n-3k = 3n'$.

If either $k(u_{sl} - u_{sl'})$ is small or follows a Gaussian distribution,

$$\langle e^{ik(u_{sl} - u_{sl'})} \rangle = e^{-(1/2)k^2 \langle (u_{sl} - u_{sl'})^2 \rangle} = e^{-(1/2)k^2 \langle u_{sl}^2 \rangle} e^{-(1/2)k^2 \langle u_{sl'}^2 \rangle} e^{k^2 \langle u_{sl} u_{sl'} \rangle}. \quad (2.116)$$

Using the abbreviations:

$$e^{-(1/2)k^2 \langle u_{sl}^2 \rangle} = e^{-M_l} \quad e^{-(1/2)k^2 \langle u_{sl'}^2 \rangle} = e^{-M_l'} \quad (2.117)$$

and by means of the relation

$$e^{k^2 \langle u_{sl} u_{sl'} \rangle} = 1 + (e^{k^2 \langle u_{sl} u_{sl'} \rangle} - 1) \quad (2.118)$$

we obtain the more compact form:

$$I = I_e \sum_l \sum_{l'} f_l e^{-M_l} f_{l'}^* e^{-M_l'} e^{(2\pi i/\lambda)(\mathbf{s}-\mathbf{s}_0) \cdot (\mathbf{R}_l - \mathbf{R}_{l'})} + \\ + I_e \sum_l \sum_{l'} f_l e^{-M_l} f_{l'}^* e^{-M_l'} e^{(2\pi i/\lambda)(\mathbf{s}-\mathbf{s}_0) \cdot (\mathbf{R}_l - \mathbf{R}_{l'})} \left(e^{k^2 \langle u_{sl} u_{sl'} \rangle} - 1 \right) \quad (2.119)$$

Since $\langle u_{sl} u_{sl'} \rangle \rightarrow 0$ for wide vibrations, the second term is negligible for large values of $\mathbf{R}_l - \mathbf{R}_{l'}$. This implies that large variations of the atomic position will not give rise to sharp peaks. In fact, this produces a diffuse scattering.

The first term of Eq.2.119, is identical to the case in which thermal vibration were neglected, except an attenuation coming from the factors e^{-M_l} , $e^{-M_l'}$. Therefore, to include the thermal vibration in the scattering from a small crystal, we can use the result of Eq.2.92 but with a structure factor:

$$F_T = \sum_n f_n e^{-M_n} e^{2\pi i(hx_n + ky_n + lz_n)} \quad (2.120)$$

In monoatomic crystals, all the M_n are identical, therefore:

$$F_T^2 = F^2 e^{-2M} \quad (2.121)$$

which is the Debye temperature factor. From Eq.2.117, one has $2M = 16\pi^2 \langle u_s^2 \rangle (\sin^2 \theta) / \lambda^2$. Hence the reduction in intensity is stronger for high temperatures, where $\langle u_s^2 \rangle$ is large, and for reflection at high values of $\sin \theta / \lambda$.

Integrated intensity for a small crystal

The atomic structure within the unit cell must be determined from the structure factors. The structure factors could in principle be derived from measurements of the peak intensities.

In reality, imperfections in the crystal and small deviations of the beam collimation produce a measurable diffracted intensity in a narrow region around the Bragg peak. Therefore a more accurate value to deal with is the *integrated intensity* of the peaks [33]. The integrated intensity of a Bragg reflection is measured in a scan, which starts away from the reflection at background level, going through the peak intensity and ending again on the other side on background level. The background-subtracted, total sum of detected photons is then a measure of the integrated intensity. The scan can in principle be in any direction in reciprocal space, but is often chosen to be a rotation of the crystal around an axis normal to the scattering plane, with the detector fixed[34].

Consider a roughly collimated beam oriented roughly at the right angle θ for the planes hkl . The scattered intensity will be observed while rotating the sample at a constant velocity ω about an axis parallel to the planes hkl and normal to the primary beam. The rotation will cover a range centred in the Bragg reflection. During the rotation, the scattered beam will be recorded by a 2D detector which will measure the total diffracted energy E given out from the crystal.

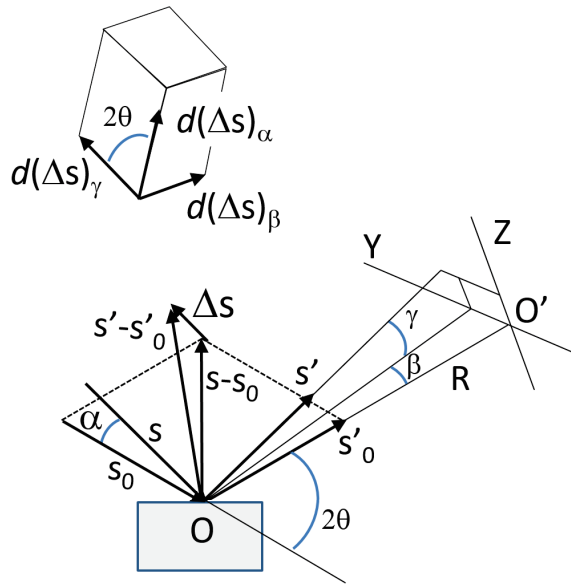


Figure 2.17: Geometry involved in the calculation of integrated intensity scattered from a small crystal rotated at angular velocity ω about an axis normal to the paper.

The geometry is presented in Fig.2.17: the primary beam s_0 impinges on a sample in O and is scattered towards the detector in O' . The scattered beam s reaches the detector surface in perpendicular incidence, after travelling a distance R . The vector s' represents the non perfect collimation of the scattered beam and deviates from s by a small angle β normal to the paper and γ parallel to it. The detector measures the total energy E scattered by the crystal during the rotation which is given by the intensity integrated over the area of the sample and over the time of acquisition:

$$E = \int \int I_p dt dA = \int \int \int I_p dt R^2 d\beta d\gamma. \quad (2.122)$$

The energy diffracted during a rotation with constant velocity ω will be recorded during the rotation. At the end of the rotation, the direction of the diffracted beam will make an angle α with the initial direction. After the rotation has begun, for every dt , the primary beam will move by an angle $d\alpha$ given from the angular velocity given from $dt = d\alpha/\omega$.

Therefore the total diffracted intensity can be calculated as:

$$E = \frac{R^2}{\omega} \int \int \int I_p d\alpha d\beta d\gamma. \quad (2.123)$$

Since, in our example, the primary and diffracted beam differ from the ideal case, the intensity I_p will be given by Eq.2.119, with $(\mathbf{s} - \mathbf{s}_0) = \lambda \mathbf{H}_{hkl} + \Delta \mathbf{S}$:

$$\sin^2 \frac{\pi}{\lambda} (\lambda \mathbf{H}_{hkl} + \Delta \mathbf{S}) \cdot N_1 \mathbf{a}_1 = \sin^2 \pi \left(hN_1 + \frac{\Delta \mathbf{S} \cdot N_1 \mathbf{a}_1}{\lambda} \right) = \sin^2 \frac{\pi}{\lambda} \Delta \mathbf{S} \cdot N_1 \mathbf{a}_1 \quad (2.124)$$

Writing $\Delta \mathbf{S}$ as a vector in reciprocal space, *i.e.* $\Delta \mathbf{S} = \lambda(p_1 \mathbf{b}_1 + p_2 \mathbf{b}_2 + p_3 \mathbf{b}_3)$, Eq.2.124 becomes:

$$\sin^2 \frac{\pi}{\lambda} \Delta \mathbf{S} \cdot N_1 \mathbf{a}_1 = \sin^2 \pi (p_1 \mathbf{b}_1 + p_2 \mathbf{b}_2 + p_3 \mathbf{b}_3) \cdot N_1 \mathbf{a}_1 = \sin^2 \pi N_1 p_1 \quad (2.125)$$

and the total diffracted intensity of Eq.2.122 takes the form:

$$E = I_e \frac{R^2}{\omega} F_T^2 \int \int \int \frac{\sin^2 \pi N_1 p_1}{\sin^2 \pi p_1} \frac{\sin^2 \pi N_2 p_2}{\sin^2 \pi p_2} \frac{\sin^2 \pi N_3 p_3}{\sin^2 \pi p_3} d\alpha d\beta d\gamma. \quad (2.126)$$

Variations in $d\alpha d\beta d\gamma$ result into variations of \mathbf{s}'_0 and \mathbf{s}' perpendicular to \mathbf{s}_0 and \mathbf{s} . In terms of $\Delta \mathbf{S}$ one observes:

$$|d(\Delta S)_\alpha| = d\alpha, \quad |d(\Delta S)_\beta| = d\beta, \quad |d(\Delta S)_\gamma| = d\gamma \quad (2.127)$$

represented in Fig.2.17. These three changes make the terminal point of $\Delta \mathbf{S}$ move describing a volume in reciprocal space given by:

$$dV = d(\Delta S)_\beta \cdot d(\Delta S)_\gamma \times d(\Delta S)_\alpha = \sin 2\theta d\alpha d\beta d\gamma \quad (2.128)$$

Using this change of variable, we can express the integral of Eq.2.126 as a volume integral in reciprocal space:

$$E = I_e \frac{R^2}{\omega \sin 2\theta} F_T^2 \int \int \int \frac{\sin^2 \pi N_1 p_1}{\sin^2 \pi p_1} \frac{\sin^2 \pi N_2 p_2}{\sin^2 \pi p_2} \frac{\sin^2 \pi N_3 p_3}{\sin^2 \pi p_3} dV. \quad (2.129)$$

This representation allows one to perform the integration over any element of volume. Choosing $dV = (\lambda^3/v_a)dp_1dp_2dp_3$ for the terminal point of ΔS , the Bragg's law is verified for $p_1 = p_2 = p_3 = 0$ and the integral is $\neq 0$ only for small values of $p_1p_2p_3$. When this requirement is fulfilled, one can approximate the $\sin^2 \pi p_i \simeq (\pi p_i)^2$ and, since there is only one peak, the integrals are taken from $-\infty$ to $+\infty$:

$$E = I_e \frac{R^2 \lambda^3}{\omega v_a \sin 2\theta} F_T^2 \int_{-\infty}^{+\infty} \frac{\sin^2 \pi N_1 p_1}{(\pi p_1)^2} dp_1 \int_{-\infty}^{+\infty} \frac{\sin^2 \pi N_2 p_2}{(\pi p_2)^2} dp_2 \times \int_{-\infty}^{+\infty} \frac{\sin^2 \pi N_3 p_3}{(\pi p_3)^2} dp_3. \quad (2.130)$$

Now the integrals give N_1, N_2, N_3 and if $N = N_1 N_2 N_3$ is the number of unit cells in the crystal, the diffracted energy reads:

$$E = I_e \frac{R^2 \lambda^3}{\omega v_a \sin 2\theta} F_T^2 N. \quad (2.131)$$

The product of N and v_a is the volume of the small crystal δV . Moreover, using for I_e the value of Eq.2.93, E becomes:

$$E = I_0 \frac{e^4}{m^2 c^4 R^2} \left(\frac{1 + \cos^2 2\theta}{2} \right) \frac{R^2 \lambda^3}{\omega \sin 2\theta} F_T^2 \frac{\delta V}{v_a^2} = \frac{I_0}{\omega} \frac{e^4}{m^2 c^4} \frac{\lambda^3 \delta V}{v_a^2} F_T^2 \left(\frac{1 + \cos^2 2\theta}{2 \sin 2\theta} \right) \quad (2.132)$$

which is the final form of the total diffracted energy upon rotation at angular velocity ω through the Bragg position. Noticeably, this quantity depends on the volume of the crystal. concerning our approximation on the crystal's shape, we can apply Eq.2.132 to small portions of the sample and sum over their contribution until the whole volume has been accounted for. However, the size of the crystal still matters, because we have neglected absorption effects. Therefore, the sample has to be small enough for the absorption to be negligible. Furthermore, the small size allow us to neglect the so-called "extinction" of the diffracted beam due to absorption of the scattered beam on its way out of the sample. Including absorption to the expression would result into a factor $1/\mu$ where μ is the linear absorption coefficient of the medium.

Finally, we point out that Eq.2.132 can be derived even without the plane wave approximation.

In a real experiment, one can measure E and I_0 , thus obtaining F_T^2 . From it, the structure of the crystal and/or the atomic scattering factors can be retrieved.

In this thesis, raw data have been processed with Binoculars [35].

2.1.4 Electron density representations

The approach to crystals diffraction we have used so far, describes the crystals as a periodic arrangements of atoms. After the combining the contribution from each electron into the atomic scattering factors, the crystal behaviour is described by combining the atomic contributions into a structure factor which is representative of a unit cell.

An alternative way to represent the scattering from crystals makes use of electron density distributions. In this approach, atoms are seen as concentrations or peaks in the continuous electron density which varies along the three spatial directions $\rho(xyz)$. This function is triply periodic and can be expressed as a triple Fourier series in the distances x, y, z parallel to the crystalline axes a, b, c .

To calculate the Fourier series of a given $\rho(xyz)$ we can consider that, for fixed x and y , the function is periodic in z and can be expressed as the Fourier series:

$$\rho(xyz) = \sum_{r=-\infty}^{+\infty} C_r(x, y) e^{-2\pi i r z / c}. \quad (2.133)$$

Nevertheless, for fixed x , the electron density is periodic in y . Therefore the coefficients $C_r(x, y)$ must be periodic in y :

$$C_r(x, y) = \sum_{q=-\infty}^{+\infty} C_{qr}(x) e^{-2\pi i q y / b}. \quad (2.134)$$

The same holds for x :

$$C_{qr}(x) = \sum_{p=-\infty}^{+\infty} C_{pqr} e^{-2\pi i p x / a}. \quad (2.135)$$

Putting together the three equations above, one gets:

$$\rho(xyz) = \sum_p \sum_q \sum_r C_{pqr} e^{-2\pi i [p(x/a) + q(y/b) + r(z/c)]}. \quad (2.136)$$

To determine the coefficients C_{pqr} , one starts multiplying both terms for $\exp(2\pi i (hx/a) + (ky/b) + (lz/c))$ and then integrating over $dx dy dz$:

$$\begin{aligned} & \int_0^a \int_0^b \int_0^c \rho(xyz) e^{2\pi i [(hx/a) + (ky/b) + (lz/c)]} dx dy dz = \\ & = \int_0^a \int_0^b \int_0^c \sum_p \sum_q \sum_r C_{pqr} e^{-2\pi i [(p-h)(x/a) + (q-k)(y/b) + (r-l)(z/c)]} dx dy dz. \end{aligned} \quad (2.137)$$

since:

$$\int_0^a e^{-2\pi i(p-h)(x/a)} dx = \begin{cases} a & \text{if } p = h, \\ 0 & \text{if } p \neq h, \end{cases} \quad (2.138)$$

the right-hand side of Eq.2.137 becomes:

$$\int_0^a \int_0^b \int_0^c \rho(xyz) e^{2\pi i[(hx/a)+(ky/b)+(lz/c)]} dx dy dz = abc C_{hkl}. \quad (2.139)$$

If we use Eq.2.107 replacing x_n, y_n, z_n with the fractional coordinates $x_n/a, y_n/b, z_n/c$, the structure factor takes the form:

$$F_{hkl} = \sum_n f_n e^{2\pi i[(hx_n/a)+(ky_n/b)+(lz_n/c)]}. \quad (2.140)$$

If we drop for this relation the sum over the atoms and we adopt the continuous electron density picture, we get:

$$F_{hkl} = \int_0^a \int_0^b \int_0^c \rho(xyz) e^{2\pi i[(hx/a)+(ky/b)+(lz/c)]} dV. \quad (2.141)$$

For this integration any axes (even non-orthogonal to one another) can be used if $dV/V = dx dy dz / (abc)$ holds⁵. The structure factor is then:

$$F_{hkl} = \int_0^a \int_0^b \int_0^c \rho(xyz) e^{2\pi i[(hx/a)+(ky/b)+(lz/c)]} \frac{dx dy dz}{abc} \quad (2.142)$$

and, upon comparison with Eq.2.139, one finally finds out that:

$$VC_{hkl} = F_{hkl} \quad (2.143)$$

i.e. the electron density $\rho(xyz)$ per unit volume can be expressed as a triple Fourier series in which the coefficients are the structure factors:

$$\rho(x, y, z) = \frac{1}{V} \sum_h \sum_k \sum_l F_{hkl} e^{-2\pi i[(hx/a)+(ky/b)+(lz/c)]}. \quad (2.144)$$

This means that each hkl reflection corresponds to a Fourier coefficient of the electron density: a strong reflection reveals a strong contribution of a given hkl -harmonic. In this perspective, the X-ray diffraction is a Fourier analysis of the electronic density in the crystal [33].

Eq.2.144 shows how it is possible to retrieve the electron density from the value of the structure factors. However, from experimental measurements,

⁵ V is the unit cell volume.

one can only access $F_{hkl}F_{hkl}^*$ or, in case F_{hkl} is real, one can measure only its squared value. Due to this, the phase information is lost.

However, from F_{hkl}^2 measurements, it is still possible to retrieve the structural information, using the right boundary conditions and methods which will be discussed in the following sections.

2.1.5 X-Ray Reflectivity

The specular rod (0,0,L) presents some peculiarities making it rather unique. Although it is poorly sensitive to the crystallographic order, it is strongly dependent on the projection of the electronic density in the direction perpendicular to the surface: the *scattering length density* (SLD) $\rho(z)$.

Experimentally, the measurements of the specular rod require to detect the intensity variations of the reflected beam. The reflection of the light reaching a boundary between two media follows the law:

$$\frac{\cos \alpha_i}{\cos \alpha'_i} = \frac{n'}{n}. \quad (2.145)$$

which is commonly known as the Snell's law, even if it was already known six centuries earlier the experiments of the Dutch scientist [36]. In Eq.2.145 the angles of incidence α_i and refraction α'_i are linked to *refractive indexes* of the media, defined as

$$n_i = \sqrt{1 - \frac{\lambda^2 \rho_i(r)}{\pi}} \quad (2.146)$$

with λ wavelength of the radiation considered and $\rho(r)$ SLD of the uniform medium. In vacuum, $\rho(r) = 0$ and Eq.2.146 yields $n = 1$.

When $n > n'$, Eq.2.145 yields a refraction angle α'_i always smaller than the incidence angle α_i . If we decrease α_i until the point where $\alpha'_i = 0$, α_i will equal the "critical angle" α_c . Below α_c , the incident wave is completely reflected. In the range of visible light, this is commonly observed when light travels from a transparent material (water $n = 1.33$ or glass $n = 1.46$) to air $n' \simeq 1 < n$. Since light is prevented from reaching the second medium, the phenomenon is known as "total internal reflection". For X-rays, due to the much shorter wavelengths, the index of refraction can be approximated with $n_{x-ray} \simeq 1 - \frac{\lambda^2 \rho(r)}{\pi} \Rightarrow n \lesssim 1$. Therefore, an Xray beam propagating initially in vacuum ($n = 1$) with an incidence angle equal to the critical angle $\alpha_i = \alpha_c \Rightarrow \alpha'_i = 1$, one has, according to the Snell's law:

$$\cos \alpha_c = n' = 1 - \delta. \quad (2.147)$$

with

$$\delta = \frac{\lambda^2}{2\pi} \rho(r) = \frac{\lambda^2}{2\pi} \frac{e^2}{mc^2} N f(0) \quad (2.148)$$

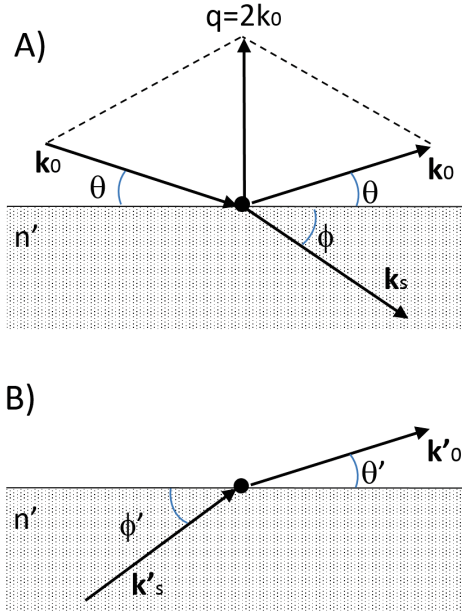


Figure 2.18: **TOP:** A light is shined on a surface of separation between two media of refraction indexes n, n' with wavevector k_i at an angle α_i . The light is then reflected off the surface with wavevector k_f at an angle $\alpha_f = \alpha_i$ or refracted into the second material with wavevector k'_i at an angle α'_i . **BOTTOM:** The light crossing the boundary towards a medium with higher index of refraction is refracted at an angle α_f following the Snell's law (Eq.2.145).

where N is the number of atoms per unit volume and $f(0) = f(q = 0)$ the atomic structure factor for zero momentum transfer.

Typical values of δ vary in the range $10^{-6} \div 10^{-5}$ as a function of the electron density ρ_e of the material. Being $\delta \ll 1$, one can expand Eq.(2.147) as:

$$1 - \frac{1}{2}\alpha_c^2 = 1 - \delta \quad (2.149)$$

$$\Rightarrow \alpha_c \simeq \sqrt{2\delta} = \lambda \sqrt{\frac{e^2}{2\pi m c^2} \rho(r)}.$$

Thus, from the measure of α_c , typically of the order of a few *mrاد*, one can gain information on the electron density $\rho(r)$.

Since $\delta > 0$, and $n \lesssim 1$, incidence angles below the critical value lead to X-rays being completely reflected *outside* off any medium. This phenomenon is known as “total *external* reflection”. This phenomenon is exploited by the beamlines in the X-rays optics: totally reflective mirrors are used to direct and focus X-rays from the storage ring to the sample.

Fresnel Reflection

The picture we provided so far is commonly known as the *Kinematical* theory of diffraction and it is valid over a wide range of experimental conditions. However, when a light impinges on a perfect crystal at an angle θ , the reflected beam will make the same angle with the crystal planes it meets on its way out, as shown in Fig.2.19. This will produce multiple reflections with the same direction as the primary beam which can lead to significant variations of the diffracted intensity. The kinematical theory is valid until the magnitude of the reflections is generally small compared to the primary beam, meaning in many cases. Nevertheless, in some cases multiple reflections produce effects which require a more accurate treatment. The kinematical theory breaks down for nearly perfect single crystals, in grazing incidence, or more generally whenever the effects of absorption, or scattering potential cannot be neglected, the kinematical theory breaks down. These inadequacies led to the development of the *Dynamical* theory, taking into account all these effects [37].

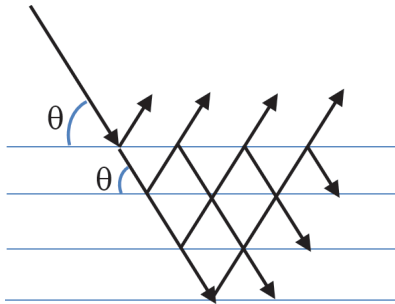


Figure 2.19: X-ray impinging on a perfect crystal with an incidence angle θ . The multiple reflections are also shown.

The first dynamical theory of diffraction was presented by Darwin in 1914: he considered the transmission effects occurring at each lattice plane providing the correct expression for reflected intensities [38]. His theory was then refined by Prins in 1929 including the absorption effects [39]. A second dynamical theory treating the crystal as a periodic distribution of electric dipoles, was developed by Ewald in 1917 [40]. Afterwards, von Laue modified it describing the diffraction in terms of Maxwell's equations in the medium.

The main improvements concern the corrections for light absorption in the medium, the right calculation of phase-shifts⁶, and the multiple reflections.

Consider the experimental geometry shown in Fig.4.7: an incoming one-dimensional plane wave of amplitude 1 and wavevector k_0 impinges on a surface at an angle θ . Part of the wave is reflected at the same angle with amplitude R , while the rest of it is transmitted into the medium with amplitude T and wave vector k_s . For simplicity we will assume that the medium has an abrupt surface and a scattering length density (SLD) uniform and equal to $\rho_s(z)$.

⁶The kinematical theory takes into account only the geometrical phase-shifts.

It can be demonstrated that:

$$k_0 = \frac{2\pi}{\lambda} \sin \theta \quad k_s = \sqrt{k_0^2 - 4\pi\rho_s}. \quad (2.150)$$

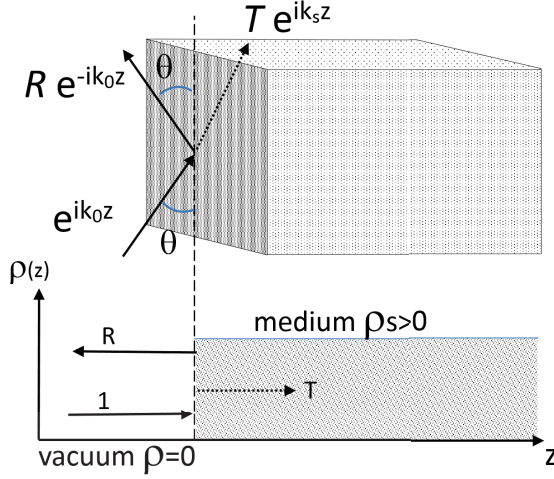


Figure 2.20: Reflection from a semi-infinite crystal. The lower part shows the behaviour of the SLD along z : the step is due to the abrupt surface. The amplitude of the waves and their wavevectors are also shown.

Applying Maxwell's equations and requiring the continuity of E_{\parallel} and B_{\perp} across the interface, one gets the Fresnel's equations for the amplitudes of the reflected and transmitted waves, also known as the reflectance R and the transmittance T_i :

$$R = \frac{k_0 - k_s}{k_0 + k_s}, \quad T = \frac{2k_0}{k_0 + k_s}. \quad (2.151)$$

or, equivalently, in terms of the angles:

$$R = \frac{\theta - \phi}{\theta + \phi}, \quad T = \frac{2\theta}{\theta + \phi}. \quad (2.152)$$

The boundary condition $R + T = 1$ ensures the energy conservation. The quantity of interest for XRR investigation is the square modulus of R , that is the reflectivity $|R|^2$.

The one-dimensional wave number $k_s = \sqrt{k_0^2 - 4\pi\rho_s}$ may vanish for a critical value

$$k_0 = k_c = \sqrt{4\pi\rho_s}, \quad \text{corresponding to: } \theta_c = \arcsin\left(\frac{k_c\lambda}{2\pi}\right). \quad (2.153)$$

In this geometry, Eq.2.151 gives $R = 1$ yielding the total external reflection described above. When this happens, the wave propagating in the medium

becomes a constant: $Te^{ik_s z} = 2$. Therefore in the medium there is actually no wave propagating *along* z anymore.

When $k_0 > k_c$ (or, equivalently $\theta > \theta_c$), the reflectivity decreases rapidly by several orders of magnitude.

On the contrary, for $k_0 < k_c$ (or $\theta < \theta_c$), k_s becomes imaginary and the wave in the medium becomes $Te^{-\kappa z}$, *i.e.* it is exponentially damped with $\kappa = \sqrt{4\pi\rho_s - k_0^2}$. At the same time, in the incident space one gets $e^{ik_0 z} + Re^{-ik_0 z}$, and the complex reflectance R adds an extra phase $\Delta\phi = \arctan(4\pi\rho_s/k_0^2 - 1)^{1/2}$.

When the momentum transfer is large, $q = 2k_0$, k_s can be expanded in a power series of ρ_s keeping terms up to the first order. The reflectance becomes $R \simeq \pi\rho_s/k_0^2$ and the reflectivity:

$$|R|^2 \simeq \frac{\pi^2 |\rho_s|^2}{k_0^4} \quad (2.154)$$

Last equation, sometimes called ‘‘Porod’s q^{-4} law’’, shows how the behaviour of the reflectivity at large q values can provide information on the SLD of the medium.

When absorption effects cannot be neglected, one can account for them adding an imaginary part to the SLD producing an exponential damping of the propagating waves. The refractive index changes accordingly becoming a complex quantity of the form:

$$n = 1 - \delta + i\beta. \quad (2.155)$$

where β is linked to the linear absorption coefficient through the relation $\beta = \mu/2k$ [34] and to δ through the Kramers-Kronig relations [41].

In terms of reflectivity, the imaginary part of the SLD yields:

$$|R|^2 \simeq \frac{\pi^2}{k_0^4} [(\text{Re}\rho_s)^2 + (\text{Im}\rho_s)^2]. \quad (2.156)$$

While no differences can be noticed for large values of k_0 , a small decrease is found in the total external reflection region and the edge around the critical value k_c is found to be rounded.

In total reflection conditions, the transmitted wave is damped and an ‘‘evanescent’’ wave is confined into a layer $\simeq 100\text{\AA}$ -thick below the surface. This results into an enhanced surface sensitivity which makes the grazing incidence geometry especially suited for surface investigations.

The surface sensitivity can be quantified specifying the depth at which a wave intensity I_0 drops to I_0/e . This depth is known as the ‘‘penetration depth’’ Λ . Using the expression for the penetration depth of the incident wave Λ_i writes:

$$\Lambda_i = \frac{1}{2k_s \text{Im}(\phi)}. \quad (2.157)$$

However, in a scattering experiment one measures the intensity of the outgoing wave which is affected by the penetration depth Λ_f (for clarity, the geometry is shown in Fig.2.18). Analogously to the incident wave, one gets:

$$\Lambda_f = \frac{1}{2k'_0 \text{Im}(\theta')}. \quad (2.158)$$

Therefore the wave reaching the detector will carry information on the system within a depth given by:

$$\frac{1}{\Lambda} = \frac{1}{\Lambda_i} + \frac{1}{\Lambda_f}. \quad (2.159)$$

The total Λ is dominated by the smallest between Λ_i and Λ_f : this implies that for grazing incidence, one has a high surface sensitivity even for wide exit angles.

2.1.6 specular reflection from a uniform layer

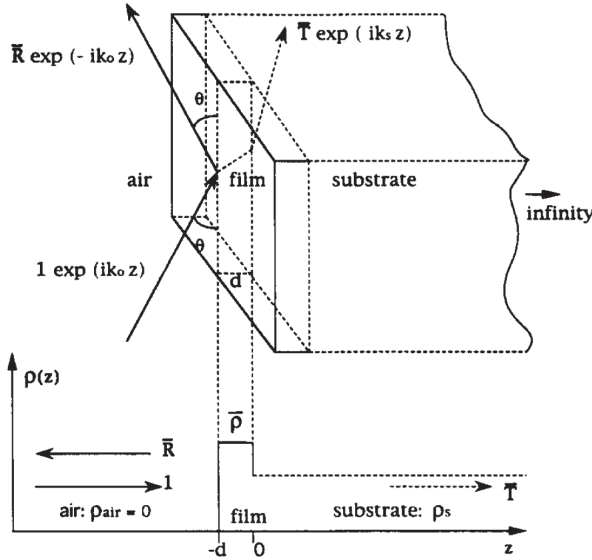


Figure 2.21: Schematic representation of a uniform film on a semi-infinite substrate. The SLD of both the film ρ_f and the substrate ρ_s are considered to be uniform. The lower part of the figure shows the behaviour of the SLD: the steps are due to the abrupt interfaces.

This work, focuses on thin films on single crystal substrate. The simplest way to model such systems is to consider a uniform film with a constant SLD ρ_f on a uniform substrate ρ_s , as shown in Fig.2.21. For such systems, the wave equations read:

$$\psi''(z) + K^2 \psi(z) = 0 \quad (2.160)$$

with $K = k_0$ in vacuum, k_f in the films, k_s in the substrate. The solutions are:

$$\begin{aligned} \psi(z) &= e^{ik_0z} + R_{surf} e^{-ik_0z} & z \leq -d \text{ in vacuum,} \\ \psi(z) &= A \left[e^{ik_fz} + R_{int} e^{-ik_fz} \right] & -d \leq z \leq 0 \text{ in the film,} \\ \psi(z) &= T e^{ik_sz} & z \geq 0 \text{ in the substrate.} \end{aligned} \quad (2.161)$$

The reflectivity comes from the reflectance:

$$R = \frac{-R_{surf} + R_{int} e^{2ik_f d}}{1 - R_{surf} R_{int} e^{2ik_f d}} e^{-2ik_0 d}, \quad (2.162)$$

$$R_{int} = \frac{k_f - k_s}{k_f + k_s}, \quad R_{surf} = \frac{k_f - k_0}{k_f + k_0}$$

where the dependence on ρ_f is implicit in k_f . At large $q = 2k_0$, one has:

$$|R|^2 \simeq \frac{\pi^2}{k_0^4} \left[\rho_f^2 + (\rho_s - \rho_f)^2 + 2\rho_f(\rho_s - \rho_f) \cos(2k_0 d) \right] \quad (2.163)$$

which is an oscillating function of period π/d whose envelope follows the q^{-4} decay. From the period of oscillation at large k_0 , one can determine the thickness of the film via the relation:

$$d \simeq \frac{\pi}{\Delta k_0} \quad (2.164)$$

where Δk_0 is the distance between two maxima of the oscillations.

Another parameter affecting the reflectivity is the film's SLD ρ_f . More precisely, the quantity responsible for changes is difference in SLD between film and substrate.

In the case of ultra-thin Co film on Ir substrates, $\rho_f < \rho_s$ and the Co reflectivity is less than the Ir Fresnel reflectivity. Hence the latter becomes the upper envelope of the former [42]⁷, as presented in Fig.2.22a.

Accounting for absorption effects, *i.e.* allowing the SLD to be a complex quantity, a reduction of the reflectivity, the rounding of the critical edge and the attenuation of the oscillations is expected for small k_0 (see Fig.2.22b).

Also the roughness of the interface has an effect on the reflectivity curve. To analyze such effects, consider a linear profile for the roughness. We can model it as presented in Fig.2.23: the layer is extending over a range long $2d$ in which, at 0 the film starts to be uniform, whereas at $-2d$ there is the uniform vacuum.

⁷Effects like rounding of the edge step are expected only for films of thickness above 100Å.

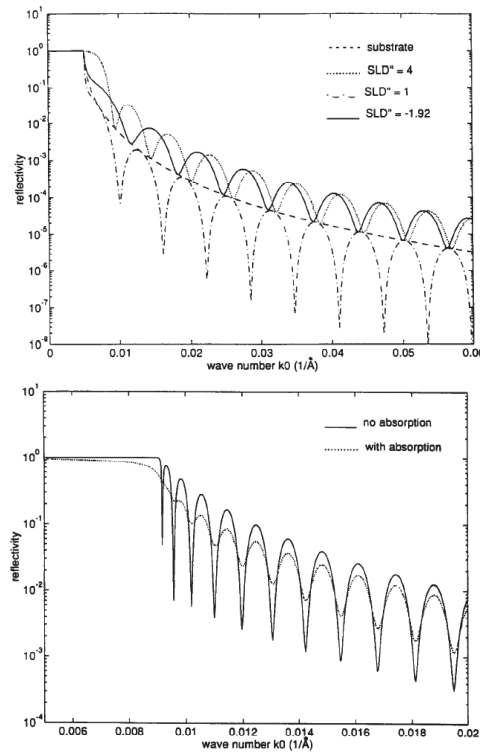


Figure 2.22: **Left:** Effects of different SLD on the XRR profile. **Right:** Effects of the absorption on the XRR profile: the total reflection is decreased and the transition to the q^{-4} decrease region is smoother and rounded. The oscillations are also damped.

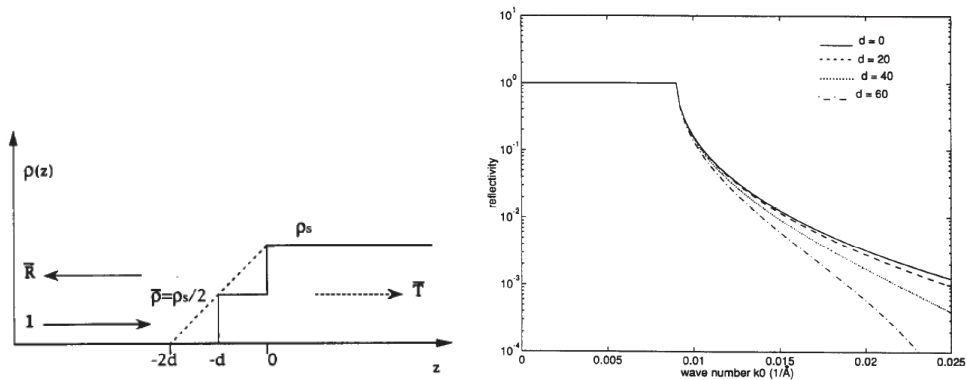


Figure 2.23: Roughness effects on the XRR profile. **Left:** the roughness is considered as a linear function of the height whose steepness depends on the length of the region $[0, 2d]$. **Right:** The effects of increasing d , or of increasing steepness in the roughness profile are shown for low k_0 values.

In the range $[-2d, 0]$, the SLD changes linearly and its average value is

$\rho_f/2$. The effects of the roughness at the interface can be seen as the steepness of the varying ρ or, equivalently as a function of the $2d$ range. One finds that as d increases, and the system gets further from the abrupt case, the reflectivity decreases. A quantitative, more detailed treatment of the roughness dependence can be found in [43].

The discussion presented so far provides the basis for a qualitative interpretation of XRR profiles. In particular, the dependence on structural parameters such as SLD, thickness and roughness have been presented as they are part of the system of interest.

In general, one can study a system being much more complicated and still the theory reported here would be quite useful. In facts, it is always possible to divide the system into thin layers, each having uniform $\rho(z)$. The interaction between the X-rays and each layer can be represented by matrices and the total effect can be calculated multiplying these matrices. As described in [44], this multiplication provides the reflectivity profile for the system.

However, the inversion of the XRR profile is not possible and approximate methods are used. Hence the simplifications made so far result to be useful. Such approximations are used in the quantitative analysis of XRR profiles: programs like ROD [31] and GenX [32] have been used to this purpose.

2.2 Visible light and anisotropic effects

The investigation of the structural properties at the atomic scale requires the use of X-rays. However, when it comes to study the magnetic response of a ferromagnet, visible light may become quite useful. In fact, since 1845 it is known that visible polarized light can undergo magneto-optic effects. In particular, when visible light reaches the polished surface of a ferromagnet, its polarization can be rotated upon transmission in the so-called Faraday effect [45]. In 1877, the same effect was found for reflected light and the phenomenon was named after its discoverer John Kerr [46].

Such effects, firstly naively described according to quantum theory in 1932 [47], were accurately explained in 1954 by Argyres [48]. In his work, perturbation theory was used to account for the spin-orbit interaction in anisotropic crystals. The resulting picture has different propagation velocities for left and right circularly polarized light. The superposition of these two modes then yields linearly polarized light whose change in direction is nothing but the manifestation of magneto-optic effects.

If one wishes to describe the optical properties of an anisotropic medium, the usual dielectric function must be replaced by dielectric tensor ε_{ij} . This tensor enters in Maxwell's equation as:

$$\begin{aligned}\nabla \cdot \mathbf{B} &= 0 \\ \nabla \times \mathbf{E} + \frac{d\mathbf{B}}{dt} &= 0 \\ \nabla \cdot \mathbf{D} = \varepsilon_0 \varepsilon_{ij} \cdot \mathbf{E} &= \rho \\ \nabla \times \mathbf{H} - \frac{d\mathbf{D}}{dt} &= \mathbf{j}\end{aligned}\tag{2.165}$$

with \mathbf{D} electric displacement field, \mathbf{E} electric field, $\mathbf{H} = \mu^{-1}\mathbf{B}$ magnetic field and ε_0 vacuum dielectric permeability. The tensor ε_{ij} can be decomposed in a symmetric and an antisymmetric part. Thanks to the Onsager relations, it is known that $\varepsilon_{i,j}(-\mathbf{M}) = \varepsilon_{i,j}(\mathbf{M})$ [49]. Furthermore, assuming cubic symmetry, the dielectric tensor can be written as:

$$\varepsilon = n^2 \begin{pmatrix} 1 & iQ_z & -iQ_y \\ -iQ_z & 1 & iQ_x \\ iQ_y & -iQ_x & 1 \end{pmatrix}\tag{2.166}$$

where n is the unmagnetized index of refraction and $\mathbf{Q} = (Q_x, Q_y, Q_z)$ is the Voigt vector. This vector is defined as $\mathbf{Q} = Q \cdot \mathbf{m}$ with \mathbf{m} being the magnetization and Q the Voigt constant, related to the frequency of the electromagnetic but independent from the temperature. Using the definition of \mathbf{Q} , Eq.(2.166) becomes:

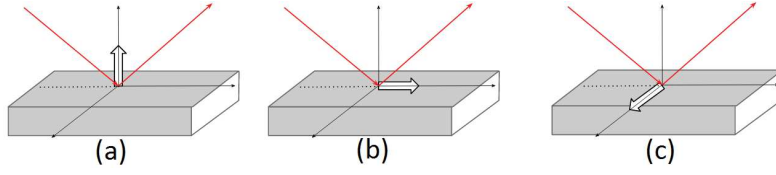


Figure 2.24: The image shows the three possible Kerr geometries: (a) Polar MOKE, (b) Longitudinal MOKE, (c) Transverse MOKE.

$$\varepsilon = n^2 \begin{pmatrix} 1 & iQm_z & -iQm_y \\ -iQm_z & 1 & iQm_x \\ iQm_y & -iQm_x & 1 \end{pmatrix}. \quad (2.167)$$

showing explicitly the dependence from the magnetization. The magneto-optic effects arise from the antisymmetric, off-diagonal elements. It can be made evident solving the Maxwell's equations with the boundaries of no charges, nor currents:

$$\nabla^2 \mathbf{E} - \mu_0 \varepsilon_0 \varepsilon \frac{\partial^2 \mathbf{E}}{\partial t^2} = 0 \quad (2.168)$$

From this, one gets as solutions the plane waves $\mathbf{E}(\mathbf{r}, t) = \mathbf{E}_0 e^{\pm i(\mathbf{k} \cdot \mathbf{r} - \omega t)}$ whose eigenvalues are the refractive indexes $n_{\pm} = n(1 \pm \frac{1}{2}Qmk)$. The \pm refers to left and right circularly polarized light $\varepsilon_L = \varepsilon(1 - \mathbf{Q} \cdot \mathbf{k})$ and $\varepsilon_R = \varepsilon(1 + \mathbf{Q} \cdot \mathbf{k})$. The different speeds of propagation are easily found from $v_{\pm} = c/n_{\pm}$ and it is clear they are directly linked to the off-diagonal elements of the dielectric tensor. Upon reflection, one component is retarded with respect to the other, from this delay the sup Linear polarized light can be seen as a combination of L and R circularly polarized light. Therefore a delay between these two components results into a different superposition which can result into a rotation of the polarization, *i.e.* the Kerr effect. The amount of rotation is measured by the Kerr rotation, or by the Kerr angle θ_k .

According to the direction of magnetization with respect to the plane of incidence and the plane of the surface, one can have three geometries for the Kerr effect:

- **Polar configuration:** when the magnetization \mathbf{M} is perpendicular to the surface;
- **Longitudinal configuration:** when \mathbf{M} is in the plane of the surface and parallel to the incidence plane;
- **Transverse configuration:** where \mathbf{M} lies in the plane of the surface and it is normal to the plane of incidence.

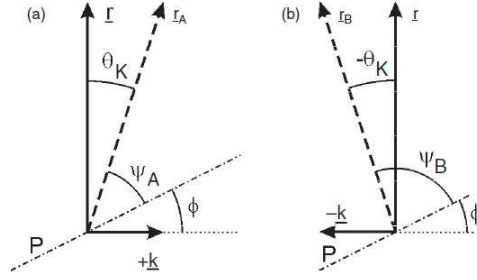


Figure 2.25: Image from D.A. Allwood *et al.*, *Magneto-optical Kerr effect analysis of magnetic nanostructures*. Schematic diagrams of polarized light amplitude vectors reflected from sample with opposite magnetization directions. \mathbf{r} is the magnetization independent reflection, \mathbf{k} is the Kerr reflection, \mathbf{r}_A and \mathbf{r}_B are the total amplitude reflections and make angles ϑ_K and ϑ_{-K} with \mathbf{r} , respectively. Angles Ψ_A and Ψ_B are formed between $\mathbf{r}_{A,B}$ and the direction of the analyzer.

For a better understanding, the three different geometries are shown in fig.2.24. The first two geometries yield an orthogonally polarized component upon reflection and allow to measure the in-plane and perpendicular magnetic anisotropy of the sample, respectively⁸. Since the aim of this work was to study the magnetic response around the critical thickness, these two configurations were chosen for the measurements.

The effects observed in longitudinal and polar MOKE are linear in \mathbf{Q} and yield a complex rotation ϕ of the polarization of the light. In order to describe it clearly, consider the reflection shown in Fig.2.25: the two drawings show the the two anti-parallel directions that give maximum MOKE signal. \mathbf{r} represents the magnetization-independent component of the reflected beam, while \mathbf{k} is the orthogonally polarized Kerr vector. \mathbf{k} depends on the magnetic properties of the medium and switches sign upon magnetization reversal. The total amplitude of the reflected vector \mathbf{r}_A (\mathbf{r}_B) is provided by adding vectorially \mathbf{r} to \mathbf{k} ($-\mathbf{k}$). The Kerr angle ϑ_K (ϑ_{-K}) is formed between \mathbf{r} and r_A (r_B). The angle made by the direction of \mathbf{k} and the polarization axis of the analyzer is called Φ .

In order to gain a quantitative insight of the effect, one can evaluate the transmitted optical amplitude with a given polarization. Neglecting absorption, it is:

$$\begin{aligned} t_A &= r_A \cos(90 - \Phi - \vartheta_K) = r_A \sin(\Phi + \vartheta_K) \\ t_B &= r_B \sin(\Phi - \vartheta_K) \end{aligned} \quad (2.169)$$

and the intensity of the beam component along P writes:

⁸The transverse Kerr effect, of minor importance to this work, causes variations of the amplitude of the reflected beam and is generally used to study the in-plane magnetic anisotropy

$$\begin{aligned} I_A &= I_0 \sin^2(\Phi + \vartheta_K) \\ I_B &= I_0 \sin^2(\Phi - \vartheta_K) \end{aligned} \quad (2.170)$$

where $I_0 \propto r_A^2 = r_B^2$ is the total optical intensity of the reflected beam. Assuming small ϑ_K , from the average intensity of the A and B cases:

$$\bar{I} = \frac{I_0}{2} (1 - \cos 2\Phi \cos 2\vartheta_K) \approx I_0 \sin^2 \Phi \quad (2.171)$$

and from the difference between I_A and I_B :

$$\Delta I = I_0 \sin(2\Phi) \sin(2\vartheta_K) \quad (2.172)$$

one can calculate the *fractional MOKE signal*:

$$\frac{\Delta I}{\bar{I}} = \frac{2 \sin(2\Phi) \sin(2\vartheta_K)}{1 - \cos(2\Phi) \cos(2\vartheta_K)}. \quad (2.173)$$

Typically ϑ_K is of the order of few *mrad*, hence the latter equation can be written as:

$$\frac{\Delta I}{\bar{I}} \approx \frac{2 \sin(2\Phi) 2\vartheta_K}{1 - \cos(2\Phi)} \approx \frac{4\vartheta_K}{\tan \Phi}. \quad (2.174)$$

In the experimental practice, one can "select" a particular polarization direction with the use of polarisers. Such devices allow only a given polarization direction to be transmitted: all the other polarizations are extinguished. The quality of a polariser is defined on the basis of its extinction ratio: currently, polarisers have this value around 10^{-7} . Taking into account this deviation from the ideality, a non-zero minimum transmitted intensity (I_{min}) could be measured even if there is no such polarization in the reflected beam. The biggest artefacts originating from such effect are found at low transmitted intensities. To correct for them, it is necessary to introduce a constant depolarization factor: $\gamma_D = I_{min}/I_0$. Eq.(2.174) becomes then:

$$\frac{\Delta I}{\bar{I}} \approx \frac{2\vartheta_K \sin(2\Phi)}{\sin^2 \Phi + \gamma_D}. \quad (2.175)$$

The factor $\Delta I/\bar{I}$ we have just calculated, represents the signal dynamic range. It is proportional to ϑ_K which, in turn, depends on the magnetization. The depolarization factor γ_D is most significant at low transmitted intensities, then one could choose to measure only big intensity signals and avoid to consider γ_D . Nevertheless, this strategy would reduce the signal dynamic range and the signal to noise ratio (proportional to ΔI) would decrease too.

In the following chapter, the experimental setup of MOKE will be presented and some practical issues will be discussed.

Methodology

3.1 Laboratory Techniques

Synchrotron radiation is an incredibly precious and versatile tool to investigate matter. In order to preserve these characteristics, the X-ray beam produced in synchrotron has strict requirements to fulfil (intensity, collimation, stability, etc...). The achievement of a good quality beam is possible and is routinely available at the ESRF, where the beam and its countless potentialities, are used by a growing scientific community.

Users can perform experiments at the ESRF, provided that their scientific quest had passed a selection protocol ensuring the high quality of science produced at the facility. In order to succeed in the selection, one has to prove a deep knowledge of the system to be studied, stating clearly the purpose of the experiment and the expectations about the measurements. All the above makes a preliminary and detailed analysis mandatory.

In order to ensure a proficuous use of the beam time and to ell define the system under study, preliminary investigations were carried out using the UHV chamber available at the ID03 beamline support laboratory. The chamber has a base pressure of 10^{-10} mbar and it is made up of three small chambers: a loading chamber, to load the sample from ambient pressure, a main chamber, where all the investigations are carried out and which is constantly under UHV conditions, and a transfer chamber, which is in between the loading and the main chamber. The transfer chamber is used to minimize chemical contamination and pressure variations in the main chamber.

During experiments, the sample is fixed on a sample holder. The sample holder is mounted on a manipulator which can be moved on three linear axis with millimetric precision and rotated along the direction of the sample surface. The sample is constantly in contact with a Boralectric[®] heating system, allowing to perform sample annealing.

The chamber is equipped with:

- an **ion gun** to perform Ar^+ sputtering,
- electron beam **evaporators** and a **quartz balance** to allow a fine control on the film growth,

- a **gas** line to inject controlled amounts of gases in the chamber (e.g. for CVD growth)

ensuring the reproducibility of the sample characteristics, and with:

- **XPS** and **LEED** equipment to check the crystalline and chemical quality of the sample (see below for more details),
- **electromagnets** to carry out **MOKE** measurements.

which can provide a fine analysis.

In the following, the procedures used for Co film and graphene growth are presented and, later on, the theoretical basis of the experimental apparatus are discussed.

3.1.1 Thin films growth

A critical issue when dealing with thin films is represented by a fine control of the film's thickness. Since the t_c defining the limit for PMA is of few ML, the thickness control must ensure a film growth within these limits. To fulfil this requirement, the thin Co films studied in this thesis were grown by *e⁻ beam evaporation*. This technique is based on Co sublimation: the atom generated from a solid Co rod travel in vacuum until they reach the sample surface forming the film.

In this work, an Omicron EFM3 directly mounted onto the Omicron UHV chamber was used. The UHV compatibility allows one to study pristine films *in-situ*.

A scheme of this evaporator is outlined in Fig.3.1 and 3.2. By tuning the current running into the "filament", electrons are emitted by thermoionic effect. Using a positive high voltage (typically around 1 KV), electrons are accelerated towards the "evaporant" (the Co rod) spot-welded to a Mo support (see fig.3.2).

The bombarding electron beam induces a temperature rise of the rod resulting into Co sublimation. Co atoms evaporate from the solid rod and, in the gaseous state, flow towards the sample at a given rate.

Due to electron impact, some of the atoms may be ionised and give rise to an ion current. The beam exit column contains an ion collector which serves as a flux monitor measuring the ion current. The ion current is proportional to the evaporation rate and to the emission current I_{em} summing up the flux of electrons and ions. The references given by the flux monitor and the emission current are used to set the evaporation rate for a given HV.

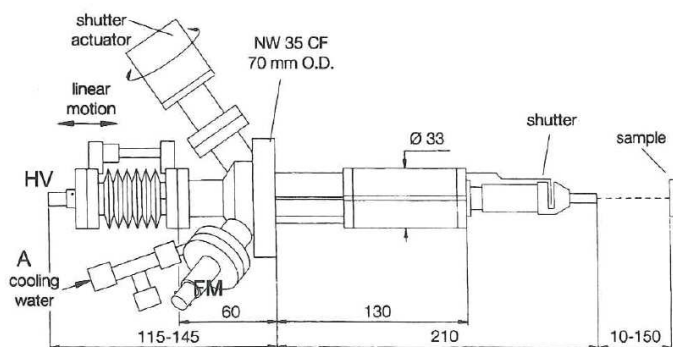


Figure 3.1: Outline of the Omicron EFM3 evaporator as presented by its manual. HV: High Voltage feedthrough, also holding the evaporant (in this case, the Co rod). FM: BNC socket for Flux Monitor. Distances are in mm.

The shutter placed at the evaporator outlet can be open and closed by a rotary drive: this feature allows a precise flux adjustment prior to exposure and a fine control of the evaporation time.

In order to avoid the evaporator heating, only restricted region of the evaporant is heated, that is the area next to the filament. In addition, a water-cooled copper cylinder called “cooling shroud” surrounds the the evaporation (Fig.3.2). These precautions minimize the desorption of any contaminants present on the evaporator’s internal walls and, therefore, avoid the surface contamination.

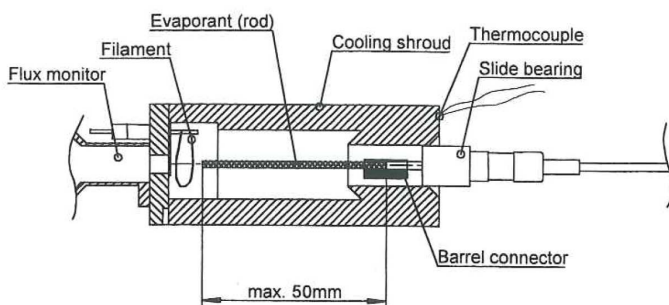


Figure 3.2: Drawing of the cooling shroud in which a rod has been mounted using a barrel connector. In our work, the Co rod was spot welded to the mounting post which replaced the barrel connector mounting.

The control on the evaporation parameters result into the achievement of a fine and stable control of the evaporation rate.

3.1.2 Graphene capping layer

Graphene is chemically inert and it represents a perfect candidate as a capping layer for the highly oxidisable Co film. The growth procedure used in this work is called Chemical Vapour Deposition (CVD). CVD is a fast and straightforward way of growing monolayer Graphene on a metallic substrate. It requires to let some gas containing Carbon atoms flow inside the UHV chamber. There, thanks to the joint action of a metallic catalyst (substrate)

and high temperatures, C atoms dissociate from the gas molecules and bind to one another, forming the Gr layer.

In our case, the Iridium substrate was brought at $T_{gr} = 600$ °C . Once the temperature was stable, some Ethylene C_2H_4 was let flow into the UHV chamber through a leak valve so that a partial pressure of 10^{-5} mbar was reached. Temperature and pressure conditions were kept stable for 40 min. Finally, the Ethylene was pumped out of the chamber and, later on, the temperature was slowly brought back to room temperature.

The choice of T_{gr} determines the final Graphene quality. The value of T_{gr} used in this work is far lower than the value commonly used to produce Graphene. This results into a defective Gr which allows the intercalation to occur at lower temperatures. This minimizes the risk of phase transitions or morphology alterations (dewetting, diffusion, intermixing).

Due to the high temperatures, the CVD growth is not safe for Gr growth directly on the Co film: in facts, $T_{gr} = 600$ °C can result into the Co film integrity loss, thus destroying its magnetic response. For this reason, the capping procedure exploits the intercalation: a thermal process occurring at way lower temperatures. The intercalation is the insertion of a material (thin film, nanoparticles etc) in between two layers. Co intercalation between a defective Gr (grown at $T_{gr} = 600$ °C) and Ir occurs at $T_{int} \simeq 300$ °C [14, 21, 50].

Thermal Intercalation

The intercalation procedure is a thermally triggered process. Intercalation was used after the Co film deposition on the Gr/Ir systems and it was achieved by keeping the system at a temperature T_{int} for a period t_{int} .

T_{int} is linked to the Gr quality: better Gr qualities require higher temperatures for the Co to be intercalated.

This follows from the fact that Co atoms choose the defects in the Gr layer as preferential site for intercalation [15]. Therefore, higher amounts of defects (or lower quality) in the Gr layer require less thermal energy to make Co atoms reach the Ir substrate. The possibility of intercalating at lower T allows one to avoid any thermal modifications to the film, thus minimizing the risk of dewetting, desorption, diffusion and so on. On the other hand, one cannot use a highly defective Gr, as too many defects would make the capping layer fail in preventing Co oxidation.

Basically one has to balance the amount of defects in order to have the right amount of defects so that the intercalation is achieved at relatively mild temperature and the Gr coverage is enough to provide chemical stability.

In this work $T_{int} = 300$ °C, and $t_{int} = 5$ min, following the procedure reported in [14] where also a magnetic characterization of the first intercalated films is available.

In order to check the Ir(111), Co, and Graphene surfaces Low Energy Electron Diffraction (LEED) and Xray Photoemission Spectroscopy (XPS) were employed.

3.1.3 XPS

The X-Ray Photoemission Spectroscopy is a complex technique providing finest details about the electronic nature of ions, molecules and surfaces. In this work, it was used as a relatively simple tool to check the cleanliness of the sample surface, to evaluate the thickness of the Co film deposited onto the Ir surface, and to probe the Co distribution along the sample depth.

XPS is based on the photoelectric effect. After shining monochromatic X-rays of energy $h\nu$ on the sample, photoelectrons from the core levels are analysed as a function of their kinetic energy E_k . Thanks to the Einstein's relation of photoelectric effect:

$$E_{kin} = h\nu - E_b - \phi \quad (3.1)$$

the binding energies E_b of such photoelectrons can be retrieved if the work function is known. Moreover, being core levels highly specific for each atom, they act as elements fingerprints and the chemical composition of thin films and surfaces can be obtained looking at the relative intensities of XPS lines.

An idealized scheme of the photoemission process is shown in Fig. 3.3. The electronic levels of the specimen are drawn on the left side of the drawing, whereas on the right side there is the analyser, its electronic levels and work function. The energetic reference between the two is the Fermi level.

If we assume the photoelectric effect to occur from the k^{th} level, the kinetic energy E_0k gained by the electron relatively to the sample, will be different from that measured by the spectrometer E_{kin} . This difference is due to the mismatch between the work functions of the sample ϕ_S and of the spectrometer ϕ_{spect} . The dependence of E_{kin} on ϕ_s is expressed through:

$$E_b^F(k) = h\nu - E'_{kin} - \phi_S E'_{kin} = E_{kin} + (\phi_{spect} - \phi_S) \rightarrow E_b^F(k) = h\nu - E_{kin} - \phi_{spect} \quad (3.2)$$

Therefore, the knowledge of the sample workfunction is not required to convert the kinetic energy to binding energy.

Experimentally, the measurements are carried out using an X-ray source, an electron energy analyser and some form of detection and control system.

Laboratory X-Ray sources consist of a heated-filament cathode from which electrons are emitted by thermoionic effect. Using high voltages ($\simeq 15$ KV), electrons are then accelerated toward a solid anode typically in Al or Mg (in our case, Al). The impact creates holes in the Al 1s orbitals. Such holes are filled through the fluorescence decay channel producing X-rays. Such radiation, called Al K_α , is produced by the dominant transition $2s \rightarrow 1s$ and has

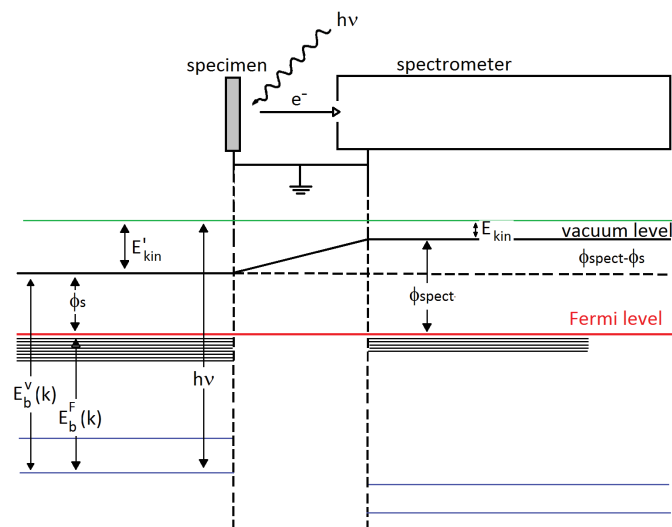


Figure 3.3: A scheme of the photoemission for a metallic sample taken from C.S. Fadley, *Basic Concepts of Photoemission Spectroscopy* [51]. The X-ray gives its energy to an atom of the sample, the latter emits an electron which reaches the spectrometer and is detected. The kinetic energy of the electron depends on the binding energy it had before the emission and on the energy of the radiation: $E_{kin} = h\nu - E_b^V(k)$. The kinetic energy measured by the analyzer is affected by the difference in the work functions of the sample and the analyzer itself. To obtain the binding energy of the electron one has to calculate $E_b^F(k) = h\nu - E_{kin} - \phi_{spect}$ so the specimen work function is not needed.

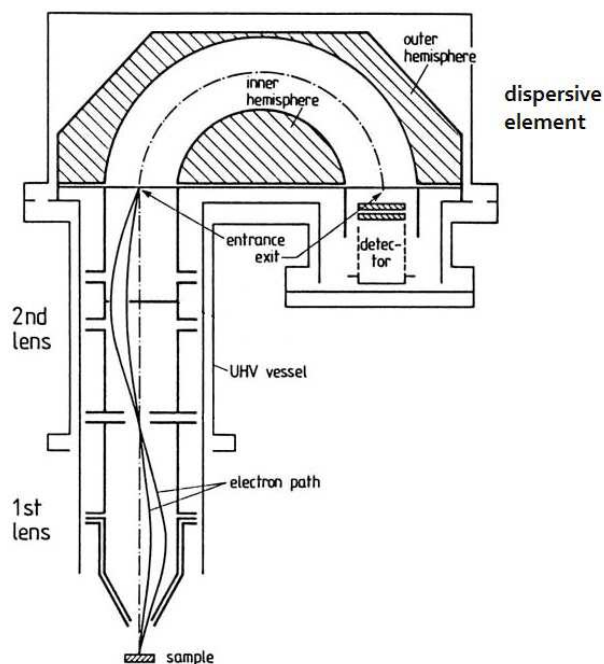


Figure 3.4: Scheme of the XPS electron analyzer from [27]. After being emitted from the surface, electrons that reach the analyser travel inside magnetic lenses that guide them to the aperture of the dispersive element. The electrons that possess the right energy (the *Pass Energy*) exit the hemispheric condenser and enter the detector.

an energy of $h\nu = 1486.7 \pm 1.4$ eV. The interaction with the specimen generates the photoelectric effect and photoelectrons are emitted in every direction. Photoelectrons emitted towards the analyser are detected and contribute to the final spectrum. A schematic illustration of the electrons path inside the analyser is shown in 3.4.

Inside the analyser, electrons travel inside a series of magnetic focussing lenses guiding them to the entrance of the dispersive element. It is a hemispherical capacitor acting like a band-pass filter selecting the particles on the basis of their kinetic energy. Electrons with energy different from a preset value (called pass energy) cannot get outside the dispersive element and do not reach the following step: the channeltron. The channeltron amplifies the electric signal. It is made of a low work function material, and when an electron impacts on it, several other electrons can be emitted through a secondary emission in a cascade effect. The channeltron is shell shaped to enhance the probabilities that the electrons (both the primary electrons and the ones emitted by the channeltron itself) hit the walls, while current flowing backward

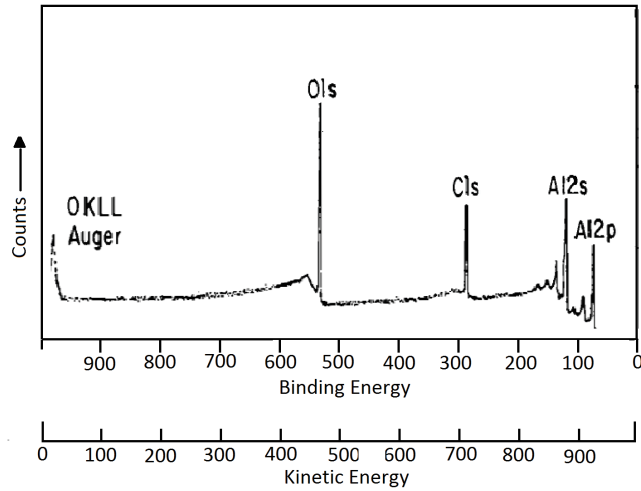


Figure 3.5: An example of an XPS spectrum of an oxidized aluminium sample with a carbonaceous contaminant overlayer taken from C.S. Fadley, *Basic Concepts of Photoemission Spectroscopy* [51]. Aluminium, Carbon and Oxygen peaks are labelled.

are prevented by a positive potential applied to the end. The total potential applied to the channeltron determines the amplification. The current pulse produced by the channeltron is converted into a voltage pulse by a preamplifier. Finally a counter counts the pulses that arrive in a certain time interval (usually of the order of few seconds) and gives an output proportional to the number of photoelectrons selected by the dispersive element. The information collected for several pass energies in a given range is used to draw the spectrum. Usually every point in the spectrum has an integration time of 1 or 2 seconds and energy scans have $0.3 \div 0.5$ eV step.

The energy range to probe is chosen with respect to the element that one wants to inspect: in principle, any energy range from 0 eV to $h\nu - \phi_{spect} = 1467$ eV can be selected. Since the core binding energies are known for each element, one adjusts the energy range in order to probe specific peaks for a given element. In this thesis, XPS chemical sensitivity was used to inspect a broad range of energies. In this way, we could make sure that the initial crystal was not contaminated by other elements before starting the experiment. After the Co growth, the range chosen were $E_{kin} = 1356 \div 1431$ eV for Ir_{4f} and $625 \div 725$ eV for Co_{2p} .

Typically, XPS spectra show the distribution of the number of photoelectrons as a function of their kinetic or binding energy. An example of a XPS spectrum is shown in Fig.3.5 where the counts are reported as a function of the kinetic energy and of the binding energy. The spectrum shows several peaks and continuum regions. The peaks are found at energies associated with specific core levels and their intensity is proportional to the amount of a given

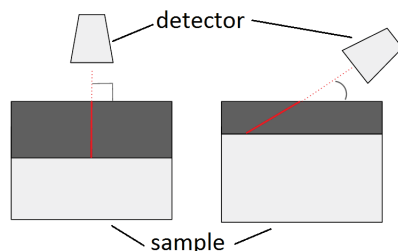


Figure 3.6: The drawing is a scheme of the experimental setup involving the sample and the detector. The solid line is the mean free path of electrons in the sample, the dotted line represents the path travelled by the photoelectrons from the sample to the detector, the shadowed part of the sample is the maximum depth probed by the XPS. On the left a right angle detection is depicted, the right side shows how a smaller angle can give a higher surface sensitivity.

element in the sample. In the case of thin films, the measurement of intensity for peaks coming from both the substrate and the film, lead to the estimation of the film thickness d [51]. For the Co on Ir case, the formula reads:

$$d = \lambda \sin \theta \ln \left(\frac{I_{Co} \rho_{Ir} \sigma_{Ir}}{I_{Ir} \rho_{Co} \sigma_{Co}} + 1 \right) \quad (3.3)$$

where λ is the average inelastic mean free path of electrons, θ is the exit angle, I_x is the peak intensity of element x , while ρ and σ are the element specific atomic density and photoelectric cross section.

Another feature observable in the XPS spectra is the decreasing continuum next to each peak resulting into a slightly asymmetric lineshape of the peak itself. This effect is given by photoelectrons that lost part of their energy because of inelastic scattering on their way out of the sample. In facts, X-rays penetrate inside materials up to a few μm deep: hence photoemission occurs far away from the surface. Nevertheless, electrons emitted from deep regions, undergo so many inelastic scattering events that they lose most of their kinetic energy before leaving the sample surface. Their contribution to the spectrum can be found in the continuum regions and represents an important source of information [52, 53, 54]. However, the study of this region requires complex and time-consuming algorithms which were not used in this work.

Despite the deep penetration in the materials, XPS surface sensitivity is limited by the short mean free path of core electrons inside solids (discussed in the previous chapter). Moreover, surface sensitivity can be tuned varying the angle of detection of photoelectrons. In particular, the use of grazing angles helps in keeping the electrons path within the topmost layers, as show in Fig.3.6.

The data collection at different angles is basis of Angle Resolved XPS (AR-XPS). When more than one chemical specie is present on the sample, varying

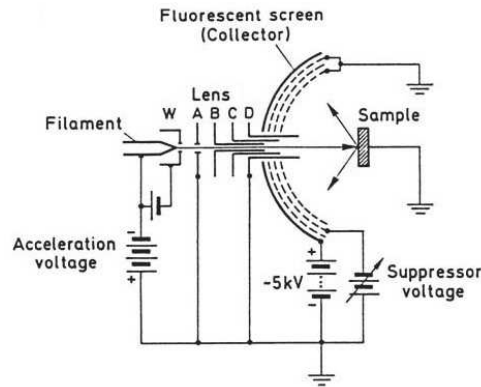


Figure 3.7: A scheme of a standard LEED setup taken from H. Luth, *Solid Surfaces, Interfaces and Thin Films* (Springer 2010). The heated filament emits electrons, these electrons pass through a Wehnelt cylinder W and a magnetic lens. Eventually they reach the sample and experience backscattering. After the scattering, inelastically scattered electrons are filtered by the grids whereas electrons that underwent elastic scattering reach the phosphor screen and give rise to fluorescence.

the angle gives information on the distribution of the each element along the direction perpendicular to the surface. In facts, the intensity of a given peak of an element lying in the topmost layers, will be enhanced by smaller angles. In the case of thin films, a linear decrease of the intensity ratio $I_{film}/I_{substrate}$ would be the evidence of the film homogeneity.

3.1.4 LEED

The Low Energy Electron Diffraction (LEED) is a technique providing a view of the reciprocal space of the sample surface. In particular, it offers an instantaneous two-dimensional projection of a spherical section of the reciprocal space that can be used to obtain real space information **ref**. The information obtainable by LEED experiments concerns the crystallographic symmetry and the surface quality within the first few atomic layers. A beam of low-energy electrons is produced by an electron gun and focused on a sample. The electron diffraction patterns are typically observed on a hemispherical fluorescent screen, centred on the specimen and observed through a glass window of the vacuum chamber. A scheme of the experimental apparatus is shown in 3.7.

The electron gun unit consists of a heated filament with a Wehnelt cylinder W followed by an electrostatic lens with apertures A, B, C and D. The acceleration energy is determined by the potential between the cathode and the apertures A and D. B and C have a potential intermediate between A and D and are used to focus the electron beam. D is kept at the same (earth) potential as the sample to allow the electrons to fly without acceleration towards the sample surface [27]. The interaction with the crystal causes the electrons

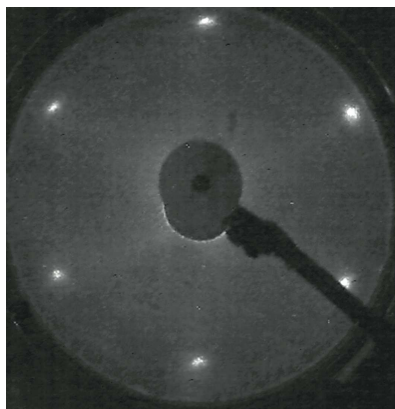


Figure 3.8: An experimental LEED pattern of an Ir(111) single crystal.

to be scattered from the surface. After scattering the electrons impact on a phosphor screen that converts the electron signal into a visible light through fluorescence. Digital images are recorded using a high resolution camera and analysed (see below) to extract crystallographic information. The electron scattering from sample surface atoms can be elastic or inelastic. Elastic interactions result in no energy losses, whereas inelastic scattering causes larger detection angles and kinetic energy losses. Elastically scattered electrons give rise to interference as shown in Fig.3.8.

A peak of interference is observed on the screen every time the Bragg's condition is satisfied. Therefore, inverting the Bragg's law, one can retrieve the crystal lattice parameter.

Electrons that undergo inelastic scattering have different wavelengths and are incoherent: they do not interfere and produce diffraction peaks. On the contrary, they give rise to a smooth, uniform background illumination of the phosphor screen bringing contrast loss in the final image. To reduce this background, four grids are interposed between the sample and the fluorescent screen where the diffraction is made visible. The background illumination is suppressed by giving the middle grid (called suppressor grid) an opportune negative bias preventing most of the low energy, inelastically scattered electrons to reach the phosphor screen. The grid and the lens aperture that lay closest to the sample and the sample itself are grounded to avoid electrons accelerations on the way to the sample and back. The fluorescent screen (or collector) has to be biased positively (5kV) in order to achieve a final acceleration of the slow electrons; only high-energy electrons can be made visible on the screen [27].

In Fig.3.8, a LEED pattern is reported. It was obtained from an Ir(111) sample using 100eV electrons. The spots are visible in position associated with reciprocal lattice points: the hexagonal symmetry of the lattice can be seen by eye.

Typical LEED energies ($20 \div 500$ eV) are low enough to give a De Broglie wavelength $\lambda = h/p$ comparable to the interatomic distances. In fact, in this energy range, the mean free path of electrons is the minimum achievable (see Fig.2.8)). Furthermore, the short mean free paths indicate a strong interaction with matter, therefore a small penetration and a good surface sensitivity is achieved.

The energy of the primary electron beam is also linked to the number of spots visible in each pattern. The higher the energy, the higher the number of spots visible. This is due to the fact that the Ewald sphere becomes bigger at higher energies and more reciprocal-lattice points lie on its surface giving rise to more Bragg peaks. Anyway, once the image is collected and stored, the analysis of the spot positions can be made and yield information on the size, symmetry and rotational alignment of the sample.

3.1.5 MOKE

The MOKE technique is based on the Kerr effect discussed in the previous chapter. Despite the Kerr effect was discovered by John Kerr in 1877 [46], its application to thin samples only began in 1985 [55]. This technique allows to measure the magnetization of ferromagnetic systems such as nanoparticles, films and multilayer. Since the penetration depth of the probing light can be of several μm , in the case of thin films, the probed magnetization is the one of the whole film. This means that MOKE surface sensitivity is limited by the film thickness itself and can go down even to one ML. As far as the lateral resolution is concerned, MOKE provides spatially integrated information about magnetic properties of the system: the area over which the integration is taken is determined by the light spot [56].

From the experimental point of view, the MOKE setup is rather simple. It consists of a laser, two polarisers, a photodiode and a lock-in amplifier, as illustrated schematically in Fig.3.9.

While the external magnetic field is produced by computer-controlled electromagnets, oriented parallel and perpendicular to the film plane, the linearly polarised laser beam ($\lambda = 670$ nm) is produced by a solid state diode with an output power of 5 mW. The laser was fed with a sinusoidally varying intensity so that the lock-in could be used (see below). The first polariser defines the polarization direction of the incoming beam, while the second one, the *analyzer*, is used to measure the polarization direction of the reflected beam. (according to Fig.2.25, the analyser defines the P direction). The photodiode, placed behind the analyser, measures the intensity of the reflected beam through the computer-controlled lock-in amplifier.

This type of amplifier allows a signal with a known waveform to be extracted from a very noisy environment: this is of fundamental importance since some MOKE signals have low intensities. The lock-in exploits a reference signal (provided by an internal circuit) to compare it to the frequency

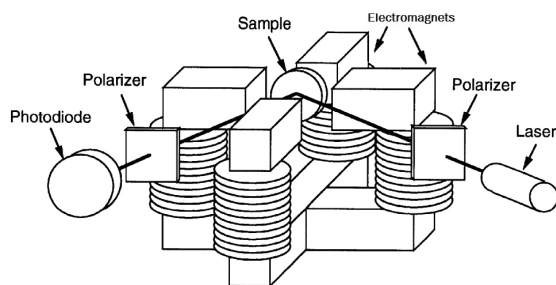


Figure 3.9: A scheme of the experimental setup for MOKE measurements. A polarized light is emitted by a laser and goes through a polarizer before reaching the sample. After reflecting upon the surface of the specimen, the light transmits through an analyzer and is finally detected by a photodiode. The signal is then amplified by a lock-in amplifier. The external applied magnetic field is produced by two electromagnets: one generates an in-plane magnetic field, the other one is responsible for the out-of-plane field. By measuring the magnetization for different magnetic fields, one can collect all the data needed to plot a magnetization curve.

of the input signal: a multiplier receives the two signals and gives an output which is non-zero only when the internal circuit frequency matches the frequency of the input. The noisy component of the output is then removed by a low-pass filter. The output of the lock-in amplifier is thus a DC voltage proportional to the amplitude of the input signal with the noise removed.

Since the sample is placed into a vacuum chamber and the laser is outside, a quarter-wave plate is usually used to correct for the birefringence of the chamber windows. However, in our work the quarter-wave was removed from the setup and we corrected the birefringence “by hand” simply varying a bit the polarization direction of the incident light. In this way, the few degrees of mismatch between incident and reflected light are taken into account.

The real, operational configuration is shown in Fig.3.10.

3.2 Synchrotron Radiation

Synchrotrons are extremely powerful light sources producing electromagnetic radiation in a broad spectral range. The synchrotron light is produced by forcing relativistic electrons to change direction of their motion under the effect of magnetic fields.

Figure 3.11 shows the main components of the European Synchrotron Radiation Facility (ESRF) located in Grenoble, France, where all the measurements described in this thesis were performed.

In this machine, everything starts with the production of electrons by a 100 keV triode gun. The electrons are packed in bunches by a short standing



Figure 3.10: The experimental apparatus used for MOKE measurements at ID03. The electromagnets are mounted on the flanges of the UHV chamber in which the sample is placed.

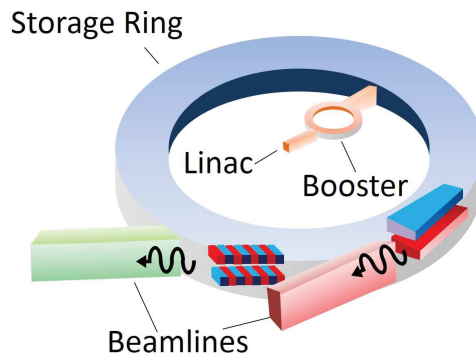


Figure 3.11: Scheme of a modern accelerator for synchrotron radiation production. Electrons are accelerated in the linac and injected in the booster, where they are further accelerated with the synchronous increase of the fields. When they reach 6 GeV, they are stored in the storage ring. Beamlines are built tangentially to the storage ring, so that they can use the X-rays produced from electrons upon bending.

wave buncher, accelerated by a “linac” (linear accelerator) to 200 MeV, and injected in a 300 m circular section called “booster”¹ where they reach 6 GeV. The bunches are then injected up to a current of 200 mA in the 844 m long storage ring where the pressure is in the 10^{-9} mbar range.

The beam energy is directly linked to its angular divergence $1/\gamma[\text{rad}]$ which is the inverse of the Lorentz factor $\gamma = E/m_e c^2 = 1957E[\text{GeV}]$. The angular divergence of the 6 GeV beam is then $\simeq 85\mu\text{rad}$ as shown in Fig.3.12.

The spread of the electrons in the phase space (represented in Fig.3.13) divided by π is the *emittance* ε . The smallest values achievable in the ESRF

¹Actually, this circular section alone is the real “synchrotron”, as this is where one has the synchronous increase of the fields in order to bring the electron bunches to high energies.

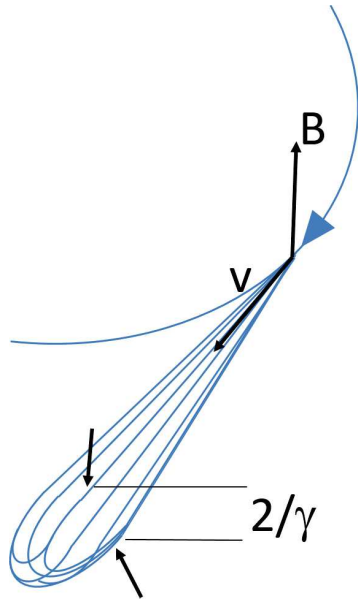


Figure 3.12: A relativistic particle on a circular orbit emits radiation in a narrow cone. The angular divergence $1/\gamma$ lies in the direction perpendicular to the orbit. If one considers the spread of the whole cone (both above and below the ideal trajectory), the angular spread is doubled.

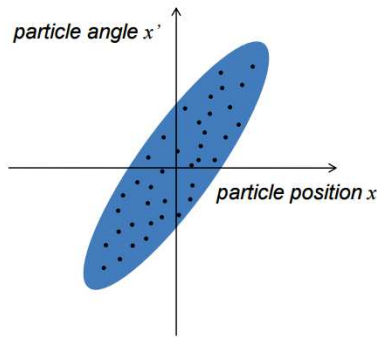


Figure 3.13: Scheme of the spread of an electrons bunch in position and momentum space.

storage ring are $\varepsilon_h = 1.5 \cdot 10^{-10}$ m-rad in the plane of the ring and $\varepsilon_v = 5.0 \cdot 10^{-12}$ m-rad in the perpendicular direction.

The radius of curvature of relativistic particles depends on the magnetic field B through $\rho = \gamma mc / (eB)$. This radius defines the critical wavelength λ_c , that is the maximum wavelength of the broad range produced by the machine. This wavelength is given by the relation:

$$\lambda_c = \frac{4\pi}{3} \frac{\rho}{\gamma^3} \tag{3.4}$$

The beam quality is usually determined in terms of flux, brightness and the brilliance. The flux of the photons for a given wavelength is defined as the number of photons emitted per second, in a spectral bandwidth $0.1\% BW$ into a 1 mrad orbital fan. In formulas, one has:

$$F = \frac{\textit{photons}}{\textit{sec} \cdot \textit{mrad} \cdot 0.1\% BW} \tag{3.5}$$

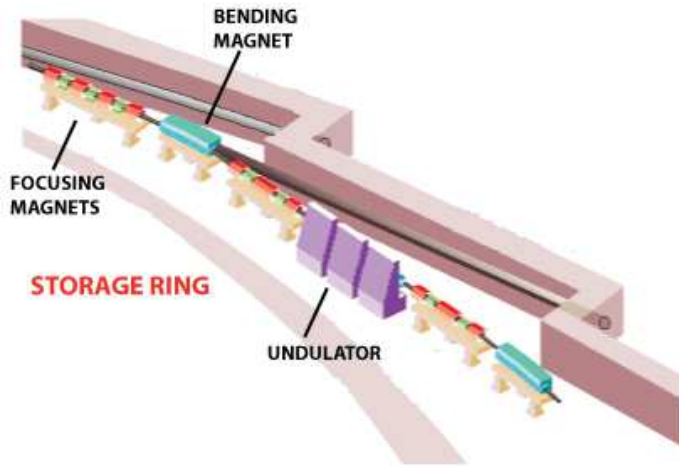


Figure 3.14: A portion of the storage ring at the ESRF showing its arrangement.

The flux per solid angle is called *brightness*. From the brightness, one defines the *brilliance* as the brightness divided by the *emittance* ε and by the average electron velocity, *i.e.*:

$$B = \frac{\text{photons}}{\text{sec} \cdot \text{mrad}^2 \cdot \text{mm}^2 \cdot 0.1\% \text{BW}}. \quad (3.6)$$

The electron beam in the ESRF storage ring travels through 32 straight and 32 curved sections in alternating order. The straight sections house undulators (shown in Fig.3.15) to produce an intense X-ray beam, whereas, in the curved sections, one finds bending magnets (BM). Passing through the bending magnets and the undulators, the electrons radiate photons and lose energy. After each BM or undulator, radio-frequency cavities are used to compensate the energy loss and restore the beam energy close to the nominal 6 GeV. Moreover, focusing magnets are employed for keeping the electrons close to their ideal orbital path. The arrangement of these elements is shown in Fig.3.14.

The beam delivered to a beamline depends strongly on the kind of device placed upstream to the beamline itself. The next two paragraphs aim to provide some details of how the undulators and bending magnets affect the beam.

Undulators are “insertion devices” made up of two arrays of small magnets producing alternating magnetic fields which force the electron beam onto a sinusoidal trajectory of N periods, each of length λ_u and with angular bending α .

The optical properties of undulators are characterized by the K parameter which links λ_u and the applied field B_0 :



Figure 3.15: The jaws of undulators are made up of small magnets producing alternating magnetic fields. The magnetic fields make the electron bunches move along wavy trajectories of period λ_u and angular deviation α . The magnetic field intensity can be adjusted by varying the gap between the jaws.

$$K = \frac{e}{2\pi mc} \lambda_u B_0. \quad (3.7)$$

Undulators have $\alpha < 1/\gamma$: therefore, the photons emitted from consecutive bends overlap and interfere constructively for wavelengths

$$\lambda_m = \frac{1}{m} \frac{\lambda_u}{2\gamma^2} \left(1 + \frac{K^2}{2} + \gamma^2 \theta^2 \right) = \frac{1}{m} \frac{13.056 \lambda_u}{E^2(\text{GeV})} \left(1 + \frac{K^2}{2} + \gamma^2 \theta^2 \right) \quad (3.8)$$

where θ is the angle between the direction of observation and the axis of the undulator. Beside the “fundamental wavelength” λ_1 , one has higher order “harmonics” given by λ_1/m . Their number and intensity increase with the wiggling angle α of the electron trajectory in the insertion device². On the axis $\theta = 0$, only odd harmonics are emitted.

The typical spectrum of an undulator is shown in Fig.3.16 for two different values of K . Small K values are obtained using a large gap between the “jaws” of the undulator and result into a smoother trajectory of the electrons. The emission is shifted to higher energies. On the contrary, closing the magnets arrays increase the value of B and K and the change of the electrons direction is more abrupt. This results into an emission shifted towards smaller energies.

Bending magnets , represented in Fig.3.18, are used to change the path of the electrons into a racetrack-shaped orbit. They emit radiation covering a wide and continuous spectrum from microwaves to X-rays and are characterized by the critical wavelength given by Eq.3.4. This value divides the spectrum in two regions of equal radiated power: 50% at wavelengths $\lambda < \lambda_c$ and 50% above.

The radiation emitted by one electron travelling on an arc of circumference is a discrete spectrum of closely spaced lines up to a cutoff frequency $\omega_{cutoff} \simeq \Delta\tau^{-1} = c\gamma^2/\rho$. On the other hand, in the storage ring, one has electron bunches in which electrons oscillate around the main orbit with a kinetic energy varying around an average value. These effects give rise to a

²The dependence of λ on α is what allows one to vary the energy of the emitted photons: in the undulators it is related to the gap between the upper and lower arrays of magnets

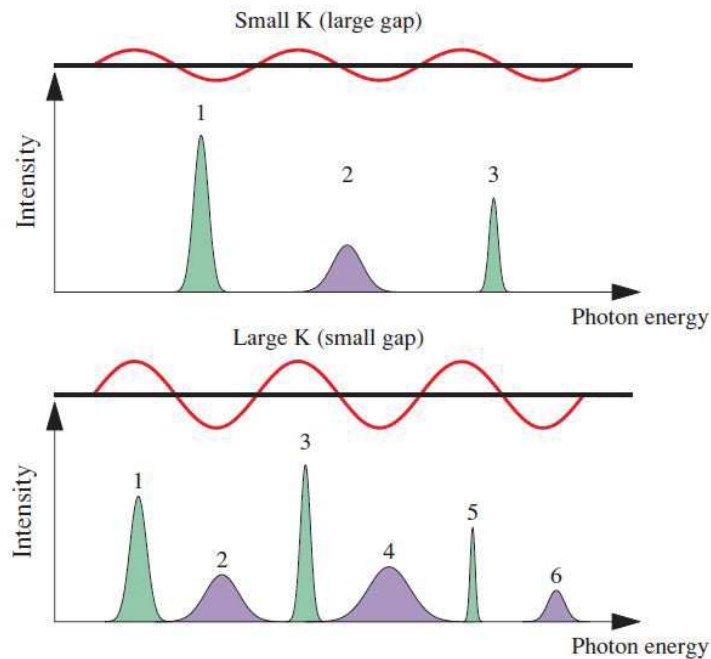


Figure 3.16: Undulator spectra for a smaller (top) and a larger (bottom) K value. Smaller K are achieved with a larger undulator gap, corresponding to weaker magnetic fields. This results in a less wavy trajectory with a consequent emission at higher energies, compared to higher K values.

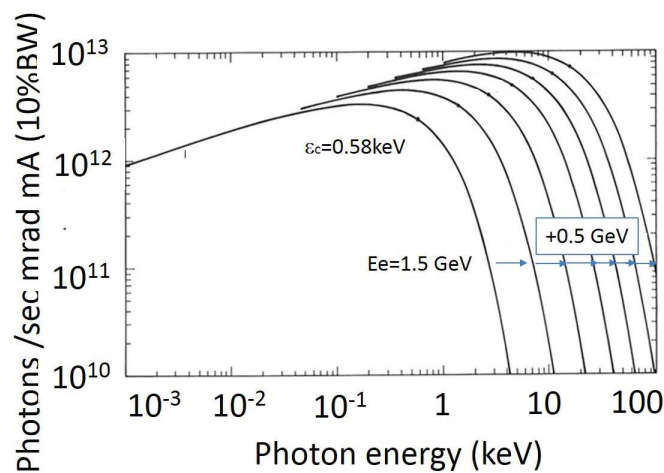


Figure 3.17: Spectral distribution of synchrotron radiation from a bending magnet. Dependence of the frequency distribution of the energy radiated on the electron beam energy.

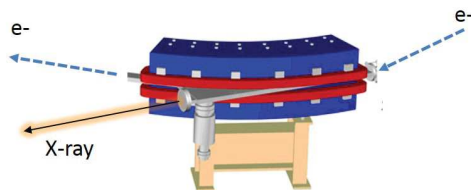


Figure 3.18: When an electron bunch enters a bending magnet (right arrow), it travels in a region where it is bent by a magnetic field. Therefore, one has two “exits” of the bending magnet: one for the electrons, and one for the X-ray photons, emitted tangentially.

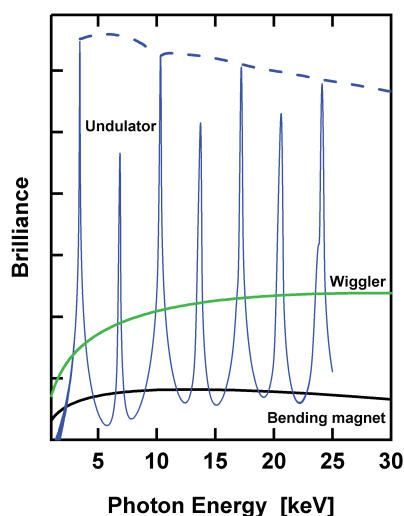


Figure 3.19: The spectra for a bending magnet and an undulator is reported to facilitate the comparison among the two. While the emission of the former is continuous and covers uniformly a broad range, the latter has several peaks of high intensity. The plot also reports the spectrum of a wiggler. Wigglers are similar to undulators but their λ_u is not small enough to generate constructive interference of the radiation emitted by two consecutive bends. Therefore the final intensity is given by the sum of the intensities of each bend and is lower than the intensity produced by an undulator. Since wigglers are not used at the ESRF, they are not further discussed in the text.

continuous spectrum, like the one in Fig.3.17. For $E \gg E_c$ ($\lambda \ll \lambda_c$), the spectral distribution falls off exponentially while for $E \ll E_c$ ($\lambda \gg \lambda_c$) it decreases slowly, practically independently from the electrons energy and mainly determined by the current of the machine.

Compared to the undulators, this radiation is less focused and less brilliant. In Fig.3.19, the reader has a reference plot to compare the intensity produced by the two devices over a broad range of photon energies. The undulators produce high intensity beam at selected wavelengths, whereas the bending magnet produces a less intense beam covering uniformly a broad range of wavelengths. The former is adequate when a high brilliance is needed: this is the case of surface diffraction where the scattering cross section is intrinsically low and the diffracted beam has to be increased by any means. In absorption spectroscopy, BM are preferred, since the energy scans can be performed without making too many corrections, thanks to the uniform beam.

Since the elements of each beamline are chosen to optimize data collection for a specific technique, a description of the two beamlines used in this work is provided.

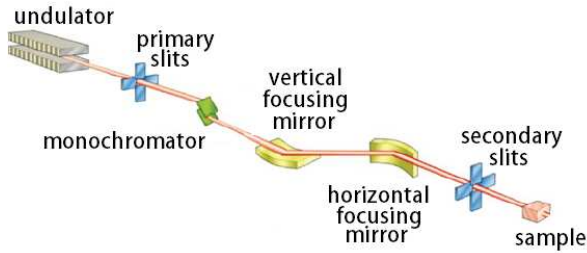


Figure 3.20: The beam produced in the storage ring is further refined to suit the need of each beamline. The figure shows how the beam produced in an undulator is resized by the use of two sets of slits, monochromatized cutting away unwanted wavelengths, and focussed using mirrors.

3.2.1 Beamlines

In general, the beamlines are all made up of two basic elements: the optics controlling the beam characteristics like size, focus, and energy, and the experimental apparatus to perform the experiment.

Each beamline is optimized for a given technique and requires different beam parameters. Therefore, each one has a dedicated "optics hut" which is used to tailor the beam to the needs of that particular technique.

As shown in Fig.3.20, typical functions of the optics hut are those of selecting a certain wavelength (through a monochromator), focusing the beam (using mirrors), and resizing it (with slits).

After the optics, one finds the experimental station which hosts the sample environment and the detectors.

3.2.2 BM23: the XAFS beamline

BM23 is the ESRF's general purpose X-ray absorption spectroscopy beamline. It is a bending magnet beamline optimized for standard EXAFS in a large energy range (5-75 keV) allowing to study K-edges of elements in the range $22 < Z < 76$. The strengths to which BM23 operates arise from the intrinsic properties of the ESRF synchrotron, coupled with a bending magnet source and the high quality performance of the beamline's principle optical element, its monochromator.

The BM23 source is located on a standard ESRF bending magnet with $B = 0.85 T$. The source size is $\sigma_z = 36.9 \mu m$ rms and $\sigma_y = 126 \mu m$ rms in the vertical and horizontal directions, respectively. The beamline accepts, through the primary slits located at 23 m from the source, a maximum divergence of $25 \mu rad$ in the vertical and 0.5 mrad in the horizontal directions. This leads to a maximum flux of 1.6×10^{12} photons s^{-1} ($0.1\% BW^{-1}$) at the ESRF critical energy (21 keV). The beamline vacuum is separated from the accelerator vacuum by a 0.5 mm-thick Be window.

The first optical element (see Fig.3.21) is a double-crystal monochromator

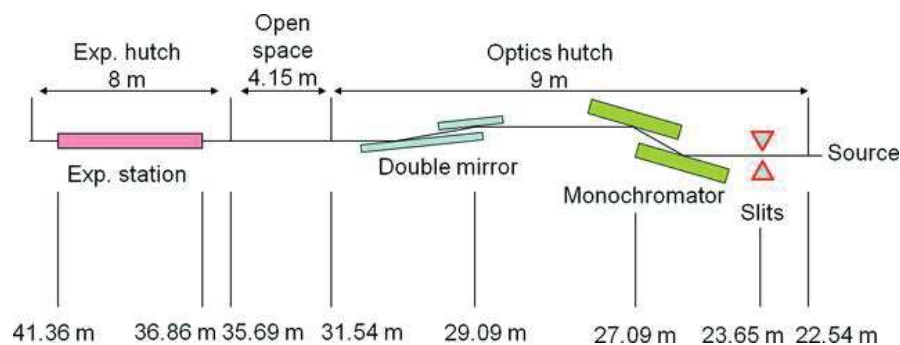


Figure 3.21: BM23 optical layout. Image from [57]

manufactured by Kohzu (Japan). The two crystals diffract in the vertical plane and allow one to access an angular range of $4.5 \div 35^\circ$. They are mounted on a single rotating plate whose rotation axis lies on the surface of the second crystal. The exit beam maintains a constant height during Bragg rotation.

The crystal support within the monochromator vacuum vessel can host three pairs of Si crystals. During the measurements carried out for this work, the Si(111) was used.

The second optical element, located after the monochromator, is a double-mirror system for harmonic rejection. It is based on total reflection through a double X-ray mirror configuration with an incidence angle variable from 2 to 5 mrad on three different stripes: Si, Pt and Rh. The first mirror lies flat and deflects the X-ray beam downwards. The second mirror deflects the X-ray beam upwards. The system allows harmonic rejection to better than the 10^{-5} level over the $5 \div 40$ keV energy range [57]. During an EXAFS scan the system does not move.

In the experimental station, a massive granite block of $1.2 \text{ m} \times 4.5 \text{ m}$ meant to damp the vibrations, lies as a support for the rest of the instrumentation (detectors and sample environment). On this support, there is room for many experimental configurations. This is where the two vacuum chambers used in this thesis were placed during the experiments (details will be provided in the next Chapter).

The beamline is optimized for transmission and fluorescence measurements and provides its users with three types of detectors:

- **Ionization chambers:** these detectors [58] coupled to medium/high-sensitivity amplifiers [59] allow transmission measurements of sample and reference simultaneously. The current amplifiers are equipped with an integral voltage-to-frequency converter which is optically coupled to the counting card.
- **Vortex Si Drift Detector (SDD):** with 1 mm-thick active material

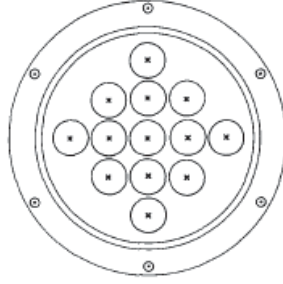


Figure 3.22: Arrangement of individual Ge detectors on the array.

and CUBE pre-amplifiers (from XGlab) [60]. The readout is performed via a single-channel DXP Mercury module from XIA LLC. This detector operates in fluorescence mode, allowing to measure the intensity of the photons emitted by the sample while decaying to a relaxed state.

- **13-elements Ge:** used for fluorescence measurements [61]. It has an active area of 13 mm² and is represented schematically in Fig.3.22. The Ge detector is coupled to a DXP-xMAP readout electronic from XIA LLC. This configuration demonstrates linear operation up to a maximum input count rate of 80000 counts per second per channel. This detector has 13 independent elements which operate simultaneously allowing to identify and remove fast artefacts such as Bragg peaks. Moreover, after discarding data acquired by one of the elements, the data collected from the other elements will be preserved. As a consequence, the statistics will not be compromised.

The XAFS measurements carried out for this work, were collected in fluorescence geometry. The impinging beam was oriented so that it made an angle of about 90° with the direction of detection. This geometry minimized the noise coming from elastically scattered photons. In this condition, for a thick sample, the fluorescence intensity is:

$$I_f(\omega) = I_0(\omega) \frac{\Omega}{4\pi} \eta \frac{\mu_a(\omega)}{\mu_{tot}(\omega) + \mu_{tot}(\omega_f)} \quad (3.9)$$

with I_0 impinging flux, $\frac{\Omega}{4\pi}$ solid angle of detector acceptance, and η fluorescence yield.

3.2.3 ID03: the surface diffraction beamline

ID03 is an undulator beamline dedicated to surfaces and interfaces structural characterizations. The beamline can be used for performing static surface crystallography studies or for studying processes at surfaces in real time. The

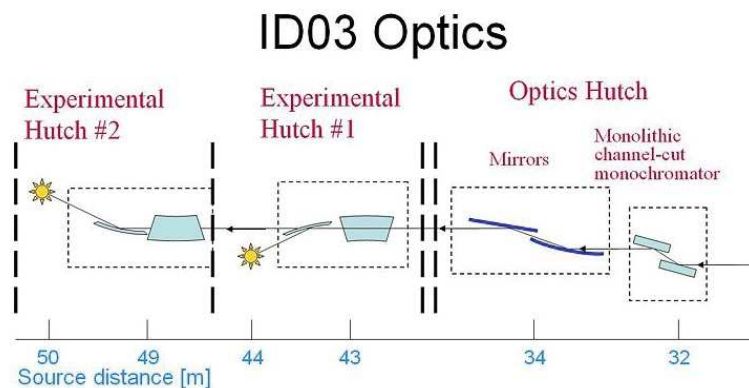


Figure 3.23: Schematic representation of ID03 optics Hutch.

photon energy is continuously tunable in the range 5÷24 keV giving the possibility of performing measurements at resonance for most of the elements.

Like the other ID beamlines, ID03 can control the corresponding undulator placed immediately upstream to it. In particular, ID03 controls three undulators: two U35 ($\lambda_u = 35$ mm) and one U32 ($\lambda_u = 32$ mm). The minimum undulator gap is 11 mm and is defined by the thickness of the insertion device vessel thickness (10 mm). Thanks to the high power front end of ID03, one can use the minimum gap on more than one undulator simultaneously.

The photon flux available exceeds 10^{13} photons/s in the whole 5-24 keV energy range and the source size is $140 \times 50 \mu\text{m}$ (fwhm) HxV, with a beam divergence of $210 \times 16 \mu\text{rad}$ (fwhm) HxV.

The beamline is divided in three main hutches shown in Fig.3.23: the optics hutch (OH) and two experimental hutches called Experimental Hutch 1 (EH1) and EH2.

Optics Hutch

The optics hutch provides a monochromatic and focused X-ray beam to both experimental hutches EH1 and EH2. The ID03 beamline is windowless, thus the first beamline component is a differential pumping system, which decouples the vacuum of the beamline from the one of the synchrotron ring.

The first optical component of the beamline is a couple of high power primary slits installed at 31.5 m from the source. Next to them, one finds the attenuators and a calorimeter vessel. At 32 m from the source, there is a monochromator based on the use of a monolithic channel cut Si (111) crystal cooled at liquid nitrogen temperature. This feature provides stability but does not allow any focusing.³

³The monochromator energy range goes from 3 keV to about 50 keV. However, the

The beamline optical design is based on a toroidal mirror with a controllable meridional focusing made up of a bendable cylindrical Si piece. The mirror, mounted at 35.5 m from the source, has a sagittal radius of 32 mm and a tunable meridional radius ranging from 5 km to 16 km. A second flat mirror is mounted on the same vacuum vessel and support. Its function is to put back the X-ray beam in the horizontal direction. Both mirrors are Pd-coated: the K-absorption edge of palladium at 24.35 keV defines the high energy cut-off of the beamline. With an appropriate choice of the incidence angle and of the sagittal radius, it is possible to focus the X-ray beam down to a theoretical value of about 50×30 fwhm (HxV) in any point of the two experimental hutches, EH1 and EH2. The beam focused by toroidal mirrors has a highly anisotropic, cigar-shaped resolution function. In grazing incidence experiments, this can become a great advantage, as the long direction of the resolution function can be aligned with the Bragg rods from the surface, thus maximizing the signal rate [34]. This is achieved in EH2, where the normal to the sample surface lies in the storage ring plane. At the entrance of each experimental hutch there is a Kirkpatrick-Baez (KB) mirrors system: when this is used, the two elliptical mirrors focus the beam both horizontally and vertically and produce a beam size of the order of few μm on the sample. In particular, they can use the focal point of the toroidal mirror as source for further demagnification of the source.

Experimental hutches

The beamline has two experimental hutches: each one is equipped with a diffractometer. For both diffractometers, Maxipix area detectors can be used. They provide noise-free X-ray images, high dynamic range, small pixel size, high frame rate and high spatial resolution.

The first experimental hutch (EH1) hosts a vertical z-axis diffractometer and is specially suited for samples with a horizontal surface geometry (liquids, electrochemistry environment etc.).

The second experimental hutch (EH2) hosts a horizontal z-axis diffractometer coupled with a UHV chamber. The diffractometer, shown in Fig.3.24, allows to rotate sample and detector around several axes.

The sample is fixed to a sample holder, shown in Fig.3.25. The back of the sample is in contact with a Boraelectric surface allowing the user to perform annealing treatments. The sample holder is mounted on a hexapod, which guarantees a fine sample alignment on the beam position. The sample can be prepared *in-situ* using one or several evaporators. Moreover, additional detectors can be mounted on users demand. Ion sputtering for sample surface cleaning, and a Cylindrical Mirror Analyser (CMA) for Auger spectroscopy, are available with the sample in the diffraction position. The sample can be

beamline design is optimized for the 5-24 keV energy range, as explained below.

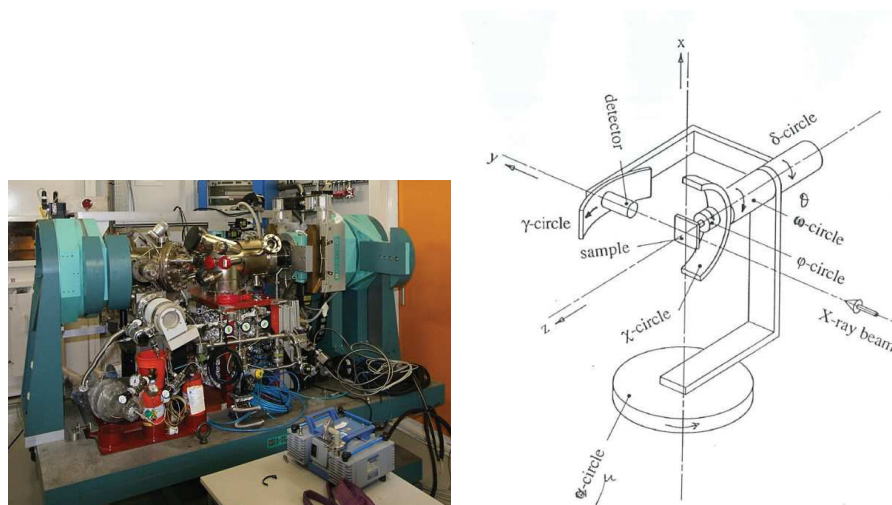


Figure 3.24: **Left:** an image of EH2 of ID03. **Right:** schematic representation of the rotation angles for diffraction measurements.

heated up to 1000 °C (flash), 600 °C (continuous) and cooled down to about -190 °C.

The data this work focuses on, were collected in EH2 during XRR and GIXD measurements. In the XRR scans, the angle between the sample surface and the beam μ and the angle between the reflected beam and the surface γ were increased simultaneously. Therefore, the dataset collected carried information on the reflectivity profile for different values of the perpendicular momentum transfer.

Concerning the GIXD, datasets were collected using two different acquisition modes. A first one using grazing incidence and exit to the surface, the momentum transfer is kept nearly parallel to the surface. This allowed a determination of the in-plane structure, that is the 3D surface structure projected onto the surface plane. A second acquisition mode measures the intensity of the CTRs along the L direction. In this way one obtains the out-of-plane structure, the heights of the atoms relative to the bulk layers. The combination of this complementary information allows one to achieve a full, three-dimensional characterization.

Data refinement

Raw data have to be processed before being ready to be fitted. This process was handled through a software tailored on ID03 needs: BINoculars [35]. This program can use diffraction images to calculate HKL map, *i.e.* a map of the Bragg rod in reciprocal space. To do so, it converts all the image pixels into voxels in reciprocal space through a binning procedure. After the conversion,



Figure 3.25: Sample mounted on the sample-holder. Two screws are fixing a Tantalum wire holding the sample in place. Alternatively, a Ta clip can be used instead of the wire.

the data can be used for structure factor determination.

To correctly obtain structure factors in standard Surface X-ray Diffraction (SXRD) experiment, one needs to integrate the intensities in the HK planes at different L 's along the diffraction rod. The structure factor for each L can be determined by integrating the intensity of reflection in the slice. The FitAid tool in BINoculars, was used to integrate the data within a pre-selected ROI while normalizing the data to the background and to the number of voxels. The structure factors are then obtained as:

$$F_{hkl} = \sqrt{\frac{roi - \#roi}{\#bkg \cdot bkg}} \quad (3.10)$$

The integration procedure starting from the diffraction images is represented in Fig.3.26 and it is described in details in [35].

The integrated data were then fitted using the GenX code [32].

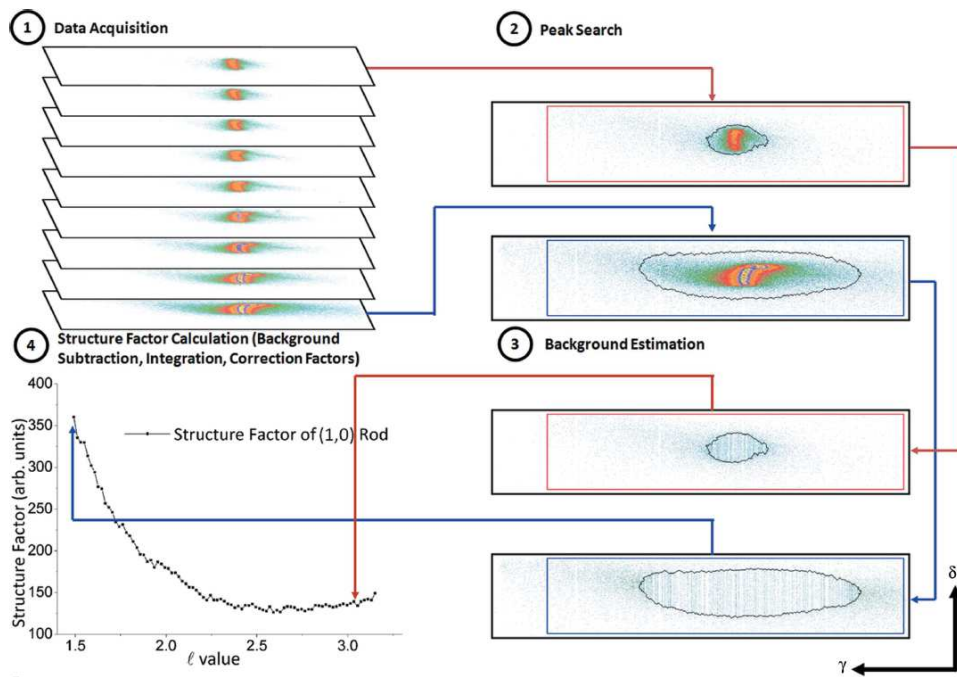


Figure 3.26: Complete analysis procedure of stationary l scans. The example used here is a $(1, 0, \ell)$ scan of an Ir(111) sample. Image from [35].

Experiments and results

In the frame of the magnetic behaviour of Co films upon intercalation, many effects have to be considered. In facts, the overall effect comes from the interplay among the Co-C interaction, the thermal effects and the Co-Ir interaction, the coupling between Co atoms in different chemical environments, structural evolution, etc...

In order to identify and isolate each contribution, we started investigating the bare Co/Ir systems, where the C atoms were not present. This allowed us to focus on the thermal effects on the structural evolution and Co-Ir interaction. The results obtained with these samples were then compared to the Gr-covered Co/Ir systems. The comparison provided elements for isolating the Gr role. These first investigations involved the combined use of XPS, LEED, and MOKE observations. Their results provided encouraging information which allowed us to move a step further using synchrotron radiation techniques.

In the following, we will present the analysis of some of the collected data. Combining several techniques, we provide experimental results aiming to describe different aspects of the systems. In particular, we focused on:

- the Graphene effect on the long-range order at the Co-Ir interface,
- the deposition and intercalation dynamics,
- the structural evolution of the Co film due to thermal effects, and
- the Gr efficiency in preventing Co oxidation under ambient pressure and the microstructural analysis of intercalated Co films.

The results are presented in four different sections following the different experiments we carried out.

4.1 The Graphene's effects

The first analysis we present proves that the system is actually worth to be extensively studied. The measurements were carried out both on bare and on

Gr-covered Co/Ir systems. From the comparison of the two, it is possible to identify the intercalation effect.

Experimental details

Synchrotron radiation measurements were performed in the EH2 at ID03 (described in Sec.3.2.3). The UHV chamber had a base pressure of 10^{-10} mbar. The samples have been characterized *in-situ*, with an Auger spectrometer and coupled with a 6-circle diffractometer. The 24keV incident X-ray beam was focused at the sample position to the size of $50 \times 20 \mu\text{m}^2$ in the horizontal and vertical directions respectively. STM and XPS measurements were conducted in separate chambers with similar base pressures.

The Ir(111) single crystals were prepared following the same procedure in all three chambers. The procedure consisted of repeated cycles of 2 keV Ar^+ ion bombardment, 5 min annealing at 1000 °C under $5 \cdot 10^{-8}$ mbar partial pressure of oxygen, followed by a final short annealing (1 min) at the same temperature with no oxygen. In EH2, the surface cleanliness was checked by Auger electron spectroscopy and measurement of crystal truncation rods (CTRs). Gr was grown by exposing the Ir substrate, kept at 600 °C, to ethylene at the pressure of $1 \cdot 10^{-7}$ for 40 min. Cobalt was evaporated on bare Ir(111) and on Gr/Ir(111) at room temperature (RT) using electron bombardment. The amount of material deposited on the substrate was determined by fitting of the XRR profiles (in EH2) and by XPS analysis (in the preparation laboratory).

A first sample was prepared in the preparation laboratory, evaporating 4 ML of Co onto Gr-covered Ir(111). Then, the sample was annealed to 300 °C in order to induce intercalation. The success of the intercalation was monitored through the integrated intensity of the XPS C_{1s} peak (normalized to the pre-edge value). As it is shown in Fig.4.1a, this value drops after the Co deposition but it goes back to the original value after the intercalation annealing.

Repeating the deposition/annealing cycle yields the same result in terms of C_{1s} peak intensity. This confirms the intercalation of Co. However, the C signal slowly decreases, suggesting that small amount of Co remains on the surface. Note that our experimental resolution (800 meV) is not enough to detect the expected few 100 meV core level shifts expected as a result of the distinctive interactions between graphene and Co or Ir [62].

The composition trends obtained by Angular Resolved XPS (ARXPS) are shown in Fig.4.1b. After deposition of 7 ML of Co on bare Ir(111), ARXPS shows a linear decrease typical of a uniform thin film (black curve): the $\text{Co}_{2p}/\text{Ir}_{4f}$ ratio strongly decays as the escape angle decreases, i.e. as the X-rays probe deeper into the sample. Successive annealing to higher temperatures cause a continuous decrease of the peak ratio, particularly at low escape angles where the technique is most surface sensitive. This can be interpreted as surface alloying [22], change in surface morphology [63] or both. At 600

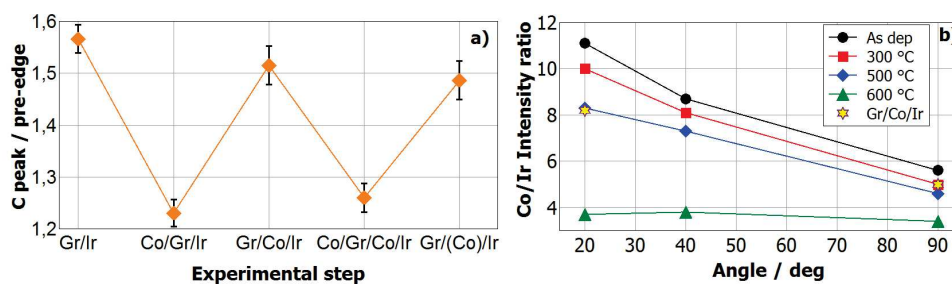


Figure 4.1: The efficiency of the intercalation process at 300 °C is followed with the normalized intensity of C_{1s} XPS peak and ARXPS composition trends are plotted in (b). The Co(2p)/Ir(4f) XPS peak ratios at different photoelectron escape angles are shown for Co film deposited on Ir(111) surface (black) and upon annealing to 300 °C (red), 500 °C (blue) and 600 °C (green). The yellow star points refer to the Gr/Co/Ir(111) heterostructure made after second intercalation at 300 °C in panel a). The escape angles are referring to the surface plane.

°C (green) the angular dependence of Co/Ir XPS ratio disappears and Co is homogeneously dissolved in the substrate.

The qualitative evolution of the Co morphology obtained by an observation of the XRR profiles (structure factors as a function of the reciprocal space coordinate perpendicular to the surface, L) is further discussed. XRR measured before and after Co deposition on clean Ir(111) (Fig.4.2a and b) reveals that the Co/Ir interface has a very low roughness, similar to the one of the clean Ir(111) surface. This is indicated by the similar values of the structure factors at the anti-Bragg region at $L \simeq 1.5$ in reciprocal lattice units (r.l.u.) of the specular rod. On the contrary, the vacuum/Co interface is rough at the scale of the X-ray beam coherence length ($\simeq 1 \mu\text{m}$), as shown by the strong damping of the fringes. This is characteristic of a granular film as confirmed by STM. Annealing at 500 °C for 5 min yields a Co thin film with a sharp Co/Ir interface and with a low surface roughness, as demonstrated by the presence of well defined fringes (Fig.4.2c). The STM images support this view showing a smooth Co film surface. From the fringe period we can estimate the Co film thickness to be about 6 ML.

The morphology of the thin Co film is different in presence of Gr. Co deposition at room temperature, yields a very inhomogeneous film, as indicated by the total absence of interference fringes (Fig.4.2d and e). The Gr/Ir(111) substrate seems practically unmodified by the presence of the Co layer, as indicated by the very similar XRR profiles in the region between $L = 0.5 \div 2.5$ r.l.u. This picture is validated by STM, which reveals that Co deposition results in the formation of nano-clusters. Annealing at 300 °C (5 min) followed by 500 °C (5 min) results in a strong decay of the anti-Bragg structure factor, accompanied by the appearance of faint fringes (Fig.4.2f). This is a signature

for a rough Co/Ir interface. STM images show that the surface of the system is much flatter than before and that Gr is again visible, confirming Co intercalation. Bright nanometer-scale bumps, on top of which Gr's honeycomb lattice appears with a different contrast as compared to flat regions, translates to a local change of density of states. This could be a signal a local inhomogeneity of the intercalated Co layer, either a point defect or locally thicker Co (by 2 Å or 1 ML).

To gather more quantitative insight into the structure of the system, we fitted the XRR data using a modified version of the ROD code [31]. The fit procedure relied on two χ^2 minimization algorithms: first, simulated annealing started with different sets of initial parameters was employed to approach the global χ^2 minimum; second, a Levenberg–Marquardt procedure allowed for final refinement of the fit parameters. The optimal model was chosen by the lowest χ^2 with the condition that the number of fringes corresponds to the observation. The fit of the clean Ir XRR curve was carried out assuming three free structural parameters: the vertical position of the last Ir layer, the roughness and Debye–Waller parameter. The fit shows the absence of any vertical relaxation of the top layer and the distance between the top two atomic Ir layers is $d_{Ir-Ir} = 2.21 \pm 0.01 \text{Å}$, equal to the bulk value, while the surface roughness is $0.2 \pm 0.1 \text{Å}$. The fit of the XRR data measured after deposition of Co at room temperature also allows us to determine the thickness of the Co layer, equal to $12.4 \pm 1 \text{Å}$ ($6.2 \pm 0.5 \text{ ML}$). The structure of the Ir substrate remains practically unmodified with respect to the clean Ir case while the distance between the topmost Ir atomic layer and the first Co atomic layer is $d_{Co-Ir} = 2.05 \pm 0.02 \text{Å}$, similar to the bulk Co–Co distance of 2.035 Å . The fit value for the RMS surface roughness is $\sigma_{v/Co} = 2.1 \pm 0.1 \text{Å}$. The main effect of the 500°C annealing (5 min) is to decrease the vacuum/Co $\sigma_{v/Co}$ roughness from 2.1 to $0.9 \pm 0.1 \text{Å}$ (see Tab.4.1). We let vary the composition of the interface to check the sensitivity of the data to the intermixing, however, the fit indicates the intermixing is limited to 1 ML and less than 10% in atomic units.

The fit of the clean Gr/Ir(111) XRR curve, (Fig.4.2d), provides the Gr–Ir atomic planes average distance $d_{C-Ir} = 3.22 \pm 0.08 \text{Å}$. This value is slightly smaller than the $3.38 \pm 0.04 \text{Å}$ determined by the X-ray standing wave technique in the case of high quality Gr prepared at a temperature higher than in the present work) on Ir(111) [64]. We interpret this difference as the effect of locally strong C–Ir bonds at the numerous point-defects sites. The high defect density is confirmed by STM measurements which reveal, beside the presence of point-like defect, the existence of several Gr domains with different orientations (three of them are highlighted as blue circles in Fig.4.2d). The distance between the top two atomic layer of the Ir(111) surfaces is contracted, with respect to the clean Ir surface, to a value of $d_{Ir-Ir} = 2.11 \pm 0.01 \text{Å}$.

After RT Co deposition of $4.5 \pm 1 \text{ ML}$ of Co, d_{C-Ir} further decreases to 2.90

Sample	$d_{Ir-Ir}(\text{\AA})$	$d_{Ir-Co}(\text{\AA})$	$d_{Ir-C}(\text{\AA})$	$d_{C-Co}(\text{\AA})$	$d_{Co-C}(\text{\AA})$	$t_{Co}(\text{ML})$	$\sigma_{v/Co}(\text{\AA})$	$\sigma_{Co/Ir}(\text{\AA})$
Ir(111)	2.21±0.01	-	-	-	-	-	-	-
Co/Ir(111) (RT)	2.21±0.01	2.04±0.05	-	-	-	-	2.1±0.1	0.5±0.1
Co/Ir(111) (500°C)	2.11±0.20	2.04±0.05	-	-	-	-	0.9±0.1	0.9±0.1
Gr/Ir(111)	2.11±0.01	-	3.22±0.08	-	-	-	-	-
Co/Gr/Ir(111)	2.13±0.02	-	2.90±0.13	1.74±0.09	-	-	10.0±5	-
Gr/Co/Ir(111) (500°C)	-	-	-	-	2.12±0.20	1.5±1.0	-	2.0±0.1

Table 4.1: Distance between Gr and Ir(111) (d_{C-Ir}), distance between Co (on top of Gr) and Gr (d_{Co-C}), distance between Gr and intercalated Co (d_{Co-Co}), intercalated pure Co thickness (t_{Co}), roughness of the topmost Co/vacuum interface ($\sigma_{v/Co}$), and roughness of the Co/Ir(111) interface ($\sigma_{Co/Ir}$), for the different samples studied in this work: the bare Ir(111) substrate, Co deposited (12.4Å or 6.2 ML) at room temperature (RT) on Ir(111), the same sample annealed at 500 °C for 5 min, Co deposited on Gr/Ir(111) at RT (9Å or 4.5 ML), Co intercalated between Gr and Ir(111) at 300 °C (5 min) followed by 500 °C (5 min).

± 0.13Å. This value, together with the small Co-Gr distance $d_{Co-C} 1.74 \pm 0.09$ Å Tab.4.1 seems consistent with a local sp^3 hybridization of C atoms below Co clusters, involving the formation of additional covalent-like C-Ir bonds, similar to the case of Pt and Ir clusters on Gr/Ir(111). The structure of the Ir substrate does not practically change ($d_{Ir-Ir} = 2.13 \pm 0.02$ Å).

Heating to 300°C for 5 min, then to 500°C for 5 min, results in the intercalation of Co below the Gr. The fit of the XRR curve is more complex. The model we use consists of up to 5 ML of the Ir(111) substrate free to intermix with Co, a non-mixed intercalated Co layer with variable thickness and a Gr layer. The best fitting structure consists of a thin Co layer with a thickness of 1–2 ML sandwiched between the Gr and Ir(111) alloyed with Co. The intermixed region in the Ir(111) substrate is about 2–3 ML. In the best fit model, some Co atoms are missing ($\simeq 1$ ML) with respect to the total amount of Co we deposited and this can be explained in three different ways:

1. some Co is still present above the Gr and it is not accounted for;
2. small part of the Co diffused further into the substrate;
3. our estimation of initial Co thickness after deposition is inaccurate.

Unfortunately, our data do not allow us to discriminate among three cases due to the relative insensitivity of the XRR fits to the parameters related to the above mentioned scenarios.

The XRR results are summarized schematically in Fig.4.3, where electron density profiles projected in the direction perpendicular to the surface are plotted together with the best fit models. XRR profiles, as Fourier transforms of the electronic density perpendicular to the surface, are especially sensitive to the abruptness of the interfaces. Therefore, the fits discriminate well between

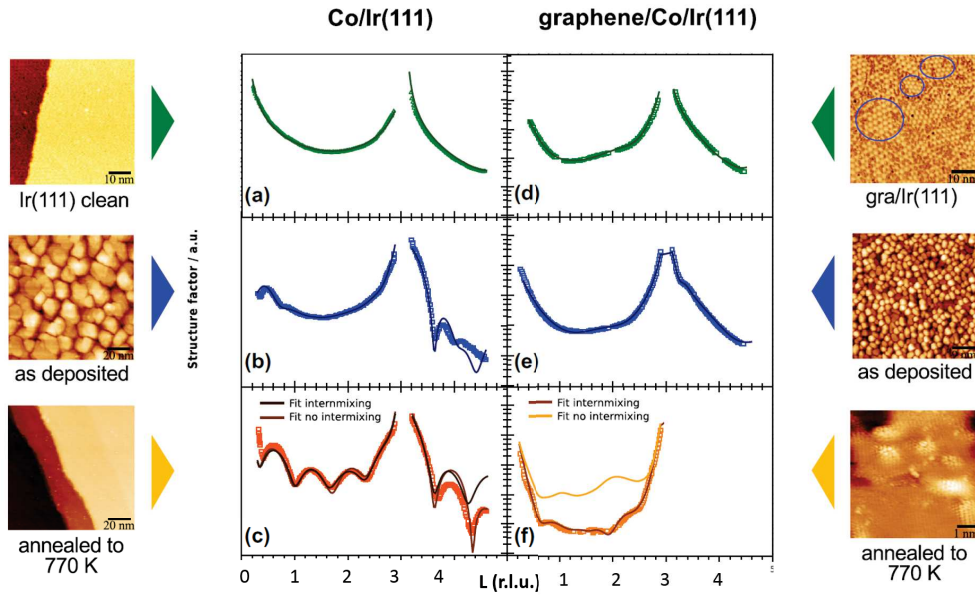


Figure 4.2: XRR profiles (structure factors as a function of the out-of-plane L reciprocal space coordinate) measured at RT (symbols) and fitted (solid lines, see text for details) for **a)** bare Ir(111), **b)** Co deposited on Ir(111) at RT, **c)** the same sample annealed at 500 °C for 5 min, **d)** Gr on Ir(111), **e)** Co deposited at RT on Gr/Ir(111), and **f)** the same sample first annealed at 300 °C for 5 min and then further annealed at 500 °C for 5 min (f). Corresponding STM images are shown on the side. The structure factors for $L > 3$ r.l.u. in **f)** are very sensitive to the structure of the intermixed region which is unknown and are, therefore, not fitted. The structure factors were obtained from raw data as described in [35]. Image from [21].

the sharp (non-intermixed) and rough (intermixed) interfaces and the electron profiles in top plot of Fig.4.3 result in significantly different XRR curves.

The morphology of the Co thin film after intercalation can finally be described as follows. The nominally 4.5 ML deposited Co layers have been almost entirely intercalated after a 5 min annealing at 500°C. Below the Gr is a Co slab, 1–2 ML thick, laying on a 2–3 ML Co/Ir alloy layer, whose Co content decreases with thickness and vanishes completely 4 ML below the pure Co slab. The observed behaviour strongly depends on the initial thickness of Co layer and the annealing procedure, which are the key parameters to prepare sharp or alloyed interfaces in Gr/Co/Ir(111) heterostructures¹. Thick layers do not show signs of alloying upon intercalation and, in contrast, steeper temperature ramp facilitates alloying. It is emphasized that surface alloying occurs when the Co is intercalated at elevated temperature (500°C).

¹More details will be provided in the following sections.

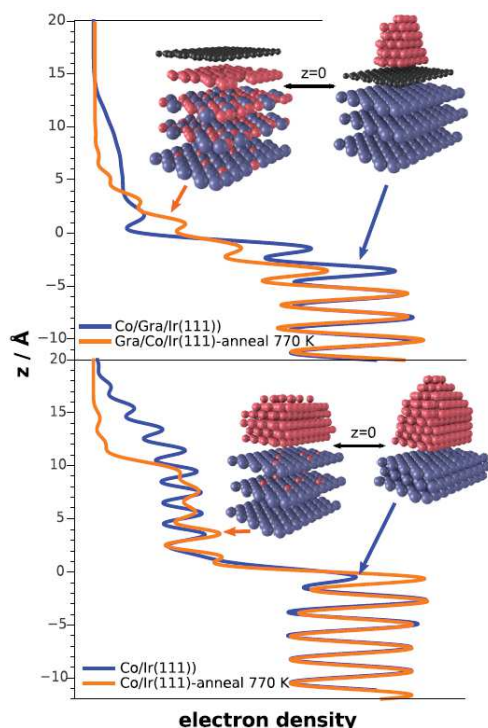


Figure 4.3: Electronic density profiles projected in the z direction perpendicular to the surface as deduced from fits of the XRR data, for Co deposited on Ir(111) at RT (bottom plot, blue line), the same sample annealed at 500 °C (bottom plot, orange line), Co deposited on Gr/Ir(111) at RT (top plot, blue line), Co intercalated between Gr and Ir(111) at 500 °C (top plot, orange line). The z -axis origin is set at the bottom of the pure Co region. Image from [21].

Conclusions

The two situations addressed in our work, with and without Gr, differ in the way Co atoms interact with the Ir substrate. Defective Gr actually acts as a colander, letting Co atoms passing with a low flux and reaching the Ir interface in a dilute phase, unlike after they have been deposited directly on top of Ir(111) at room temperature. We speculate that in the former case, the low coordination of the Co atoms on Ir facilitates their penetration inside the Ir substrate. This penetration does not consist in a diffusion via interstitial crystallographic sites of Ir, but rather by atomic exchange between Ir and Co atoms. We are lead to conclude that the kinetic barriers for this exchange are low, and that with the 5 min annealing the system reaches a close to equilibrium state, implying strain-induced intermixing [65], characterized at 500°C by 2–3 ML of varying Co–Ir composition.

In conclusion, we show that a presumably strain-induced intermixing, involving the bottom 2 ML of the intercalant, occurs during Co intercalation at 500°C. The intermixed layer is formed as a result of a low intercalation flux through the Gr colander, which provides an alternative pathway to the usual lattice mismatch accommodation between intercalant and substrate occurring via an interface dislocation network. We have to stress that the presented results are valid only for the indicated temperatures and for the defective Gr. Different annealing temperatures may lead to a different intermixing as will be

discussed in the following sections. Here we have to highlight that the extent of intermixing is much lower when Co is intercalated at 300°C, which is the temperature used in previous reports [14, 1].

4.2 Intercalation dynamics

The previous analysis shows how the intercalation under Gr results in an interface roughening not observed for the bare Co case. From the data collected in our experiments and those available in literature, the most reasonable explanation for the roughening is a strain-induced intermixing. This process is facilitated by the film integrity loss upon intercalation due to the action of the Gr.

However, since the two systems compared in Sec.4.1 have different thickness, the roughening process cannot be related to the Gr presence until two questions are answered:

1. Does the different thickness of the films in Sec.4.1 play a role?
2. Is the “colander picture” accurate?

In order to answer these questions, we ran a new series of experiments involving XRR and GIXD.

To answer to question #1, we studied two films obtained evaporating the same amount of Co on Ir and on Gr/Ir. In this way, we could verify the Gr effect.

The answer to question #2 was needed to explain why the bare Co/Ir system did not show the same interface roughening as the Gr-covered one. If the colander picture was actually accurate, then even the Co/Ir systems interface would be expected to roughen reproducing the colander effect. This effect occurs when the Co get in contact with the hot Ir substrate. In the case of the intercalated Co, this requires the film to be broken down into small clusters or single atoms while passing through the Gr defects. In order to reproduce such conditions, we deposited the Co while keeping the Ir substrate at high temperatures. In this way, the Co coming from the evaporator touches the hot Ir substrate gradually, as single atoms. The comparison of this system with the case of a RT-deposited film, heated as a whole, could shed light on the questioned colander effect.

In the following, we present the XRR and GIXD experiments we carried out. Later on, we report the answers to the two questions on the basis of the obtained results.

In the following we will show and compare the SXRD measurements of the Gr/Co/Ir systems with those of RT- and hot-deposited Co/Ir systems. For the three samples we analysed, the substrate preparation procedure is the same we have outlined in the previous section. The Gr growth was carried out at 600 °C.

		Pristine	300 °C	500 °C
Co	$t =$	13.2 ± 0.2	13.6 ± 0.1	13.6 ± 0.2
	$r =$	3.1 ± 0.1	1.6 ± 0.1	1.2 ± 0.1
Ir(111)	$r =$	2.3 ± 0.1	0.7 ± 0.1	0.9 ± 0.1

Table 4.2: Structural parameters evaluated from the XRR fitting of the bare Co/Ir sample. r stands for roughness, t for thickness. All values are in Å.

4.2.1 The thickness dependence

Dealing with surfaces and interfaces, the thickness dependence is rather strong and even few MLs of difference can affect a system's response. In order to disentangle the Gr contribution from possible thickness effects, we carried out XRR and GIXD measurements on two films grown using the same Co deposition times. In particular, in both cases Co was deposited at RT for 8 min on two substrates: clean Ir(111) and Gr/Ir(111).

After the Co evaporation, both films were characterized by XRR to check their thickness and roughness. The measurements were repeated upon annealing at 300 °C, and at 500 °C. The results are reported in Tab4.2 and 4.3 for the bare and Gr-covered film respectively. The bare film was found to be 13.2 ± 0.2 ML corresponding to $\simeq 6.5$ ML with an initial surface roughness (rms) of 3.1 ± 0.1 Å. The interface roughness is evaluated to be 2.3 ± 0.1 Å. This value is compatible with the granular Co growth observed in Sec.4.1. The effect of the annealing is to smooth both the surface of the film and its interface with the substrate.

In the Gr-covered film, the model used to fit the data was made up of three layers: a Co film, a Gr layer and an Ir substrate. No intercalated Co layer was used to fit the XRR profile measured on the pristine film. The calculated roughness is comparable to the film thickness, implying a high uncertainty in the estimation of the thickness value. As in the bare Co case, this can be explained with the highly irregular, granular growth of Co on Gr. The best fit model of the XRR data measured upon the two thermal treatments takes into account the possibility of partial intercalation and it is shown in Fig.4.5. Four layers were used: a topmost Co layer simulating some Co left on the Gr surface, a Gr layer, some intercalated Co and the Ir substrate. The annealing procedures bring some regularity to the system causing the roughness and uncertainties to decrease to acceptable values. Noticeably, the interface is smoothed by the annealing. This behaviour is opposite to what was observed in Sec.4.1.

The GIXD data collected in the same experimental conditions as the XRR are reported in Fig.4.4. The plot shows the intensity profiles of the diffracted

		Pristine	300 °C	500 °C
Co-top	$t =$	16 ± 4	9.7 ± 0.5	0.5 ± 0.4
	$r =$	15 ± 1	4.7 ± 0.3	1.9 ± 0.2
Gr	$t =$	3.3 ± 0.5	1.1 ± 0.1	1.7 ± 0.4
	$r =$	1.7 ± 0.3	1.4 ± 0.1	1.9 ± 0.4
Co	$t =$		3.8 ± 0.4	13.7 ± 0.1
	$r =$	/	4.0 ± 0.2	3.9 ± 0.2
Ir(111)	$r =$	2.3 ± 0.1	2.0 ± 0.1	1.7 ± 0.1

Table 4.3: Structural parameters evaluated from the XRR fitting of the Gr/Co/Ir sample. r stands for roughness, t for thickness. The model used to fit the data of the pristine film involves 3 layers: Co, Gr and Ir. After the annealing treatments, the best agreement was found for models accounting for some Co left on the Gr surface. The 4 layers are reported from the topmost (first row) to the substrate (bottom row). All values are in Å.

beam around the Ir (1,0) reflection collected at $L = 0.3$ r.l.u.. Solid lines refer to the bare Co films, whereas dashed lines to the Gr-covered films. The value $H = 1.08$ r.l.u. corresponds to a distance of 2.51 Å in real space, that is the Co bulk lattice parameter. Therefore, peaks around this value can be ascribed to the Co film.

In the case of bare Co/Ir, the evolution of the Co peak reveals an improvement of the Co crystalline quality upon the thermal treatments: this is evidenced by the decrease of the peak width and the rising of its intensity. This interpretation is compatible with the surface and interface smoothing observed with the XRR analysis reported in Tab.4.2.

In the case of Gr-covered Co film (dashed lines) we observe a rather broad peak for the pristine film whose maximum value lies slightly above $H=1.08$ r.l.u., indicating an average lattice parameter being slightly compressed with respect to bulk Co. This is compatible with the presence of small Co regions with dimensions of few nanometers [66]. This picture, already observed with STM in Sec.4.1, is confirmed by the large width of the peak and by the high roughness of the film as suggested by the XRR (Tab.4.3).

Upon the 300 °C annealing, the lattice parameter is back to the bulk value $H = 1.08$ r.l.u. $\Rightarrow 2.51$ Å, the peak intensity is higher, and the width is reduced. These effects are enhanced upon the 500 °C annealing. On the contrary of what observed in Sec.4.1, the intermixing at the interface is not observed: nor in the perpendicular direction, neither along the film plane. This means that the interface modifications cannot be due to the presence of the Gr or, at least, they do not depend uniquely on the Gr presence. In other words, the interface roughening is thickness dependent as it is observed for a thin (6 ML) film below the t_c while it is not observed for a thicker film ($\simeq 7$ ML) lying in the thickness range where spin reorientation transition occurs.

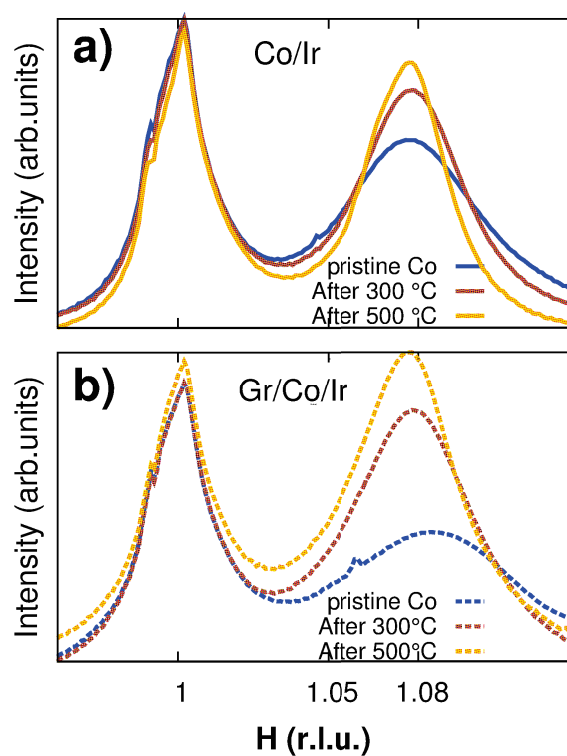


Figure 4.4: Intensity profile around the Ir (1,0) peak along the H direction for the bare Co/Ir sample (a) and for the Gr-covered Co film (b).

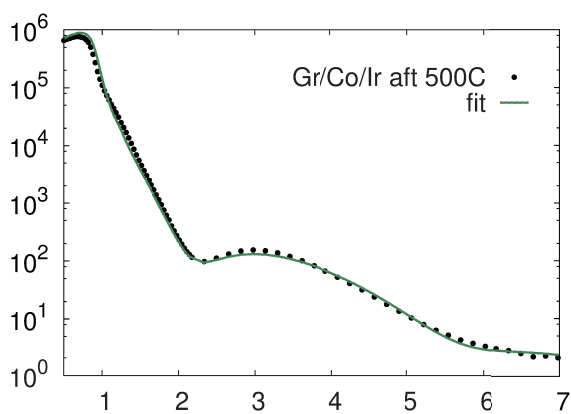


Figure 4.5: XRR profile of the Gr-covered Co film after annealing at 500 °C (black points) and fit to the data (green line). The fit was run minimizing a figure of merit (FOM) calculated as $\ln R^2$, with R being the residuals. The parameters estimated by the fit are reported in Tab.4.3.

4.2.2 The effects of deposition temperatures

As far as the accuracy of the colander picture is concerned, we tried to reproduce the Co integrity loss due to the crossing of Gr layer, performing a Co evaporation on a hot Ir substrate. This aimed to let the Co reach the hot substrate mostly as single atoms. Compared to the RT deposition, where the Co films interacts with the hot Ir as a whole film, the hot deposition enhances the surface effects and modifies the average chemical environment of Co atoms at the interface. In facts, dealing with smaller units like single atoms, the strain induced lattice expansion and/or intermixing, should be enhanced.

Our hot-deposition was performed at 500 °C. The film's thickness and roughness were evaluated after each experimental step from the XRR profiles, whereas the intensity profiles of the Ir (1,0) peak along the H directions (Fig.4.6) were used to monitor the in-plane lattice evolution. The results are compared to those discussed in the previous paragraph, referring to the RT deposited film after the 500 °C annealing.

From Fig.4.6, one can observe how the hot deposited sample (red line) shows a Co peak whose intensity overcomes that of the Ir peak, and whose maximum lies around $H = 1.06$ r.l.u., corresponding to 2.57 Å. Noticeably, a small shoulder appears around $H = 1.08$ r.l.u., that is where the peak from the bulk Co is expected. Therefore, one can conclude that two crystalline phases with different periodicities are present with a stretched phase being dominant. Aiming to isolate these two contributions, we focussed on the Co peak and tried to fit the experimental data using two Gaussian functions. Our attempts, however, resulted into an unbalanced curve. A good agreement could be reached including a third contribution on the low-H side of the main peak. The three Gaussian functions, a linear background, and their sum are reported in Fig.4.7a. From the reciprocal space position of the Gaussian peaks b_{exp}^i , the real space lattice parameters of the three phases (a_{exp}^i , $i = 1, 2, 3$) were calculated. These three phases were used to represent three Co layers in the fitting of the XRR curve shown in Fig.4.7b. The fit was carried out assuming the three layers were stacked on the Ir surface starting from the most stretched, up to the completely "relaxed" phase. This choice assumes the gradual relaxation of the surface strains while going further from the Ir surface. The free parameters we considered were each layer thickness, roughness and density. Our first attempt found that the contribution of the bottom layer ("stretched" phase) was superfluous. Not only the roughness of the Ir substrate was exceeding the thickness of this layer, but we could also reach a good agreement with the data using only two Co phases. The values returning this successful fit are reported in Tab.4.4 and the good agreement is shown in Fig.4.7b.

The densities are indicated as δ and have to be interpreted upon comparison with the value for bulk Co: $\delta_{bulk} = 0.0091 \text{ at}/\text{\AA}^3$. The topmost layer, according to its density, corresponds to pure Co, while the underlying layer

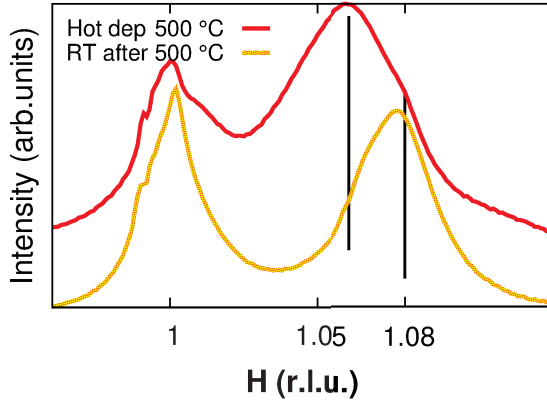


Figure 4.6: Intensity profile around the Ir (1,0) peak along the H direction. The red line refers to the film deposited on the hot Ir(111) substrate: the black lines are references for the main peak and the small shoulder. The orange line serves as a comparison with RT-deposited film, annealed at 500 °C.

has a slightly higher value of δ . This can be due to some Co-Ir intermixing, or to the Ir outcropping. We are not able to distinguish the two cases using XRR, as it is only sensitive to scattering length density (SLD) variations along the surface normal and, for a given depth, it can only probe average SLD values. However, we propend for the Ir outcropping, because our XAFS study suggests negligible Co-Ir alloying for annealing at $T \leq 600$ °C (see next section and [50]). Moreover, a columnar arrangement of Co given by the Ir outcropping [67] may explain the enhancement of the perpendicular magnetic anisotropy of the intercalated Co films [1]. This interpretation is also compatible with the GIXD data: the different phases identified in Fig.4.7a, represent the columns of Co formed by the Ir outcropping at the interface, an intermediate phase, and a topmost pure phase, in contact with the Gr. The most relaxed phase present in Fig.4.7a (blue curve) is likely related to the slight interface intermixing, which can be substituted in our fits by a large interface roughness value.

Beside the morphological question, our data prove the validity of the colander model to describe the action of the Gr layer during the Co intercalation. The Gr layer act on the Co flow towards the Ir surface, slowing it down. When the rate is sufficiently slow, the Co coordination is low enough to accommodate the surface strains by Ir outcropping (or Co-Ir intermixing).

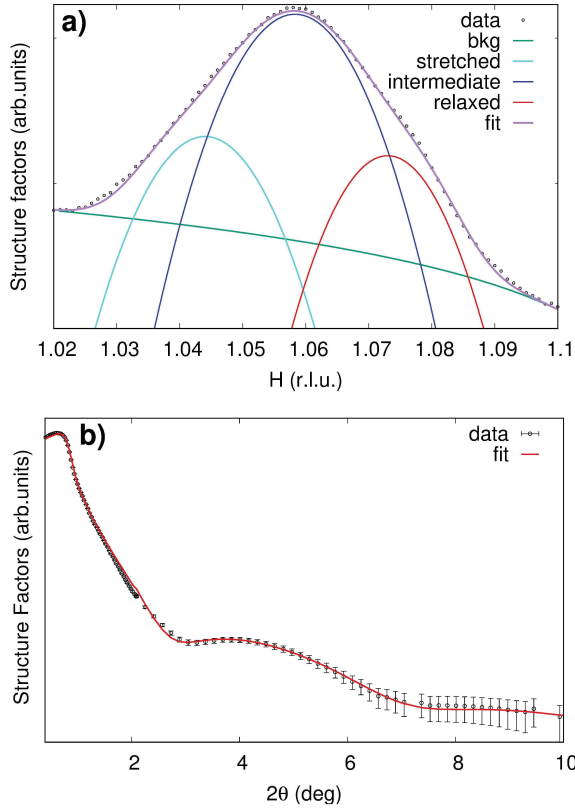


Figure 4.7: Logscale plots of **a)** Co peak region of the red line in Fig.4.6 (points) and fit (pink line) to experimental data involving three Gaussians: a contribution from the “relaxed” Co phase (red line), a major contribution for the “intermediate” phase (blue line), and a third contribution from the “stretched” Co phase (cyan line) lying at the Co-Ir interface. **b)** Reflectivity profile of the film (black points), and fit to data (red line) obtained with the parameters reported in Tab.4.4.

Layer		
Pure Co (top)	t	$6.1 \pm 0.4 \text{ \AA}$
	r	$1.0 \pm 0.1 \text{ \AA}$
	δ	$0.095 \pm 0.005 \text{ at./\AA}^3$
Intermediate Co	t	$6.2 \pm 0.1 \text{ \AA}$
	t^*	$5.0 \pm 0.2 \text{ \AA}$
	r	$0.9 \pm 0.5 \text{ \AA}$
	δ	$0.111 \pm 0.006 \text{ at./\AA}^3$
Ir substrate	r	2.1 ± 0.1

Table 4.4: Thickness (\AA), RMS roughness (\AA), and atomic density ($\text{atom}/\text{\AA}^3$) of each layer making up the best-fit model presented in Fig.4.7. Layers are presented from the topmost (pure Co) to the bottom (Ir substrate). In order to reliably compare this sample to the others, the effective thickness, t^* , is presented: it corresponds to the thickness one would observe if the Co was not stretched.

4.3 Co/Ir interface evolution upon thermal annealing

In order to study the interface effect from a local point of view, we decided to use XANES techniques, exploiting its chemical sensitivity and the local-scale, element-specific information it provides. Aiming to focus on the thermal effects, we studied a bare Co film upon repeated annealing.

4.3.1 Magnetic response dependence on the film's integrity

Two Co films were deposited on Ir(111) substrate at RT with the usual procedure. After the deposition, the samples were annealed for 5 min at $T_a = 300$ °C, to relax surface strains and to smooth the Co films while preserving their integrity [21]. At this temperature no Co-Ir alloy formation is observed for films thicker than 4 ML [22]. The final Co film thickness and the vertical distribution of the Co atoms in the sample were determined from the ratio of the Co_{2p} and the Ir_{4f} XPS peaks [51] measured at 40° of incidence with respect to the surface plane in order to minimize morphology artefacts [63].

The magnetic response of a first Co/Ir sample (film thickness $16 \pm 2 \text{Å}$, *i.e.* $\simeq 8 \pm 1$ ML) was characterized with a MOKE (magneto optical Kerr effect) magnetometer upon annealing under UHV conditions. The film thickness was above the critical value t_c at which the volume contribution (responsible for the in-plane anisotropy) overcomes the surface anisotropy originating the PMA, as explained in Sec.2.2. As expected, no magnetization was detected in the out-of-plane direction. The normalized hysteresis loops M/M_s were observed only in the longitudinal configuration and are shown in Fig.4.8a for the film after annealing at $T_a = 300, 500$ and 600 °C for 5 min each. Data demonstrate that the in-plane magnetic response of the film changes weakly until $T_a = 500$ °C. However, the treatment at $T_a = 600$ °C induces the broadening of the hysteresis loop providing the evidence of a magnetic domains rearrangement [68].

In order to probe the film integrity upon annealing we evaluated the vertical distribution of Co atoms by Angular Resolved XPS (AR-XPS) analysis (Fig.4.8b). The Co_{2p}/Ir_{4f} ratios calculated after $T_a = 300$ °C decrease when the exit angle is increased. This behaviour is typical for uniform thin films, where the XPS signal from the film is enhanced for lower angles (higher Co/Ir ratio) and suppressed at higher angles (lower Co/Ir ratio).

The annealing to 500 °C leads to the overall reduction of the Co_{2p}/Ir_{4f} intensity peak ratios. As this temperature is far below the Co melting point (around 1500 °C [69]), this suggests some reduction of the effective Co thickness, which is compatible with the increase of Co-Ir interface roughness.

The decrease of Co_{2p}/Ir_{4f} intensity peak ratios is much more pronounced after the 600 °C annealing. Furthermore, the angular dependence is weaker suggesting a more homogeneous distribution of Ir across the probed depth,

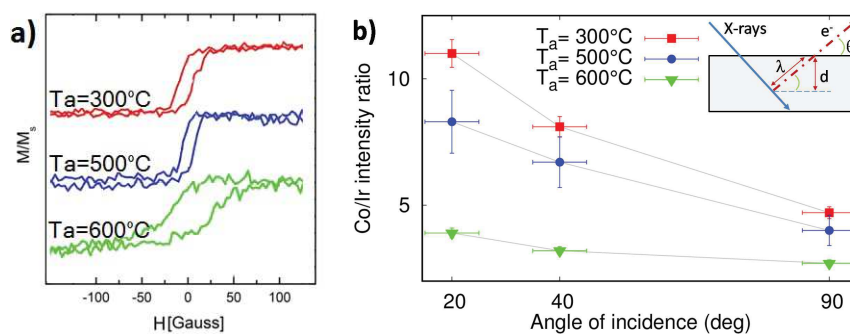


Figure 4.8: **a)** In-plane hysteresis loops measured by MOKE as a function of annealing temperature on 8 ML Co thin film. **b)** AR-XPS $\text{Co}_{2p}/\text{Ir}_{4f}$ intensity peak ratio as a function of annealing temperature on 8 ML Co thin film. **Inset:** the set-up used for the measurements: the probed depth d is shown together with the inelastic mean free path λ and the exit angle θ .

which is due to the more severe intermixing of Co and Ir.

4.3.2 Co atomic environment

The XPS characterization of the Co/Ir film demonstrates that the annealing induces macroscopic changes in the film structure, affecting its magnetic response. In order to further assess how the average local structure around Co atoms changes as a function of annealing, we carried Co-K edge XAS measurements.

A new Co thin film sample was deposited on an Ir(111) crystal surface following the same procedure described earlier: the thickness evaluated from XPS was $18 \pm 2 \text{ \AA}$ or $\simeq 9 \pm 1$ ML. The sharp LEED pattern in Fig.4.9a demonstrates the good crystalline quality of the Co thin film surface. The XPS spectra collected at 40° in the Co_{2p} and Ir_{4f} energy regions are shown by the solid lines in Fig.4.9b: the absence of any significant peak doubling, broadening or shifts ensures that no oxidation took place.

The Co/Ir sample was then transferred into an UHV mobile chamber specially designed for XAFS measurements at the BM23 beamline described in Sec.3.2.2. The chamber, whose base pressure was better than 10^{-8} mbar, was equipped with a heater stage for sample annealing and two perpendicular Be windows ($500 \mu\text{m}$ thickness) for incoming x-ray beam and outgoing fluorescence intensity collection (Fig. 4.9c). The sample was oriented in such way that the linear polarization of the incoming beam was nearly perpendicular (80°) to the sample surface. In this geometry, the XAFS is mainly sensitive to structural features perpendicular to the film plane [70]. Co K edge XAS data were acquired in fluorescence geometry. The incident x-ray flux I_0 , was measured using gas filled ionization chambers and the fluorescence yield was

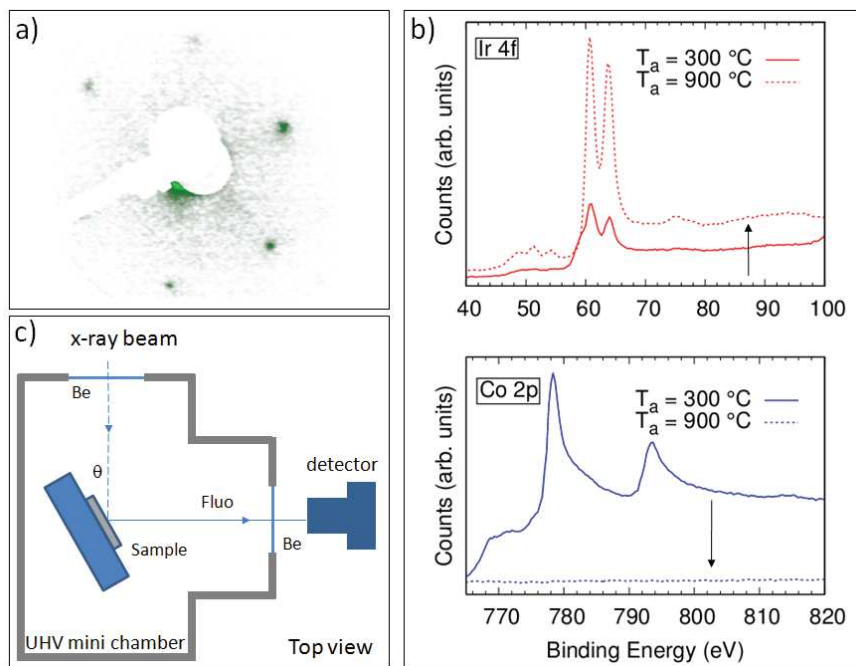


Figure 4.9: **a)** LEED pattern of the 9 ML Co film after 300 °C annealing. **b)** XPS of Co_{2p} and Ir_{4f} peaks collected on the 300 °C annealed film (solid lines) and after repeated annealing cycles up to 900 °C (dashed lines): the Co_{2p} intensity is completely suppressed while Ir_{4f} raises (arrows). **c)** Schematic view of the XAS data collection geometry at BM23, ESRF.

measured using a single-element energy resolution detector placed about 10 cm away from the sample. The Co K_α fluorescence signal I_f , was selected using the multi-channel analyzer (MCA) electronics. The live time of the detector was kept higher than 90% to suppress the non linearity effects. The absorption signal was calculated as the ratio $\mu(E) = I_f/I_0$.

In order to reveal the structural modification around Co atoms, the sample was annealed at $T_a=500, 600, 700, 800$ and 900 °C, for 5 min at each temperature. Ten Co K-edge spectra were collected in the near edge region on the relaxed film ($T_a=300$ °C) and after each annealing cycle. In order to remove the Bragg peaks from the Ir substrate, the sample was slightly tilted (within $\simeq 2^\circ$) after each spectrum. This resulted into a shift of the Bragg peaks along the spectra so they could be easily identified and removed [71].

After the XAS measurements the sample was moved back under UHV conditions into the preparation laboratory at ID03 and further XPS measurements were carried out to probe the thin film status. The Ir_{4f} signal in Fig. 4.9b, dashed lines shows higher intensity while the Co_{2p} XPS signal cannot be distinguished from the background noise. This finding cannot be explained by the Co evaporation because the overall Co K edge jump discontinuity is only slightly reduced ($\simeq 10 \div 15\%$) after annealing. Instead, XAS and XPS data can be coherently interpreted as a complete Co film dissolution and formation of Ir rich surface layer after $T_a=900$ °C. Co photoelectrons cannot escape the sample but their fluorescence signal is detected. Therefore Co atoms must be buried under an Ir layer thicker than the inelastic mean free path of Co photoelectrons ($\simeq 10$ Å) but thin enough to not suppress the Co K_α fluorescence detection (the transmission coefficient for a 0.1 μm -thick Ir layer is higher than 90%).

The Co K edge XAS spectra were averaged and normalized using standard procedures for X-ray absorption fine structure data treatment [72, 70] and are shown in Fig.4.10A. The spectra show gradual modifications as a function of the annealing temperature, characterized by a progressive shift of the main spectral features. Noticeably, these changes are relatively weak until $T_a=600$ °C, but interestingly at this temperature XPS data demonstrate a consistent increase in the Co/Ir interface roughness related to modifications of the magnetic response observed by the MOKE measurements (see Fig.4.8).

Raising the annealing temperature above $T_a=600$ °C causes the XANES spectra of the Co film progressively evolve, signaling changes of the average local atomic structure around the absorbing atoms. In order to understand the structural evolution taking place around the Co atoms, we first compare the experimental spectra of the film to that of bulk Co phase.

Co K edge XANES spectrum of a Co metal foil (black solid line in Fig.4.10C) is characterized by a typical double peak at the edge (a and a') and a shoulder at the edge onset (b). To achieve a reliable interpretation the origin of these features, we calculated theoretical XANES using the full multiple scattering

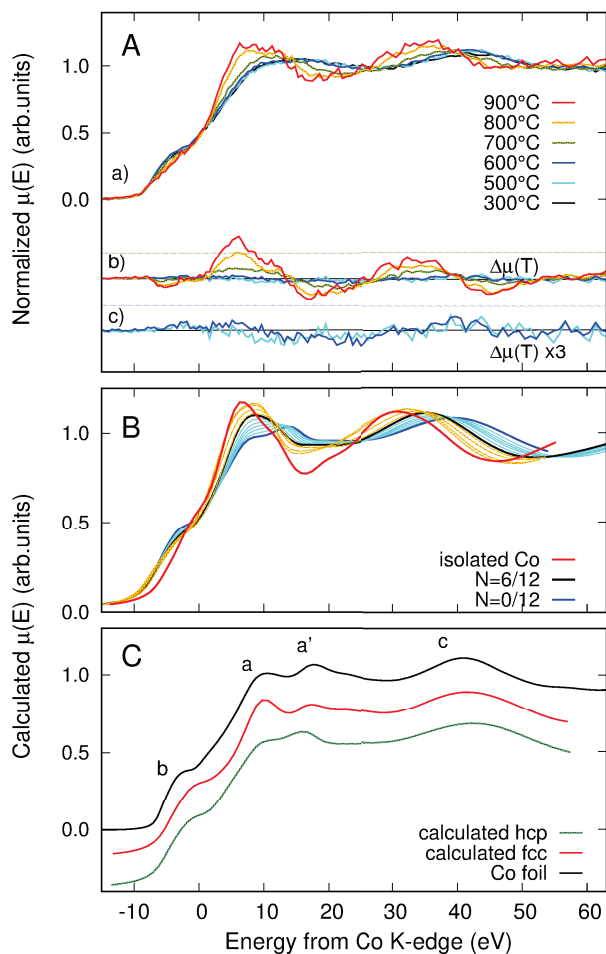


Figure 4.10: **A**) Co-K edge normalized XANES spectra of 9 ML Co/Ir(111) film after subsequent annealing cycles. The differences $\Delta\mu(T_a) = \mu(T_a) - \mu(300^\circ\text{C})$ between the data collected after annealing at T_a and relaxed (300°C) film are also presented (downshifted for clarity). The $\Delta\mu(500^\circ\text{C})$ and $\Delta\mu(600^\circ\text{C})$ data were multiplied by 3 to highlight the weak effects. **B**) Theoretical XANES curves calculated for a pure Co hcp structure ($N = 0$, blue line), $\text{Co}_{0.5}\text{Ir}_{0.5}$ alloy ($N = 6$, black line) and an isolated Co atom embedded in an Ir structure (red line). $\text{Co}_x\text{Ir}_{1-x}$ alloys representing intermediate concentration of Co-rich (cyan) and Ir-rich alloys (orange lines) are also reported. **C**) The experimental XANES spectra measured on Co metal foil (black) theoretical curves calculated for hcp (green dotted) and fcc (red dotted) atomic models (shifted for clarity).

approach implemented in the FEFF8 software package [73]. As a first step we simulated the Co-bulk XANES spectrum starting from literature data [74] and we optimized the parameters of the simulation. Self consistent exchange and correlation potentials were modelled using complex Hedin-Lundqvist potentials [75] in the muffin-tin approximation using the default muffin-tin radius. Self consistency was calculated in a 3 Å cluster radius around the absorber, whereas full multiple scattering was extended to a 6 Å radius atomic cluster around the absorber. An imaginary part (1 eV) was added to the exchange potential to take into account the experimental resolution and core-hole broadening. The same parameters were applied to model the XANES spectra of fcc and hcp Co and the results are shown by the dashed lines in Fig.4.10C.

Comparing the XANES features of the Co foil to these calculations of fcc and hcp Co structures, there are evident differences pointing to the hcp nature of the foil and, therefore, we are able to distinguish between fcc and hcp structures in our measurements. Noticeably, the data collected from the relaxed Co/Ir film (Fig.4.10A) depict structural features relatively smooth compared to those of bulk Co (Fig.4.10C). This effect is likely due to the finite size of the film which results into a large fraction of under-coordinated sites and/or in a more distorted environment with respect to the bulk.

On the basis of the above considerations, we used the hcp structure of pure Co as the starting point for a quantitative XANES interpretation of the results. Several atomic cluster models were built replacing, one by one, the 12 nearest Co atoms around the absorber with Ir atoms and considering all the not equivalent dispositions of Co sites. For each composition all the spectra resulting from non equivalent Ir configurations were averaged up taking into consideration their multiplicity. We used the Vegard's model [76] to account for the lattice expansion due to the increasing Ir concentration: assuming a linear behavior of the lattice parameter between pure Co ($a_{Co} = 2.51$ Å) and pure Ir ($a_{Ir} = 2.72$ Å), for a Co_xIr_{1-x} model we stretched the structure by $x(a_{Ir} - a_{Co})$ with respect to the pure Cobalt. Moreover, in order to model the diffusion of a single Co atom into the Ir matrix, we considered also the case of an isolated a Co atom at the center of an Ir cluster. These models are approximations which could be improved by taking into account additional neighboring shells. However bearing in mind the intrinsic limitations of the XANES theory ² and the difficulties to account for all the possible parameters to shape the atomic cluster models, these models can be considered a satisfactory and reliable description of the Co atomic environment in these

²The time required for a single XANES calculation is around $t = 30$ min on an *Intel Core i5* processor, we found that the major effect on the XANES features arises from the composition of the nearest neighbors shell, therefore we did not change the composition of the next neighbour shells. This is a crude approximation but the good agreement of these models with experimental findings is already satisfactory, whereas taking into account next neighbour shells would result in a huge increase of the computational time due to the many configurations to be considered.

films.

The calculated spectra for the model structures are presented in fig.4.10B. Comparing the simulations to the experimental spectra, the similar trends are evident: the theoretical curves match the decrease of the edge shoulder (label *b* in Fig.4.10C) and the progressive shift of the *a-a'* and *c* features to lower energies in experimental data. Interestingly, both in the experimental data and in the theoretical curves, the *a* and *a'* peaks merge and their relative intensities are reversed upon increasing the annealing temperature. The trends observed for theoretical and experimental curves allow us to reliably explain the evolution of the experimental spectra as resulting from gradual modification of the Co local structure toward Ir-rich Co-Ir phases.

To understand more quantitatively the system evolution as a function of annealing we simplified the problem and reproduced the absorption spectra measured for intermediate annealing temperature, as a linear combination of $\mu(300\text{ }^\circ\text{C})$ and $\mu(900\text{ }^\circ\text{C})$. This approach, also known as linear combination analysis (LCA), relies on the hypothesis that the Co structure is not homogeneous but consists of coexisting phases. In particular, we considered a pure Co phase (represented by $\mu(300\text{ }^\circ\text{C})$) and an Ir-rich phase ($\mu(900\text{ }^\circ\text{C})$). Such phase separation, also observed in our previous experiments [21], is a reasonable assumption due to the short annealing times where the system cannot reach thermodynamic equilibrium. As an example, we show the fit of $\mu(700\text{ }^\circ\text{C})$ in Fig.4.11A (similar agreement is obtained also for the other spectra).

Furthermore, assuming that the pure Co phase is absent in $\mu(900\text{ }^\circ\text{C})$ (see below), we can use the best-fit coefficient of $\mu(300\text{ }^\circ\text{C})$ in LCA to evaluate the relative amount of pure Co as a function of T_a . The results, shown in Fig.4.12, demonstrate that the Co phase is largely unaffected by annealing until $T_a=500\text{ }^\circ\text{C}$. After $T_a=600\text{ }^\circ\text{C}$, the pure Co phase fraction starts decreasing while the Ir-rich phases increase: this trend proceeds rapidly after $T_a=700\text{ }^\circ\text{C}$.

To better understand Co atoms environment upon annealing, we applied the same LCA approach to the analysis of the $\mu(900\text{ }^\circ\text{C})$ spectrum, where the system is close to the thermodynamic equilibrium, using the theoretical simulations of Fig.4.10B) as contribution to the combination. This allowed us to get more insight about the composition of Co phases. In particular, after combining theoretical XANES having different Ir content ($N=0, 1, \dots, 12$ and isolated Co in Fig.4.10B), we found that the best agreement (minimum χ^2) is for the pair involving an alloyed/intermixed nearly stoichiometric CoIr phase ($N=5,6,7$) and isolated Co in Ir. Due to the above mentioned intrinsic limitations of XANES models, we are unable to distinguish the exact stoichiometry, however we can safely assume a nearly-50% stoichiometry in the following discussion.

In order to check for possible oxygen contamination we also tried to include Co-oxide contributions to the LCA analysis but the agreement did not improve. Therefore we can exclude this contribution.

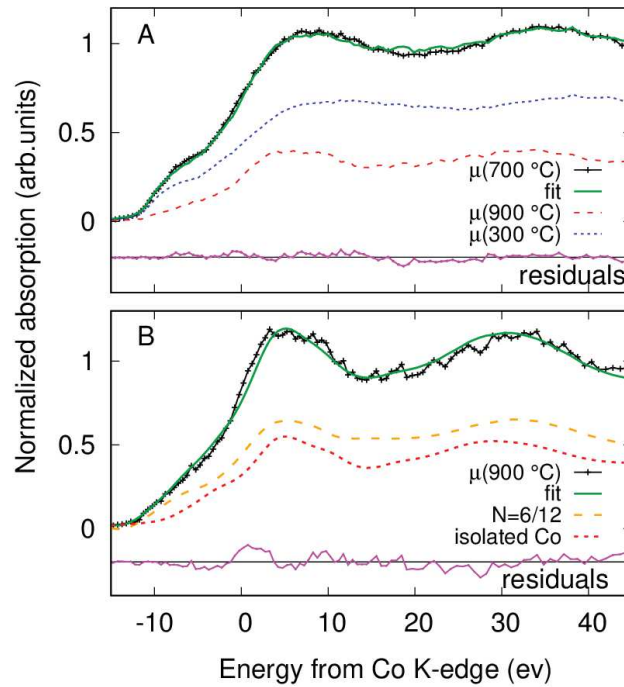


Figure 4.11: **A**) LCA best fit of $\mu(700\text{ }^\circ\text{C})$ experimental spectrum (black line) fitted (green line) to a linear combination of $\mu(900\text{ }^\circ\text{C})$ (red dashed line) and $\mu(300\text{ }^\circ\text{C})$ (blue dotted line) experimental spectra. **B**) LCA best fit for $\mu(900\text{ }^\circ\text{C})$ spectrum (black line) fitted (green line) as a linear combination of $\text{Co}_{0.5}\text{Ir}_{0.5}$ alloy (orange dashed line) and isolated Co (red dotted line) spectra. The contribution of a pure Co phase (not shown) was taken into account by including either $\mu(300\text{ }^\circ\text{C})$ experimental spectra or the hcp calculation presented in the former section. In both cases, the combination coefficient resulted to be 0. Residuals (experimental data minus best fit) are shown by magenta lines, vertically shifted for sake of clarity.

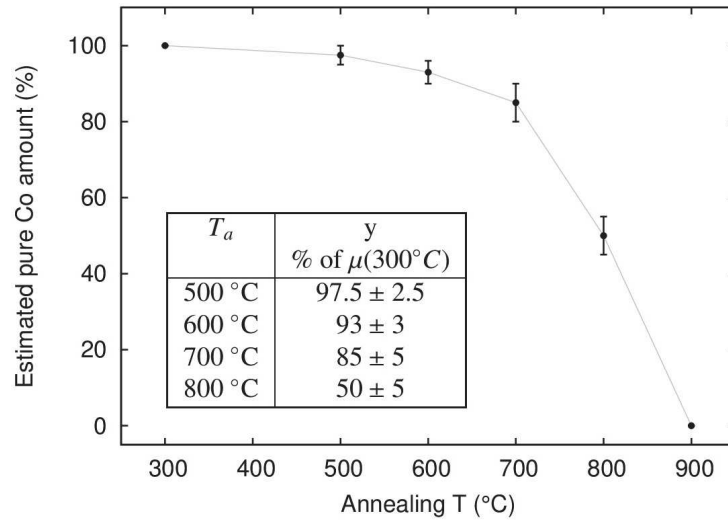


Figure 4.12: Amount of pure Co in the sample estimated from the LCA coefficient of the $\mu(300^\circ\text{C})$ contribution. **Inset:** Coefficient of LCA analysis, the experimental $mu(T_a)$ spectrum is fitted to the theoretical curve: $y \mu(300^\circ\text{C}) + (1 - y) \mu(900^\circ\text{C})$ refining y .

Noticeably, both LCA analyses shows a very low pure Co content after annealing to 900 °C (less than 10%). This confirms our hypothesis of nearly complete film disintegration and suggests a bimodal distribution of Co: alloyed with Ir in a roughly stoichiometric phase or as isolated atoms into the Ir matrix.

Discussion

Both XPS and XANES data confirm the intermixing of Co and Ir but depict apparently different behaviors.

XPS data demonstrate that a 600 °C annealing roughens the interface resulting into a homogeneous distribution of Co and Ir in the whole probed depth. On the contrary, XAS spectra show a progressive evolution of Co local structure toward Ir richer phases whose trend is relatively weak up to $T_a=600^\circ\text{C}$. Moreover the XPS Co_{2p} signal is negligible on the $T_a=900^\circ\text{C}$ film while XAS demonstrate negligible Co evaporation (similar edge intensities) and the formation of Ir rich phases.

In order to understand this apparent contrast we must stress that XPS is probing the sample composition close to the surface (few nanometers in depth) averaged on a length scale of few millimetres, being the size of x-ray beam on the sample. In contrast, XAS selectively probes the average local structure around Co atoms up to several micrometers depth. Therefore XAS and XPS findings can be coherently understood assuming that the annealing firstly causes the roughening of the Co-Ir interface even at mild temperatures

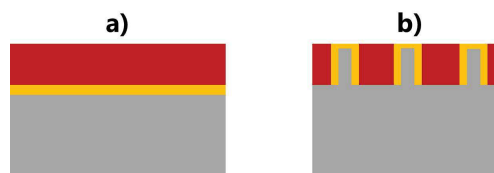


Figure 4.13: Two possible models representing the structural evolution of the sample upon annealing. **a)** Homogeneous Co film (red) on a regular alloyed layer (orange) on the Ir(111) substrate (grey). **b)** Pillars of Ir protruding from the substrate are breaking the Co film integrity. The interface regions give rise to alloyed regions.

$T_a \leq 500$ °C. Around $T_a = 600$ °C the Ir starts to protrude to the Co film compromising its integrity and making the $\text{Co}_{2p}/\text{Ir}_{4f}$ intensity ratio measured by AR-XPS nearly constant throughout the probed angular range. Due to the low Co fraction in the Ir phases, XAS is blind to this phenomenon. Nevertheless, raising the annealing temperature causes the interdiffusion of Co into the substrate together with the formation of phases richer in Ir. This is clearly detected by XAS measurements.

This process could be driven by the mixing entropy like it was proposed for Co/Pt systems [77]. However, if this was the case, we would expect the formation of a homogeneous alloy layer at the Co-Ir interface, as represented schematically in Fig.4.13a. This occurs only until $T_a < 600$ °C, where the formation of a nearly stoichiometric alloy minimizes the strain at the interface due to its intermediate lattice parameter between pure Ir and Co. For $T_a \geq 600$ °C, the loss of angular dependence of the XPS intensity ratios (Fig.4.8b) proves the homogeneous distribution of Co and Ir along the vertical direction, supporting the Co diffusion towards deeper regions of the substrate, probably due to the surface tension minimization, and the Ir protrusion to the film surface. The resulting lattice mismatch can break the film into smaller clusters, maybe separated by Ir protrusions, and intermixed regions (see Fig.4.13b). Finally, the in-plane integrity loss, inducing modifications to the magneto-crystalline anisotropy of the film, is most likely related to the modified magnetic response detected by MOKE measurements.

In previous measurements (Sec.4.1 and [21]), GIXD on two Co films (a bare and a Gr-covered Co film) showed that an intermixed layer was found only for the intercalated film upon annealing at 500 °C. The present results, obtained combining XAS, XPS, and MOKE, demonstrate that the intermixing is favoured by the breaking of the film continuity. Such effect is provided by surface strains or, in the intercalated films, by the presence of Gr. Moreover we believe that the high thickness increases the stability of the film disfavoring the interdiffusion process: this interpretation is also supported by the observations made on Pt/Cu(100) systems [78].

Conclusions

We have characterized the structural and magnetic evolution of Co thin films above the critical thickness t_c marking the in-plane to out-of-plane magnetization transition. Combining *in-situ* complementary techniques we were able to describe the diffusion process causing the loss of Co film integrity which is then linked to the magnetic behaviour.

AR-XPS and MOKE observations show that the films are homogeneous after annealing at 300 °C and present an in-plane magnetization. As coherently demonstrated by XPS and XANES, further annealing to 500 °C results into a higher roughness at the Co/Ir interface which does not affect the magnetic properties. The 600 °C treatment breaks the in-plane integrity of the Co film affecting its magnetic response through a rearrangement of the magnetic domains. XANES modifications interpreted with LCA, show that a significant amount of CoIr alloy is formed upon annealing to 700 °C. The alloying progresses during the 800 and 900 °C thermal treatments. Eventually, the absence of Co_{2p} signal after $T_a = 900$ °C demonstrates the diffusion of Co further than 1 nm from the surface.

This analysis demonstrates the structural breakdown of the Co film upon thermal annealing, the lattice rearrangement driven by the surface strains relaxation, and the consequent modification of the Co magnetic response. The interdiffusion of Co and Ir is found to be activated at high temperatures, giving rise to Ir-rich phases. A thermally induced, homogeneous Co-Ir intermixing occurring at the interface and gradually swallowing the Co film can be excluded.

4.4 Capping efficiency and origin of the enhanced PMA

Introduction

The following experiments address two main points: an important applicative issue, and an aspect of fundamental knowledge about the structural description of the intercalated Co films.

First of all, the Gr efficiency in the oxidation prevention will be addressed. In facts, the effective protection provided by Gr is of fundamental importance for applicative purposes, and yet it has never been investigated. To approach this issue we present polarized-XANES measurements carried out on intercalated Co films exposed for few minutes at ambient pressure. The experimental procedure, described in details in the following paragraphs, allowed us to probe the Co oxidation.

Furthermore, from the EXAFS region of the same measurements we were able to gain information on the microstructural strain acting on the interca-

lated Co films. This strain was found to be thickness dependent: in particular, it affected only intercalated Co films below t_c , proving an existing relation with the PMA.

Experimental details

Two Ir(111) substrates were prepared under UHV using the usual procedure at the ID03 preparation laboratory. The surface quality was inspected by XPS, and LEED (whose patterns are reported in Fig.4.14a). After Gr was grown at 600 °C, XPS and LEED were carried out again. The blurred, incomplete rings around the Ir spots in the LEED pattern in Fig.4.14b are a sign of defective Gr on the surface, as expected from a process growth at these temperatures.

After the Co deposition at RT, XPS and LEED measurements were repeated. The ratio of Co_{2p}/Ir_{4f} XPS peaks, collected with an exit angle of 45° to minimize morphology effects [63], gave a films thickness of 10 ± 1 ML and 5 ± 1 ML. In the following we will refer to the former as the *thick film* and to the latter as the *thin film*. The blurred spots in the LEED patterns (Fig.4.14c) are due the poor regularity of the Co film, in agreement with the granular growth observed by STM (see Sec.4.1 and [21]).

The films were then intercalated between the Gr layer and the Ir(111) at $T = 300$ °C for 5 min. The decrease observed in the XPS Co $2p$ peaks in Fig.4.14, combined with the increase of the C $1s$ peak are interpreted as a sign of the effective intercalation. Furthermore, the higher blurriness of LEED in Fig.4.14d) is a sign of the increased disorder at the surface.

After the intercalation, each sample was transferred under ambient pressure to the BM23 beamline where it was loaded into a vacuum chamber with a base pressure $P \simeq 10^{-5} mbar$. Co K-edge XAS spectra were collected in fluorescence yield both in the near edge (XANES) and in the extended (EXAFS) regions using a Ge 13-elements detector placed at about 3 cm from the sample surface (Fig.4.15).

The incident x-ray flux I_0 , was measured using gas filled ionization chambers. Data acquisition was carried out keeping the X-ray linear polarization closely perpendicular (80°) and parallel (10°) to the sample surface in order to maximize the XAFS sensitivity to structural features being either perpendicular or parallel to the film plane [2]. The Co K_α fluorescence signal I_f^i of each element, was selected using the MCA electronics. The live time of the detector was kept higher than 90% to keep negligible the nonlinearity effects. The total absorption signal was calculated as the ratio $\mu(E) = I_f^T/I_0$, with I_f^T being the sum of the single intensities collected by each element. For each sample orientation, several spectra were collected tilting the specimen by $\simeq 0.2^\circ$ between two consecutive scans: this resulted in an energy shift of the Ir Bragg peaks

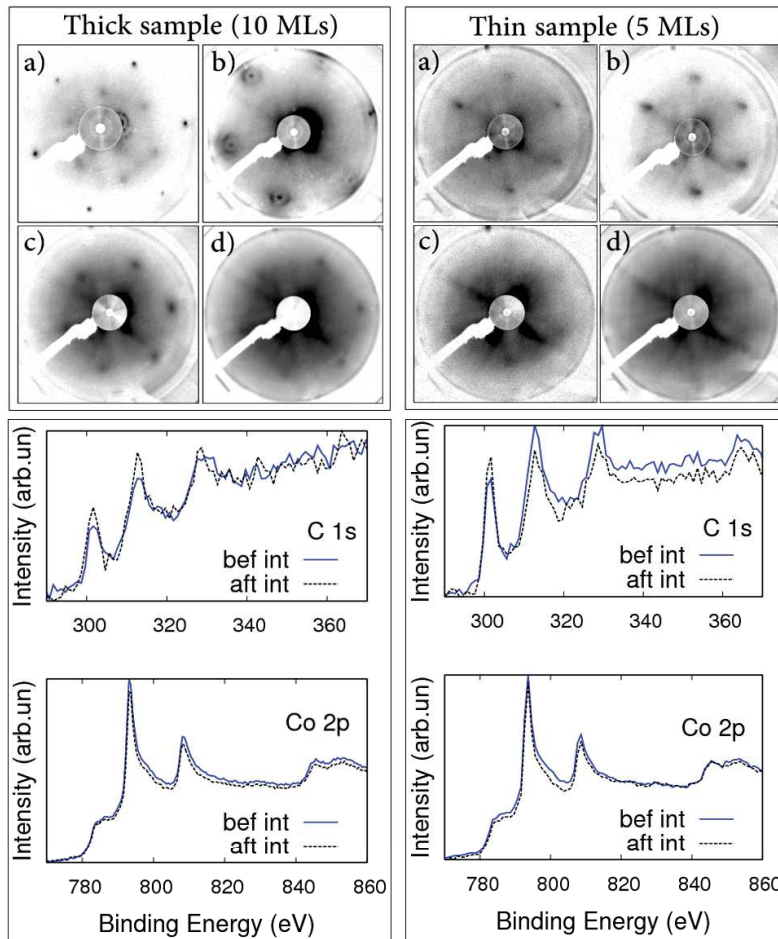


Figure 4.14: Thick film sample - **TOP:** LEED patterns acquired for the thick sample **left** and for the thin sample **right**. *a* clean Ir surface, *b* pristine Gr, *c* Co film as deposited and *d* upon annealing at 300 °C. **BOTTOM:** XPS of the thick **left** and thin sample **right**. The blue filled line were acquired on the pristine Co film, the black dashed line refer to the sample after the intercalation.

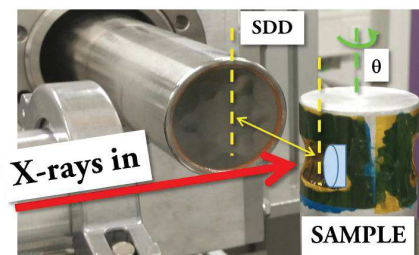


Figure 4.15: Experimental setup used for XAFS measurements at the BM23 beam-line, ESRF. The sample was placed in a vacuum chamber with Kapton windows with its surface vertical. The chamber was mounted on a rotating support allowing to vary the angle between the incoming beam and the sample surface. The detector was placed at 90° with respect to the X-ray beam and the sample to detector distance (SDD) was $\simeq 1$ cm during the measurements.

which could be easily identified and removed from each spectrum acquired by the single elements of the detector. The XAS spectra were then averaged and normalized using standard procedures for X-ray absorption fine structure data treatment [79, 80, 73].

Once the characterization of the intercalated films was completed ($\mu_{\perp}^{bef}(E)$ and $\mu_{\parallel}^{bef}(E)$), the samples were annealed for 5 min at 500°C . After cooling down to room temperature, samples were brought back to ambient pressure and loaded back into the vacuum chamber. Then, new spectra were collected using the same procedure: $\mu_{\perp}^{aft}(E)$, $\mu_{\parallel}^{aft}(E)$.

All the normalized spectra are presented in the near edge (extended) region for the thick and thin samples in fig.4.18 (4.21) and 4.20 (4.22), respectively.

In order to provide a reliable interpretation, we carried out a reference measurement on a standard Co foil $\mu_{ref}(E)$. The results are presented by the black, full line in Fig.4.16.

Noticeably, a good agreement in terms of the position and the relative intensities of the main experimental spectral features (labelled a , a' , b , c) is found between our hcp Co model and $\mu_{ref}(E)$.

4.4.1 Oxidation prevention

The first spectrum was collected on the thick film with the beam polarization lying along the film plane $\mu_{\parallel}^{bef}(E)$. The near edge region of the spectrum is presented by the black points in Fig.4.17: noticeably it presents a broad white line α , a small pre-edge shoulder β and a smeared oscillation γ around 45 eV. These features are not directly compatible with the pure Co hcp, which conversely shows a doublet a - a' , a better defined pre-edge shoulder b and the stronger c oscillation (brown line). Nevertheless, since the film was kept under ambient pressure, it is reasonable to assume the formation of some Co oxide.

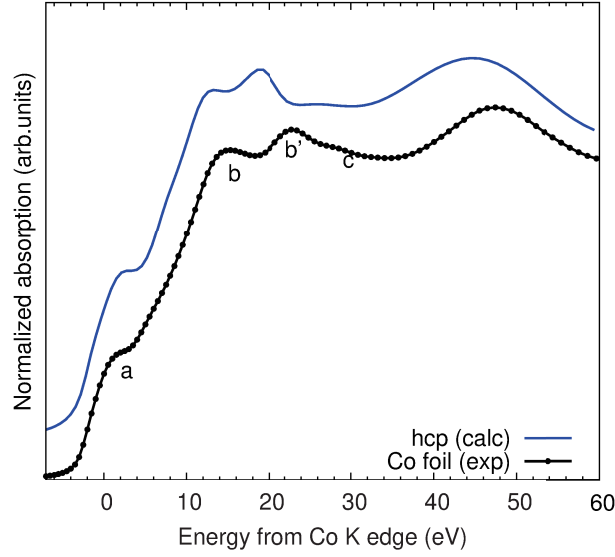


Figure 4.16: XAS of the Co foil reference structure (black points) and theoretical calculation of pure Co hcp (blue line).

The oxidised phase CoO presents an extremely intense A white line while no peaks are observed in the pre-edge and in the region around 45 eV. The combination of these features with those of the hcp Co, can reproduce quite well the collected spectra $\mu_{\parallel}^{bef}(E)$: the white line would be strongly affected by the massive A peak shadowing the a - a' doublet, while the β and γ features can be obtained from the “original” b and c peaks plus the antiphase contribution of CoO. The LCA analysis performed combining these two contribution is reported in Fig.4.17b and matches relatively well the experimental data suggesting a contribution of about $25\pm 5\%$ from the CoO phase. Differences between the LCA and the data can be ascribed to a highly defective CoO phase and to a generally disordered film.

After the acquisition of $\mu_{\parallel}^{bef}(E)$, the data collection was repeated with the polarization vector oriented perpendicular to the film plane: $\mu_{\perp}^{bef}(E)$. The perfect superposition of the $\mu_{\parallel}^{bef}(E)$ and $\mu_{\perp}^{bef}(E)$ signals (top curves in Fig.4.18a) points out an isotropic behaviour for this thick film.

After keeping the sample for 5 min at 500 °C, both the measurements were repeated. In the near edge region, $\mu_{\perp}^{aft}(E)$ and $\mu_{\parallel}^{aft}(E)$ (bottom curves in Fig.4.18a) present different lineshapes: around 15 eV a single broad feature is observed for $\mu_{\perp}^{aft}(E)$, while a broad double peak can be distinguished in $\mu_{\parallel}^{aft}(E)$. Moreover a slightly higher oscillation amplitude is found for $\mu_{\parallel}^{aft}(E)$. These effect are most likely due to termination effects: in the perpendicular

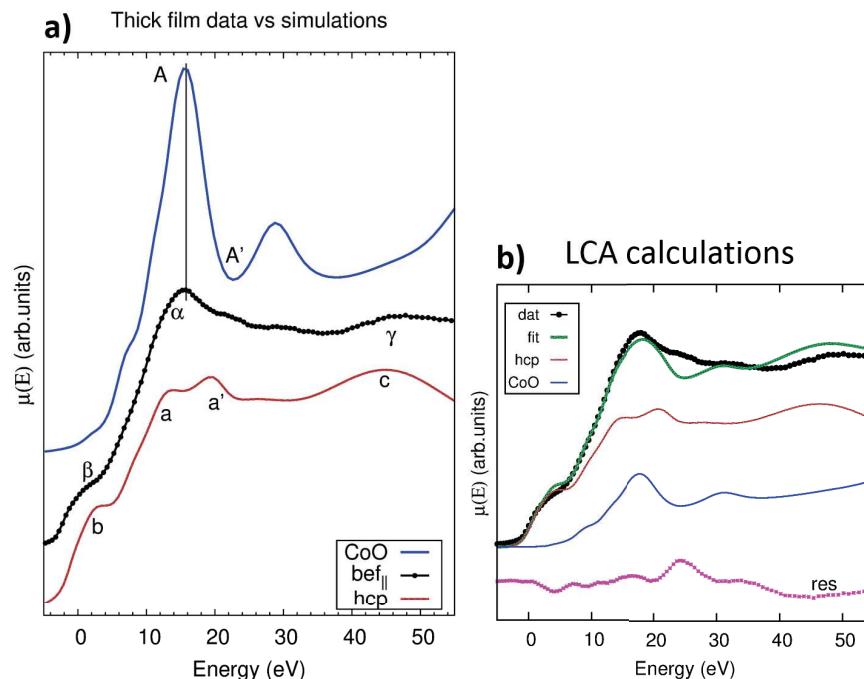


Figure 4.17: Experimental XANES of film B (black circles) compared to *Ab-initio* simulations of pur Co hcp (brown), and *CoO* (blue) theoretical curves. Spectra have been shifted for clarity.

direction, the relative amount of Co atoms lying near the borders of the Co layer is high, therefore these Co absorbers are under-coordinated and cannot generate the a , a' doublet. To verify this hypothesis, we compare the hcp simulation of Fig.4.17, with the ones obtained using smaller anisotropic clusters simulating the termination effects on the film. The theoretical curve we obtained, solid lines in Fig.4.19, show the case of the small cluster probed by a light beam polarized parallel to the terminated film (green line), and by an unpolarized light beam (black line). The first detail that comes to the eye when comparing the effects due to the size of the cluster (dashed line to solid lines), is a definite smearing of the XANES features. Moreover, if we consider the effect of polarization, we notice that the effect is weaker for an in-plane polarized beam being mostly sensitive in the film plane, that is where the termination effects are smaller.

In order to highlight the modifications due to the annealing, the four $\mu(E)$ are reported in Fig.4.18b where the data collected with the same polarization geometry have been superimposed. The features due to the oxide presence are significantly suppressed by the annealing: the white lines of the $\mu^{aft}(E)$ are more similar to the theoretical hcp Co structure, their pre-edge has risen and the amplitude of their oscillation around 45 eV have been restored. LCA

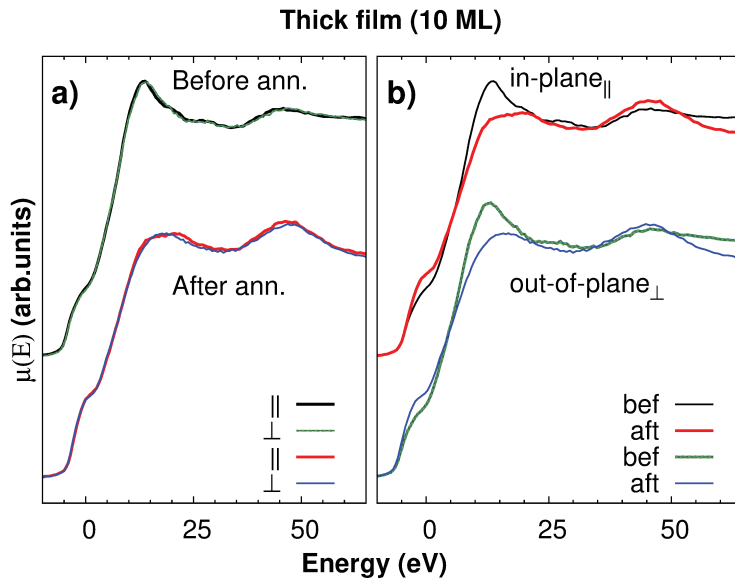


Figure 4.18: **a)** XANES of the thick film collected for the thick film as intercalated with in-plane (black line) and out-of-plane (green line) polarization, and for the annealed film with in-plane (red line) and out-of-plane (blue) geometries. **a)** Data are reported to highlight the comparison of the different polarizations. **b)** The same spectra presented in *a)* are shown to facilitate the identification of the annealing effects. **b)** LCA analysis of the $\mu_{\perp}^{bef}(E)$ spectrum (black points). Two contribution were considered: a CoO phase (blue line) and the pure Co hcp (brown line). The best fit (green line) gives a $25 \pm 5\%$ contribution from CoO.

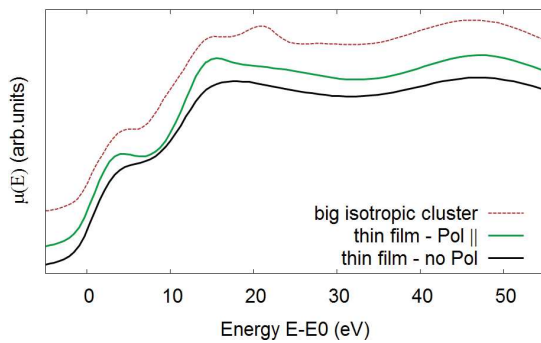


Figure 4.19: Theoretical spectra of an hcp big cluster (brown dashed line) and of two smaller, anisotropic clusters representing the thin film (solid lines): the calculations were run for in-plane polarization (green line) and unpolarized beam (black line). The latter configuration represents the case in which such small clusters are randomly oriented on the surface and their effect gives the same result one would have using unpolarized light.

calculations, compatibly with these observations, estimated an oxide concentration $\simeq 10\%$.

As for the thick film, the thin one was measured right after the Co intercalation with both the polarization geometries: $\mu_{\perp}^{bef}(E)$ and $\mu_{\parallel}^{bef}(E)$. The XANES spectra are reported in Fig.4.20a.

Contrarily to the thick film case, the presence of the oxide in the thin film is not evident from the XANES data. However it becomes visible by comparing $\mu_{\parallel}^{bef}(E)$ and $\mu_{\parallel}^{aft}(E)$, as proved by Fig.4.20b: the rise of the pre-edge peak, the decrease of the white line and the restoration of the oscillation amplitude and frequency around 45 eV, as discussed for the previous sample, are an evidence of the decreasing oxide amount. In particular, the LCA analysis estimates a relative amount of CoO around the 10% before the annealing, and $< 5\%$ afterwards.

The minor amount of CoO makes the two signals $\mu_{\perp}^{bef}(E)$ and $\mu_{\parallel}^{bef}(E)$ distinguishable already before the annealing. The main difference, enhanced upon annealing, is the single feature presented by the $\mu_{\perp}(E)$ spectra with respect to the double peak emerging in the $\mu_{\parallel}(E)$. Also, the γ peak of $\mu_{\parallel}(E)$ is found to be shifted towards lower energies and to have a stronger amplitude compared to $\mu_{\perp}(E)$. As for the thick film, these effects are ascribed to the low thickness causing a higher Co coordination along the film plane (compare Fig.4.19).

Microstructural strain and anisotropy

The extended region of the spectra collected on the thick film (and their Fourier transform) are presented in Fig.4.21a (4.21b): as in the XANES region, the two datasets present the same features both in k and in R -space, with a nearly perfect superposition. The slightly smaller intensity of the perpendicular signal in Fig.4.21b can be ascribed to termination effects.

The spectra collected after keeping the sample for 5 min at 500 °C are reported in Fig.4.21c,d. Just like it was found for the spectra collected before annealing, the two curves match with each other both in k - and in R -space.

Quantitative information about the first shell in-plane and out-of-plane atomic distribution about the average Co site was obtained by fitting the k^2 weighted data over the range $3 < k < 11 \text{ \AA}^{-1}$, including the first four shells around the absorber. The scattering factors were obtained using the FEFF8 code [30] whereas the average bond lengths $R_{\perp, \parallel}$ and the Debye-Waller factors $\sigma_{\parallel, \perp}^2$ were extracted from the fits. The parameters giving the best results in terms of χ^2 are presented in Tab.4.5a.

The intercalated film $\mu^{bef}(E)$ presents interatomic distances compatible with the values of bulk Co (2.507 Å [81]) with a small compression in the

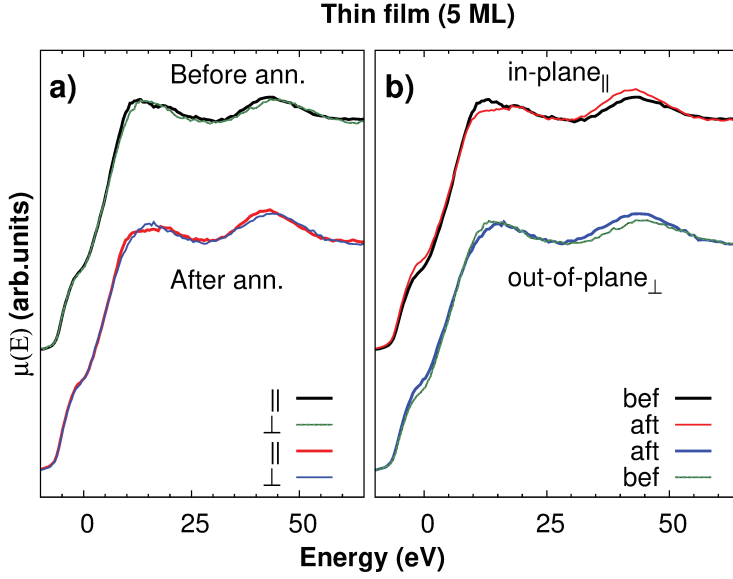


Figure 4.20: **a)** XANES of the thin film are reported superimposing the two different polarization before (top) and after (bottom) the heating treatment. **b)** The same data are presented according to their polarization direction: top curves show the in-plane spectra while the out-of-plane is at the bottom.

a)	Thick film			
	R_{\parallel} (Å)	σ_{\parallel}^2 (Å ²)	R_{\perp} (Å)	σ_{\perp}^2 (Å ²)
$\mu^{bef}(E)$	2.504(6)	0.0074(7)	2.498(6)	0.0075(7)
$\mu^{aft}(E)$	2.504(5)	0.0056(5)	2.502(5)	0.0055(6)

b)	Thin film			
	R_{\parallel} (Å)	σ_{\parallel}^2 (Å ²)	R_{\perp} (Å)	σ_{\perp}^2 (Å ²)
$\mu^{bef}(E)$	2.504(5)	0.0069(6)	2.497(5)	0.0066(7)
$\mu^{aft}(E)$	2.511(6)	0.0076(8)	2.479(6)	0.0080(7)

Table 4.5: Best fit parameters of the EXAFS spectra collected before ($\mu^{bef}(E)$) and after ($\mu^{aft}(E)$) the 500 °C annealing. The bulk Co lattice parameter is 2.506 Å.

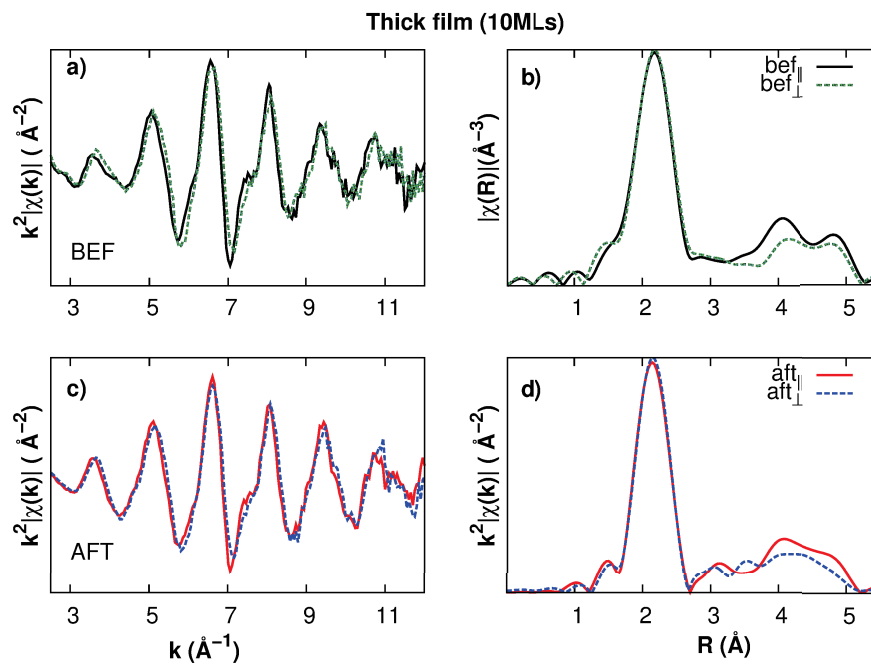


Figure 4.21: EXAFS signals and their Fourier transform for the thick film before (top) and after (bottom) the 500 °C treatment. Data were collected using beam polarizations parallel (solid lines) and perpendicular (dashed lines) to the film plane.

perpendicular direction. However, within the uncertainty we can consider an overall isotropic arrangement of the first coordination shell. Upon annealing, R_{\parallel} and R_{\perp} show no significant change, whereas the average disorder is found to decrease in both the directions, as estimated by the σ^2 parameters. We can interpret this behaviour as a general smoothing of the film.

The EXAFS region of the spectra measured for the thin film point out some differences with respect to the thick film case. $\mu_{\perp}^{bef}(E)$ and $\mu_{\parallel}^{bef}(E)$. They can be noticed in Fig.4.22a,b.

The EXAFS data collected before the annealing show some anisotropy (Fig.4.22a,b). In k -space, $\mu_{\perp}^{bef}(E)$ oscillates with a lower frequency and the oscillations go back in phase with $\mu_{\parallel}^{bef}(E)$ only after $k = 7 \text{ \AA}^{-1}$. Moreover, the oscillations of $\mu_{\parallel}^{bef}(E)$ are slightly higher and less noisy, indicating a higher coordination in the in-plane direction, coherently with our XANES interpretation. However, when moving to the R space, no shift is found in the first coordination shell ($R \simeq 2\text{\AA}$)³.

Upon annealing, a phase delay appears above $k = 5 \text{ \AA}^{-1}$ resulting into an evident shift of the FT main peak, as shown in Fig.4.22d. In R (and k) space, the difference of the signals $\chi_{\perp}^{aft} - \chi_{\parallel}^{aft}$ increases with R (and k), suggesting the shift is due to a coordination effect. In particular, the lower intensity of the $\mu_{\perp}^{aft}(E)$ is ascribed to a lower Co coordination in this direction: this effect can be seen already in the first shell of Fig.4.22d, and it is enhanced in the second shell showing strong signal suppression. However, this cannot be linked to a Co-Ir alloying, since this contribution would be visible first at low k , and would leave a net fingerprint also in the XANES region. In particular, if this was the case, an evident increase in the white line and in the pre-edge region would be noticed.

From a quantitative point of view, the values extracted from the fit to $\mu^{bef}(E)$ and $\mu^{aft}(E)$ indicate a small compression of R_{\perp} and a small expansion of R_{\parallel} . This is found together with an increasing σ_{\perp} (see Tab.4.5b). We ascribe this volume-conserving stretching to a surface strain caused by the lattice mismatch between Co and Ir.

General discussion

The significant amount of oxide shown by the thick film can be reasonably linked to the ambient pressure exposure. In this respect, the Co could oxidise either from above the Gr, in case of a partial intercalation, or through the defects of the Gr layer, in case of poor Gr efficiency in the oxidation prevention. The latter hypothesis, however, can be ruled out on the basis of the minor amount of oxide found in the thin film. In facts, if the Gr defects would allow

³The small disagreement of further shells are not reliable due to the high disorder of the system.

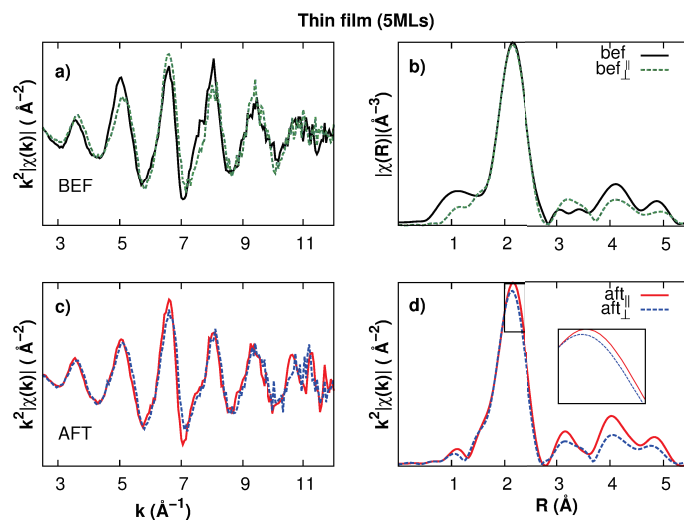


Figure 4.22: EXAFS of the thin film before **a)** and after **c)** the 500 °C treatment are shown in k -space and in R -space as Fourier transformed signals **b)** and **d)**, respectively. Data were collected using beam polarizations parallel (solid lines) and perpendicular (dashed lines) to the film plane. The inset in panel **d)** shows an enlarged view of the region $2 \div 2.5 \text{ \AA}$.

for some Co oxidation, one would expect a higher CoO concentration in the thinner film. On the contrary, the data suggest an oxidation taking place at the surface, thus we interpret the presence of CoO as an evidence of the partial intercalation.

Moreover, the reduction of the CoO found upon the 500 °C annealing for both the thick and the thin films, could be explained by the CoO desorption from the surface. However, this would require a decrease in the total Co amount on the sample and, as a consequence, a decrease of the edge jump of XANES data. On the contrary, the discontinuity of the absorption edge is stable and the desorption can be safely excluded. Therefore the further annealing can be though as promoting the dissociation of Co from the oxygen and the subsequent total intercalation.

As far as the microstructural analysis is concerned, structural parameters were evaluated from the fits to the EXAFS data. Their evolution shows that both films have a lattice parameter compatible with the bulk Co with a small compression in R_{\perp} , upon the 300 °C intercalation.

After the 500 °C annealing, for the thick film, the average disorder decrease and no further changes are observed. On the contrary, the thin film presents higher σ and an anisotropic arrangement: the film is stretched along the film plane and a squeezed in the perpendicular direction. This finding about a

thickness-dependent structural evolution is in agreement with the conclusions presented in Sec.4.2. Moreover, the volume-conserving structural modifications reported in Tab.4.5, bring the atoms of two different layers closer to each other. Therefore, the interaction among their electrons is expected to be stronger. This stronger interaction most likely originates the PMA enhancement observed upon intercalation [1].

At the beginning of this chapter, in Sec.4.1, we showed that on the basis of diffraction and AR-XPS observations, intermixing can occur upon a double annealing (at 300 and then at 500 °C) of a Co film deposited on Gr/Ir. However, the EXAFS analysis presented in this Section does not show evidences of Co-Ir coordination. Therefore, the effect observed with GIXD is most likely an outcropping of the Ir substrate, causing the Co film breaking into smaller clusters. This means that the interface is actually getting rougher, as correctly found by the GIXD analysis. Nevertheless, the formation of a Co-Ir alloy like the one described in Sec.4.3, requires most likely higher annealing temperatures.

Conclusions

We studied the local structure of two Co films intercalated at 300 °C between Graphene and Ir(111) and later brought at ambient pressure.

The analysis of the XANES region of the spectra gave interesting details on the oxidation prevention provided to the Co film by the Gr layer. In particular, our XANES analysis revealed the presence of a CoO phase being more abundant for the thicker film, ruling out the hypothesis of oxidation through the Gr layer. Upon further annealing at 500 °C and a second exposure to ambient pressure, the CoO phase appears to be strongly reduced suggesting the oxidation to be a consequence of incomplete intercalation. Interestingly, the Gr is found to maintain its oxidation-preventing properties even after these two treatments. Moreover, the Co amount does not decrease upon annealing: this finding, together with the CoO decrease, leads to the conclusion that a Co-O dissociation must have occurred together with the complete intercalation upon the second annealing.

Moreover, from the analysis of the EXAFS region, a description of the local structure could be obtained. After the 500 °C annealing the thick film is found to maintain its original lattice parameter denoting an overall stability of the film structure. On the contrary, the thin film was found to be stretched along the film plane and squeezed in the perpendicular direction. This strain, induced by the lattice mismatch with the substrate, can most likely be linked with the enhancement of the PMA.

These findings give valuable information both for the fundamental science and for applicative purposes. In particular, exploiting the coordination

sensitivity of the XANES region together with the fine directional sensitivity provided by EXAFS, we were able to assess important details regarding intercalated Co films.

Conclusions

This thesis focused on the structural evolution of Co thin films intercalated between Gr/Ir. In particular, it aimed to provide details on the peculiar magnetic response of the films upon the intercalation procedure.

The structure of Co films has been investigated on the short- and long-range order, using complementary X-ray techniques. Synchrotron radiation (XRR, GIXD, XANES, EXAFS) and laboratory techniques (MOKE, LEED, AR-XPS) were used to describe the structural evolution of the films upon intercalation. Different experimental strategies were adopted in order to disentangle the contribution of the several parameters such as: the Gr layer, the film thickness, the annealing temperatures and times.

Four experiments were carried out and their results allowed to achieve a deep understanding of the atomic structure, morphology and magnetic response of the Gr/Co/Ir films as well their evolution as a function of the annealing temperature.

In the first experiment, XRR and AR-XPS were used to study the evolution of the Co films upon intercalation. Aiming to disentangle the Gr effects from the thermal-induced modifications, the behaviour of an intercalated film was compared to that of a bare Co film on Ir. The two systems behaved differently upon annealing at 500 °C. In particular, the Co-Ir interface was found to get rougher in the Gr/Co/Ir case, while it was observed get smoother in the bare Co/Ir case. This led to the conclusion that Gr favours the intermixing thanks to a colander-like effect during the intercalation. In facts, when the Co passes through the Gr defects, it breaks down into small clusters. Such clusters, getting in touch with the hot Ir substrate are stretched by the lattice mismatch with the substrate. On the other hand, the higher stability of bare Co film has been linked to the higher Co coordination. Therefore, the intermixing phenomenon has been thought to require the film integrity loss.

In the second experiment, we tried to gain some insight in the intercalation process. Since in the first experiment the intermixed film was thinner than the other one, here we wanted to get rid of the potential effects due to the film thickness. For this reason we studied two Co films grown with the same evaporation times: one was grown on bare Ir, the other one on Gr/Ir. For the bare

film, the XRR measurements confirmed the smoothing effect of the annealing. Moreover, the GIXD data allowed us to follow the ordering process along the in-plane direction induced by the annealing. Analogously, for the Gr system, the XRR showed no intermixing upon annealing. Moreover, a decrease of the interface roughness was observed. This finding is an apparent contradiction to the previous measurements. However, the colander model proposed to explain the integrity-dependent intermixing, can solve this consistency problem. In fact, since the film studied in this experiment is thicker than that of experiment #1, the stronger contribution from the volume effects overcoming the surface ones, might be invoked to explain the higher film's stability. These results agree with the need of integrity loss in order to facilitate the intermixing. As a further confirmation, we tried to reproduce this effect using a "hot-deposition", *i.e.* growing Co directly on the hot Ir substrate. The GIXD measurements showed a Co peak particularly broad and shifted towards the Ir value, providing evidence of an in-plane stretching. Moreover, we ascribed the shoulder found on this peak, to the presence of two Co phases with different periodicities. Therefore, the model we built to interpret XRR data was made up of a topmost pure Co layer, an intermediate Co-Ir transition layer and the Ir substrate. The high roughness among these components testifies an intermixing/outcropping effect and represents the evidence for the colander-picture accuracy.

In our third experiment, we focused on the local scale characterization of bare Co/Ir systems. Combining AR-XPS and MOKE, we followed the evolution of the magnetic response of a 8 ML film. The magnetic response was found to be modified when the linear behaviour of the AR-XPS was lost, *i.e.* after the film homogeneity was lost. In order to investigate the structural evolution of the Co at the local scale, we used XANES on a 9 ML bare Co film. Upon repeated annealing at temperatures up to 900 °C, we found the progressive evolution of the XANES feature due to modifications to the Co chemical environment. On the basis of *ab-initio* simulations, we interpreted these changes as a change in the Co coordination, progressively involving more Ir atoms.

In the fourth experiment, we focused on the Gr-covered system and analysed them after a short exposure to ambient pressure. Thanks to the XANES results, we could easily find the presence of some Co-oxide leading us to the nature of the oxidation sites. In fact, being the CoO phase more abundant for the thicker film, we could deduce the oxidised phase was only on top of the Gr, concerning only the part of Co not intercalated underneath the Gr. Upon annealing and successive ambient pressure exposure, the amount of oxide was reduced but the amount of Co was not. This was explained with the Co dissociation from the O in the CoO molecule together with the final Co

intercalation.

The EXAFS region of the spectra, gave interesting results on the microstructural anisotropy. In fact, only the spectra of the film thinner than t_c were found to be affected by the annealing. This film was found to stretch along the film plane, with a consequent shrinking in the perpendicular direction conserving the unit cell volume. This stretching is thought to be responsible for the enhanced PMA of intercalated Co films. In fact, the increased closeness of the Co atoms in two neighbouring layers, can enhance the d bands overlapping and lead to a stronger PMA. In agreement with this interpretation, the 10 ML film (thicker than t_c), evolved differently.

The complex phenomena affecting the magnetic response of Co thin films have been widely investigated with complementary, state-of-the-art techniques. The structural evolution of the Co films upon thermal treatments has been found to depend on several parameters, such as: film thickness and integrity, annealing temperatures and times, presence of Gr. The interplay of these parameters determines the strength of the surface effects on the volume contributions. This, in turn, may affect the overall response of the Co films.

In conclusion, the analysis presented so far demonstrates that surface effects can be induced by thermal treatments. Such effects can affect both the structure and the overall magnetic response of the films. Therefore, particular care is required during the film growth and intercalation between Gr and Ir. In fact, minor modifications in one of the parameters can dramatically modify the overall magnetic anisotropy of the film.

Rèsumè substantiel

6.1 Introduction

Ce memoire décrit l'évolution structurelle des films de Cobalt lors du recuit. Le but de ce travail est de trouver une relation entre l'anisotropie structurelle et magnétique des films ferromagnétiques. Une attention particulière est portée aux effets de surface sur la réponse magnétique macroscopique des systèmes.

En général, les films ferromagnétiques peuvent être exploités dans l'application la plus avancée pour le magnétisme: la technologie sous-jacente au stockage magnétique des données [2, 3, 4]. En fait, les structures des films minces artificiels ont été utilisées depuis les années 1990 [5]. Plus tard, au début des années 2000, les mémoires magnétiques non volatiles ont été proposées comme des mémoires magnétiques d'accès aléatoire (Magnetic Random Access Memories, MRAM) [6]. A cet égard, les films minces ferromagnétiques possédant une Anisotropie Magnétique Perpendiculaire (PMA) occupent une position éminente en raison de leur utilisation potentielle dans le MRAM à très haute densité [7, 8, 9, 10, 11].

La PMA, par rapport à l'aimantation longitudinale, permet d'obtenir une plus petite taille des bits magnétiques tout en préservant l'état magnétique des fluctuations thermiques. Depuis 1978, quand le premier film d'enregistrement de Co-Cr avec PMA a été rapporté [12], un certain nombre de systèmes ont été explorés. Parmi ceux-ci, le Co hcp est connu pour avoir une forte anisotropie magnétique intrinsèque, et pour développer PMA pour épaisseurs au-dessous d'une valeur critique $t_c \simeq 7$ monocouches (ML) [13, 1].

Pour que les films de Co facilement oxydables conviennent aux applications, ils doivent être protégés contre la dégradation. Ce défi a conduit à la fabrication de films protégés par une couche de graphène (Gr) caractérisés par une stabilité chimique améliorée. La croissance de Gr *in-situ* sur le film mince de Co peut être obtenue par dépôt chimique en phase vapeur (CVD). Cependant, cette procédure nécessite des températures élevées ($T \simeq 1000$ °C) représentant un problème pour l'intégrité structurelle de la couche de Co. D'autre part, l'utilisation des procédures d'intercalation requiert des températures beaucoup plus basses ($T \simeq 300$ °C) en évitant les problèmes d'intégrité pendant la production des hétérostructures Gr/Co/Ir(111) [14].

On a démontré que le recouvrement en Gr affecte les propriétés magnétiques des films minces de Co: les systèmes intercalés de Gr/Co/Ir présentent des domaines magnétiques plus petits tandis que le PMA est conservé même par le film Co dépassant t_c [1]. Ces résultats ont suscité un regain d'intérêt pour les applications de ces hétérostructures et ont stimulé la recherche fondamentale sur le rôle de Gr dans les propriétés magnétiques des couches de Co intercalées. Les travaux récents fournissent des explications différentes pour le comportement observé en invoquant la topologie d'intercalation [15], l'hybridation des orbitales d'électrons Gr et Co [16, 1], l'ordre magnétique du Co après l'intercalation [17] et le moment magnétique du Gr [18]. Bien qu'une grande attention ait été accordée à l'interaction de l'interface Co-Gr, moins a été étudié sur la contribution de l'interaction Co-Ir lors de la préparation des hétérostructures Gr/Co/Ir(111).

Ce travail met l'accent sur les effets à l'interface Co-Ir et vise à fournir une caractérisation fine de cette région combinant plusieurs techniques *in-situ*. Les informations complémentaires obtenues avec chaque technique ont fourni une description détaillée de l'évolution structurale des couches minces de Co lors de l'intercalation. En particulier, on a utilisé des techniques de laboratoire (spectroscopie de photoélectrons aux rayons X "XPS" et l'effet Kerr magnéto-optique ou "MOKE") pour obtenir des informations sur la distribution en Co le long de la direction perpendiculaire à la surface du film et sur sa réponse magnétique. De plus, des techniques de rayonnement synchrotron (spectroscopie d'absorption des rayons X "XAS" et la diffraction des rayons X à incidence rasante "GIXD") ont été utilisées pour évaluer la structure locale et l'ordre à longue distance des films.

Ce mémoire est organisé de la façon suivante:

Chapitre I: Introduction au concept d'anisotropie magnétique avec quelques détails concernant le cas particulier des films de Co.

Chapitre II: Les phénomènes qui conduisent l'interaction entre la lumière et la matière.

Chapitre III et IV: Techniques de laboratoire et techniques de rayonnement synchrotron.

Chapitre V: Mesures expérimentales - divisé en quatre sections: chaque section traite d'un cycle expérimental différent impliquant plusieurs techniques de caractérisation.

Chapitre VI: Conclusion.

6.2 Réalisation expérimentale

La structure des films de Co a été étudiée à court et à long terme, en utilisant des techniques complémentaires de rayons X. On a utilisé le rayonnement synchrotron (XRR, GIXD, XANES, EXAFS) et les techniques de laboratoire (MOKE, LEED, AR-XPS) pour décrire l'évolution structurale des films lors

de l'intercalation. Diff rentes strat gies exp rimentales ont  t  adopt es afin de d m ler la contribution des diff rents param tres tels que: la couche de Gr, l' paisseur du film, les temp ratures et les temps de recuit.

Quatre exp riences ont  t  r alis es et leurs r sultats ont permis d'obtenir une compr hension approfondie de la structure atomique, de la morphologie et de la r ponse magn tique des films Gr/Co/Ir ainsi que leur  volution en fonction de la temp rature de recuit.

Exp rience 1: XRR et AR-XPS ont  t  utilis s pour  tudier l' volution des films de Co lors de l'intercalation. Dans le but de d m ler les effets de Gr des modifications thermiques induites, le comportement d'un film intercal  a  t  compar    celui d'un film de Co nu sur Ir. Les deux syst mes se comportent diff remment lors du recuit   500  C. En particulier, l'interface Co-Ir s'est r v l e plus rugueuse dans le cas Gr/Co/Ir par rapport au cas Co/Ir. Ceci a conduit   la conclusion que le Gr favorise l'entrem lement gr ce   un effet "passoire" lors de l'intercalation. En fait, lorsque le Co passe par les d fauts Gr, il se d compose en petits grappes. Tels grappes, entrant en contact avec le substrat d'Ir chaud, sont  tir s par l'incompatibilit  du r seau avec celui du substrat. D'autre part, la plus grande stabilit  du film de Co nu a  t  li e   la plus haute coordination du Co. Par cons quent, le ph nom ne d'entrem lement doit exiger la perte d'int grit  du film.

Exp rience 2: compr hension du processus d'intercalation. Puisque dans la premi re exp rience, le film m lang   tait plus mince que l'autre, nous voulions ici  liminer les effets potentiels dus   l' paisseur du film. Pour cette raison, nous avons  tudi  deux films de Co cultiv s avec les m mes temps d' vaporation: l'un  tait cultiv  sur Ir nu, l'autre sur Gr/Ir. Pour le film nu, les mesures XRR ont confirm  l'effet de lissage du recuit. De plus, les donn es GIXD nous ont permis de suivre le processus de ordonnement induite par le recuit dans le plan du film. De fa on analogue, pour le syst me Gr, le XRR ne pr sentait aucun m lange lors du recuit. De plus, une diminution de la rugosit  de l'interface a  t  observ e. Cette constatation est une apparente contradiction avec les mesures pr c dentes. Cependant, le mod le de passoire propos  pour expliquer le m lange d pendant de la perte d'int grit  peut r soudre ce probl me de coh rence. En fait, puisque le film  tudi  dans cette exp rience est plus  pais que celui de l'exp rience 1, on peut invoquer la plus forte contribution des effets de volume surmontant ceux de surface pour expliquer la sup rieure stabilit  du film.

Ces r sultats concordent avec la n cessit  d'une perte d'int grit  afin de faciliter le m lange. Comme confirmation suppl mentaire, nous avons essay  de reproduire cet effet en utilisant un "d p t   chaud", *i.e.* croissant le Co directement sur le substrat d'Ir chaud. Les mesures de GIXD ont montr  un pic de Co particuli rement large et d cal  vers la valeur de l'Ir, fournissant une  vidence

d'un étirement dans le plan. En outre, nous avons attribué l'épaule trouvée sur le pic du Co, à la présence de deux phases Co à différentes périodicité. Par conséquent, le modèle que nous avons construit pour interpréter les données XRR était composé d'une couche de Co pure supérieure, d'une couche intermédiaire de transition Co-Ir et du substrat Ir. La rugosité élevée de ces composants témoigne d'un effet de mélange entre Co-Ir ou d'affleurement du Ir et représente la preuve de l'efficacité du modèle à passer.

Expérience 3: Caractérisation à l'échelle locale des systèmes Co/Ir. Combinant AR-XPS et MOKE, nous avons suivi l'évolution de la réponse magnétique d'un film de 8 ML. On a trouvé que la réponse magnétique était modifiée lorsque le comportement linéaire du AR-XPS était perdu et, donc, lorsque l'homogénéité du film était perdue. Afin d'étudier l'évolution structurale du Co à l'échelle locale, nous avons utilisé XANES sur un film de Co nu de 9 ML. Lors d'un recuit répété à des températures allant jusqu'à 900 °C, nous avons constaté l'évolution progressive de la caractéristique XANES en raison des modifications apportées à l'environnement chimique Co. Sur la base des simulations *ab-initio*, nous avons interprété ces changements comme l'évolution de la coordination du Co, impliquant progressivement plus d'atomes d'Ir.

Expérience 4: Analyse du système Gr/Co/Ir après exposition à la pression ambiante. Grâce aux résultats XANES, nous avons pu facilement trouver la présence d'un certain Co-oxyde nous conduisant à la nature des sites d'oxydation. En fait, étant la phase de CoO plus abondante pour le film plus épais, on pourrait déduire que la phase oxydée était seulement au-dessus du Gr, concernant seulement la partie de Co non intercalée sous le Gr. Lors du recuit et de la successive exposition à la pression ambiante, la quantité d'oxyde a été réduite, mais la quantité était stable. Ceci a été expliqué avec la dissociation de Co de O dans la molécule CoO conjointement avec l'intercalation finale de Co.

La région EXAFS des spectres a donné des résultats intéressants sur l'anisotropie microstructurale. En fait, seuls les spectres du film plus minces que t_c ont été trouvés pour être affectés par le recuit. On a trouvé que ce film s'étirait le long du plan de film, avec un conséquent rétrécissement dans la direction perpendiculaire, conservant le volume de cellule unitaire. On pense que cet étirement est responsable de la PMA intensifiée des films de Co intercalés. En fait, la proximité accrue des atomes de Co dans deux couches voisines, peut améliorer les orbitales électroniques d chevauchants et conduire à un PMA plus fort. En accord avec cette interprétation, le film de 10 ML (plus épais que t_c) a évolué différemment.

Les complexes phénomènes affectant la réponse magnétique des films minces de Co ont été largement étudiés avec des techniques avancées et complémentaires. On a constaté que l'évolution structurale des films de Co après les traite-

ments thermiques d ependait de plusieurs param tres, tels que: l' paisseur et l'int grit  du film, les temp ratures et les temps de recuit, la pr sence de Gr. L'interaction de ces param tres d termine la force des effets de surface sur les contributions de volume. Ceci,   son tour, peut affecter la r ponse globale des films de Co.

En conclusion, l'analyse pr sent e d montre que les effets de surface peuvent  tre induits par des traitements thermiques. Tels effets peuvent affecter   la fois la structure et la r ponse magn tique globale des films. Par cons quent, un soin particulier est n cessaire pendant la croissance du film et l'intercalation entre Gr et Ir. En fait, des modifications mineures dans l'un des param tres peuvent modifier radicalement l'anisotropie magn tique globale du film.

Acknowledgements

At the end of these tough three years, I feel profoundly changed, enormously enriched and even a bit older. During my project I have been lucky enough to meet tons of new, inspiring people. I would like to thank them for keeping my curiosity alive and for sharing a lot of good times, healthy discussion, and, sometimes, not-so-healthy hobbies.

First of all, I feel the need for thanking my two supervisors, Carlo and Roberto, who chose to believe in my potentialities and allowed me to dive into this *adventure*.

I wish to thank also my closest colleagues in the past years, Jakub and Sergio, and the ID03 wonderful team for teaching me a lot. En plus, Helena and Thomas, vous m'avez fait sentir comme chez moi. Vous etiez mes reperes quand rien marchait. Merci, vraiment. Francesco, grazie per avermi ricordato ogni singolo giorno i livelli che la determinazione può raggiungere. Grazie per tutto l'aiuto prestato e per i confronti e le discussioni costruttive che abbiamo avuto. Non so scegliere quale sia stato piú prezioso. Anastasia and Marta, grazie per i coffee break, per i momenti spesi insieme in laboratorio e per il supporto nei momenti piú bui.

A huge “thank you” is for the people I met in Grenoble with whom I have shared a crazy amount of good memories. Grazie al mio “Italian team”: Federica, Leo, Valeria, Michael, Francesco¹, Luca and Niccoló per avermi sempre ricordato i principi di vita italiana.

Thanks to Ash, Matteo, Stefano, Davide, Valentina, Casper, Margherita, Franz, Mattia (aka *er romano*), Tommaso, Salvo, Lur, and all the other people met in the HERCULES: knowing that we were suffering together has been a good reason to carry on.

Un ringraziamento speciale va alla mia famiglia per aver rappresentato un appoggio su cui poter contare quando le cose non andavano nel verso giusto. E grazie per aver accettato di avermi lontana tanto tempo. C'è chi dice lo abbiate fatto apposta, devo credergli?

Infine, grazie agli amici di sempre: anche se alcuni di voi erano felici di avermi fuori dai piedi, siete riusciti a non farmi sentire lontana durante il mio periodo francese. Diversa, un po', sí. Lontana, mai. Grazie quindi a Matteo (aka *il nuovo francese*), Valerio (o *manipulator-killer*), Gian M...arco, Gabriele, Paolo, Mandi, Gaia, Fffabiomoretti & Mmmarcodecicco, Michelone,

Cristina, insomma, tutto il team di DSPG. Grazie a Sara, con cui ho condiviso anche le gioie dei beamtime e a Giorgia, per essere la mia fornitrice ufficiale di spunti e confronti, sempre utilissimi. Un ringraziamento speciale va riservato poi a Simona, punto di riferimento costante negli anni.

...e poi, ovviamente, *Paffy*. Pensavi davvero che mi fossi dimenticata di te? Giammai! Abbiamo iniziato insieme, sofferto insieme, esitato sul modulo E insieme. E oggi finiamo quest'avventura insieme. Da domani, mi sentirò un po' piú sola, nella mia carriera. Sei insostituibile.

E ora che siamo davvero alla fine, grazie alla mia dolce metà, per aver sempre creduto in me, per essere la dimostrazione vivente che con la giusta determinazione (e tanta fatica), niente è impossibile e non c'è mai limite al *miglio*.

Grazie, grazie, grazie.

I.

Bibliography

- [1] N. Rougemaille, A.T. N'Diaye, J. Coraux, C. Vo-Van, O. Fruchart, and A.K. Schmid. Perpendicular magnetic anisotropy of cobalt films intercalated under graphene. *Appl. Phys. Lett.*, 101:142403, 2012.
- [2] J. Stöhr. *X-Ray Absorption*, volume 92, chapter xx. Wiley, 1988.
- [3] Finn Jorgensen. *The complete handbook of magnetic recording*. McGraw-Hill/TAB Electronics, 1996.
- [4] Shan X Wang and Alex M Taratorin. *Magnetic Information Storage Technology: A Volume in the Electromagnetism Series*. Academic press, 1999.
- [5] JB Kortright, DD Awschalom, J Stöhr, SD Bader, YU Idzerda, SSP Parkin, Ivan K Schuller, and H-C Siegmann. Research frontiers in magnetic materials at soft x-ray synchrotron radiation facilities. *Journal of Magnetism and Magnetic Materials*, 207(1):7–44, 1999.
- [6] David D Awschalom, Robert A Buhrman, James M Daughton, Michael L Roukes, and Stephan von Molnar. Spin electronics. Technical report, DTIC Document, 2003.
- [7] S. Iwasaki and Y. Nakamura. An analysis for the magnetization mode for high density magnetic recording. *IEEE Trans. Magn.*, 13:1272, 1977.
- [8] N. Nishimura, T. Hirai, A. Koganei, T. Ikeda, K. Okano, Y. Sekiguchi, and Y. Osada. Magnetic tunnel junction device with perpendicular magnetization films for high-density magnetic random access memory. *J. Appl. Phys.*, 91:5246, 2002.
- [9] S Ikeda, K Miura, H Yamamoto, K Mizunuma, HD Gan, M Endo, S Kanai, J Hayakawa, F Matsukura, and H. Ohno. A perpendicular-anisotropy *cofeb-mgo* magnetic tunnel junction. *Nature Mat.*, 9:721, 2010.
- [10] R. A. Lukaszew, Y. Sheng, C. Uher, and R. Clarke. Use of magnetocrystalline anisotropy in spin-dependent tunneling. *Appl. Phys. Lett.*, 75(13):1941, 1999.

- [11] Takayuki Nozaki, Anna Koziol-Rachwał, Witold Skowroński, Vadym Zayets, Yoichi Shiota, Shingo Tamaru, Hitoshi Kubota, Akio Fukushima, Shinji Yuasa, and Yoshishige Suzuki. Large voltage-induced changes in the perpendicular magnetic anisotropy of an mgo-based tunnel junction with an ultrathin fe layer. *Phys. Rev. Appl.*, 5:044006, 2016.
- [12] S. Iwasaki and K. Ouchi. Co-cr recording films with perpendicular magnetic anisotropy. *IEEE Trans. Magn.*, 14:849, 1978.
- [13] R. Allenspach, M. Stampanoni, and A. Bischof. Magnetic domains in thin epitaxial co/au(111) films. *Phys. Rev. Lett.*, 65:3344, 1990.
- [14] J. Coraux, A. T. N'Diaye, N. Rougemaille, C. Vo-Van, A. Kimouche, H. Yang, M. Chshiev, N. Bendiab, O. Fruchart, and A. K. Schmid. Air-protected epitaxial graphene/ferromagnet hybrids prepared by chemical vapor deposition and intercalation. *J. Phys. Chem. Lett.*, 3:2059, 2012.
- [15] S. Vlaic, A. Kimouche, J. Coraux, B. Santos, A. Locatelli, and N. Rougemaille. Cobalt intercalation at the graphene/iridium(111) interface: Influence of rotational domains, wrinkles, and atomic steps. *Appl. Phys. Lett.*, 104:342, 2014.
- [16] D. Pacilé, S. Lisi, I. Di Bernardo, M. Papagno, L. Ferrari, M. Pisarra, M. Caputo, S. K. Mahatha, P. M. Sheverdyaeva, P. Moras, P. Lacovig, S. Lizzit, A. Baraldi, M. G. Betti, and C. Carbone. Electronic structure of graphene/co interfaces. *Phys. Rev. B*, 90:195446, 2014.
- [17] R. Decker, J. Brede, N. Atodiressei, V. Caciuc, S. Blügel, and R. Wiesendanger. Atomic-scale magnetism of cobalt-intercalated graphene. *Phys. Rev. B*, 87:041403, 2013.
- [18] H. Vita, St. Böttcher, P. Leicht, K. Horn, A. B. Shick, and F. Máca. Electronic structure and magnetic properties of cobalt intercalated in graphene on ir(111). *Phys. Rev. B*, 90:165432, 2014.
- [19] L. Néel. —. *J. Phys. Rad*, 15:376, 1954.
- [20] MT Johnson, PJH Bloemen, FJA Den Broeder, and JJ De Vries. Magnetic anisotropy in metallic multilayers. *Rep. Prog. Phys.*, 59(11):1409, 1996.
- [21] J. Drnec, S. Vlaic, I. Carlomagno, C. J. Gonzalez, H. Isern, F. Carlà, R. Fiala, N. Rougemaille, J. Coraux, and R. Felici. Surface alloying upon co intercalation between graphene and ir (111). *Carbon*, 94:554, 2015.
- [22] W.Y. Chan, D.C. Tsai, W.H. Chen, C.H.T. Chang, and J.S. Tsay. Enhancement of the polar coercive force for annealed co/ir(111) ultrathin films. *Journal of Korean Physical Society*, 62:1945, 2013.

- [23] P Fornasini. *Synchrotron Radiation-Basics, Methods and Applications*, chapter XAFS. Springer-Verlag, 2015.
- [24] D. Bonnin. X-ray absorption in lamellar compounds. *J. Phys. Colloques*, 47(C8):831–836, 1986.
- [25] Adriano Filipponi. Exafs for liquids. *Journal of Physics: Condensed Matter*, 13(7):R23, 2001.
- [26] J.J. Rehr and Albers R.C. X-ray absorption fine structure. *Rev. Mod. Phys.*, 72(3), 2000.
- [27] H. Luth. *Solid Surfaces, Interfaces and Thin Films*. Springer, 2010.
- [28] Settimio Mobilio, Federico Boscherini, and Carlo Meneghini. *Synchrotron Radiation*. Springer, 2015.
- [29] JJ Rehr and AL Ankudinov. Progress in the theory and interpretation of xanes. *Coordination Chemistry Reviews*, 249(1):131–140, 2005.
- [30] JJ Rehr, AL Ankudinov, B Ravel, and SD Conradson. Real space multiple scattering calculation of xanes. *Phys. Rev. B*, 58, 1998.
- [31] Elias Vlieg. Rod: a program for surface x-ray crystallography. *Journal of Applied Crystallography*, 33(2):401–405, 2000.
- [32] Matts Björck and Gabriella Andersson. Genx: an extensible x-ray reflectivity refinement program utilizing differential evolution. *Journal of Applied Crystallography*, 40(6):1174–1178, 2007.
- [33] B.E. Warren. *X-ray Diffraction*. Dover Publications, 1990.
- [34] Robert Feidenhans. Surface structure determination by x-ray diffraction. *Surface Science Reports*, 10(3):105–188, 1989.
- [35] Jakub Drnec, Tao Zhou, Stelian Pinteau, Willem Onderwaater, Elias Vlieg, Gilles Renaud, and Roberto Felici. Integration techniques for surface X-ray diffraction data obtained with a two-dimensional detector. *Journal of Applied Crystallography*, 47(1), 2014.
- [36] Ibn Sahl. *On Burning Mirrors and Lenses*. Baghdad Court, 984.
- [37] J Penfold and RK Thomas. The application of the specular reflection of neutrons to the study of surfaces and interfaces. *Journal of Physics: Condensed Matter*, 2(6):1369, 1990.
- [38] Charles G Darwin. Xxxiv. the theory of x-ray reflexion. *The London, Edinburgh, and Dublin Philosophical Magazine and Journal of Science*, 27(158):315–333, 1914.

- [39] J. A. Prins. Über die beugung von röntgenstrahlen in flüssigkeiten und lösungen. *Zeitschrift für Physik*, 56(9):617–648, 1929.
- [40] Peter Paul Ewald. Zur begründung der kristalloptik. *Annalen der Physik*, 359(23):519–556, 1917.
- [41] R de L Kronig. On the theory of dispersion of x-rays. *JOSA*, 12(6):547–557, 1926.
- [42] Xiao-Lin Zhou and Sow-Hsin Chen. Theoretical foundation of x-ray and neutron reflectometry. *Physics Reports*, 257(4):223–348, 1995.
- [43] L Névot and P Croce. Sur l'étude des couches superficielles monoatomiques par réflexion rasante (spéculaire ou diffuse) de rayons x, par la méthode de l'empilement sandwich'. *Journal of Applied Crystallography*, 8(2):304–314, 1975.
- [44] Max Born and Emil Wolf. *Principles of optics: electromagnetic theory of propagation, interference and diffraction of light*. CUP Archive, 2000.
- [45] Michael Faraday. Experimental researches in electricity. and twentieth series. section 26th. on new magnetic actions; and on the magnetic condition of all matter. In *Abstracts of the Papers Communicated to the Royal Society of London*, volume 5, pages 592–595. The Royal Society, 1843.
- [46] John Kerr. Xliii. on rotation of the plane of polarization by reflection from the pole of a magnet. *The London, Edinburgh, and Dublin Philosophical Magazine and Journal of Science*, 3(19):321–343, 1877.
- [47] HR Hulme. The faraday effect in ferromagnetics. *Proceedings of the Royal Society of London. Series A, Containing Papers of a Mathematical and Physical Character*, 135(826):237–257, 1932.
- [48] Petros N Argyres. Theory of the faraday and kerr effects in ferromagnetics. *Physical Review*, 97(2):334, 1955.
- [49] Lars Onsager. Reciprocal relations in irreversible processes. ii. *Physical Review*, 38(12):2265, 1931.
- [50] I. Carlomagno, J. Drnec, A. M. Scaparro, S. Cicia, S. Vlais, R. Felici, and C. Meneghini. Co-ir interface alloying induced by thermal annealing. *J. Appl. Physics*, xxx, 2016.
- [51] C.S. Fadley. *Electron Spectroscopy: Theory, Techniques and Applications*, volume 2, chapter Basic concepts of XPS. Academic Press, 1978.
- [52] Sven Tougaard. Quantitative xps: non-destructive analysis of surface nano-structures. *Applied surface science*, 100:1–10, 1996.

- [53] HS Hansen and S Tougaard. Separation of spectral components and depth profiling through inelastic background analysis of xps spectra with overlapping peaks. *Surface and interface analysis*, 17(8):593–607, 1991.
- [54] Sven Tougaard. Energy loss in xps: Fundamental processes and applications for quantification, non-destructive depth profiling and 3d imaging. *Journal of Electron Spectroscopy and Related Phenomena*, 178:128–153, 2010.
- [55] ER Moog and SD Bader. Smoke signals from ferromagnetic monolayers: p (1× 1) fe/au (100). *Superlattices and microstructures*, 1(6):543–552, 1985.
- [56] ZQ Qiu and Samuel D Bader. Surface magneto-optic kerr effect (smoke). *Journal of magnetism and magnetic materials*, 200(1):664–678, 1999.
- [57] O. Mathon, A. Beteva, J. Borrel, D. Bugnazet, S. Gatla, R. Hino, I. Kantor, T. Mairs, M. Munoz, S. Pasternak, F. Perrin, and S. Pascarelli. The time-resolved and extreme conditions XAS (TEXAS) facility at the European Synchrotron Radiation Facility: the general-purpose EXAFS bending-magnet beamline BM23. *Journal of Synchrotron Radiation*, 22(6):1548–1554, Nov 2015.
- [58] RF Pettifer, M Borowski, and PW Loeffen. The physics of ionization chambers—or how to improve your signal-to-noise ratio for transmission exafs measurements. *Journal of synchrotron radiation*, 6(3):217–219, 1999.
- [59] Ch Gauthier, G Goujon, S Feite, E Moguiline, L Braicovich, NB Brookes, and J Goulon. Modulated detection of multibeam dichroism using photodiodes. *Physica B: Condensed Matter*, 208:232–234, 1995.
- [60] Shaul Barkan, Jan S Iwanczyk, Bradley E Patt, Liangyuan Feng, Carolyn R Tull, and G Vilkelis. Vortex-a new high performance silicon drift detector for xrd and xrf applications. *Adv. X-Ray Anal*, 46:332–337, 2003.
- [61] SP Cramer, O Tench, M Yocum, and GN George. A 13-element ge detector for fluorescence exafs. *Nuclear Instruments and Methods in Physics Research Section A: Accelerators, Spectrometers, Detectors and Associated Equipment*, 266(1-3):586–591, 1988.
- [62] AB Preobrajenski, May Ling Ng, AS Vinogradov, and Nils Mårtensson. Controlling graphene corrugation on lattice-mismatched substrates. *Physical Review B*, 78(7):073401, 2008.
- [63] PLJ Gunter, OLJ Gijzeman, and JW Niemantsverdriet. Surface roughness effects in quantitative xps: magic angle for determining overlayer thickness. *Applied surface science*, 115(4):342–346, 1997.

- [64] Carsten Busse, Predrag Lazić, Rabie Djemour, Johann Coraux, Timm Gerber, Nicolae Atodiressei, Vasile Caciuc, Radovan Brako, Stefan Blügel, Jörg Zegenhagen, et al. Graphene on ir (111): physisorption with chemical modulation. *Physical review letters*, 107(3):036101, 2011.
- [65] JL Stevens and RQ Hwang. Strain stabilized alloying of immiscible metals in thin films. *Physical review letters*, 74(11):2078, 1995.
- [66] O. Mironets, H. L. Meyerheim, C. Tusche, V. S. Stepanyuk, E. Soyka, H. Hong, P. Zschack, N. Jeutter, R. Felici, and J. Kirschner. Bond length contraction in cobalt nanoislands on cu(001) analyzed by surface x-ray diffraction. *Phys. Rev. B*, 79:035406, Jan 2009.
- [67] Tu Chen and P Cavallotti. Electroplated cobalt film for perpendicular magnetic recording medium. *Applied Physics Letters*, 41(2):205–207, 1982.
- [68] D.C. Jiles and D.L. Atherton. Theory of ferromagnetic hysteresis. *J. Magn. Magn. Mater.*, 61:48, 1986.
- [69] M.S. Van Dusen and A.I. Dahl. Freezing points of cobalt and nickel. *J. Res. Natl. Bur. Stand.*, 39:292, 1947.
- [70] G. Bunker. *Introduction to XAFS*. Cambridge University Press, 2010.
- [71] C. Meneghini, S. Di Matteo, C. Monesi, T. Neisius, L. Paolasini, S. Mobilio, C.R. Natoli, P.A. Metcalf, and J.M. Honig. Antiferromagnetic – paramagnetic insulating transition in cr-doped v_2o_3 investigated by exafs analysis. *J. Phys. Condens. Matter*, 21:355401, 2009.
- [72] C Meneghini, F Bardelli, and S Mobilio. Estra-fitexa: a software package for exafs data analysis. *Nucl Instrum Meth B*, 285:153, 2012.
- [73] Bruce Ravel and MATHENA Newville. Athena, artemis, hephaestus: data analysis for x-ray absorption spectroscopy using ifeffit. *J. Synchrotron Radiat.*, 12(4):537, 2005.
- [74] Alessandro Longo, Luisa Sciortino, Francesco Giannici, and Antonino Martorana. Crossing the boundary between face-centred cubic and hexagonal close packed: the structure of nanosized cobalt is unraveled by a model accounting for shape, size distribution and stacking faults, allowing simulation of XRD, XANES and EXAFS. *J. Appl. Crystallogr.*, 47(5):1562, 2014.
- [75] L. Hedin and L.I. Lundqvist. Explicit local exchange-correlation potentials. *J. Phys. C: Solid St. Phys.*, 4:2064, 1971.

- [76] A. R. Denton and N. W. Ashcroft. Vegard's law. *Phys. Rev. A*, 43:3161, 1991.
- [77] J. S. Tsay and C. S. Shern. Diffusion and alloy formation of co ultrathin films on pt(111). *J. Appl. Phys.*, 80:3777, 1996.
- [78] R. Belkhou, J. Thiele, and C. Guillot. Growth of ptcu (100): formation of a surface alloy. *Surf. Sci.*, 377:948, 1997.
- [79] D.E. Sayers and B.A. Bunker. *X-Ray Absorption*, volume 92, chapter x. Wiley, 1988.
- [80] M Newville, P Līviņš, s? Y Yacoby, JJ Rehr, and EA Stern. Near-edge x-ray-absorption fine structure of pb: A comparison of theory and experiment. *Phys. Rev. B*, 47(21):14126, 1993.
- [81] Ralph WG Wyckoff. Cubic closest packed, ccp. *Structure, Cryst. Struct*, 1:7-83, 1963.